



TECHNISCHE
UNIVERSITÄT
WIEN



institute of
telecommunications

Dissertation

RIS Analysis from Communication and Electromagnetic Perspectives

Author

MEng. Le Hao

Matriculation Number: 12037295

Advisor

Univ.Prof. Dipl.-Ing. Dr.techn. Markus Rupp

Assisting Advisor

Associate Prof. Dipl.-Ing. Dr.techn. Stefan Schwarz

Examiners

Prof. Ke Guan

Associate Prof. José Rodríguez-Piñeiro

Institute of Telecommunications
Technische Universität Wien
Vienna, Austria

July, 2024

Abstract

The next generation of wireless communication networks will facilitate the connection of a large number of devices and a broad range of services. Serving such a large amount of user equipments (UEs) can be of very high cost if using active antenna solutions such as increasing the number of base stations (BSs), using massive multiple-input multiple-output (MIMO) antennas, and deploying relays between the BSs and the UEs. In this context, a passive antenna solution, such as reconfigurable intelligent surfaces (RISs), would be more beneficial and attractive. RIS has become an emerging technology with diverse applications in future wireless networks, owing to its ability to dynamically control and optimize the propagation environment. The rapid evolution driven by escalating performance demands of coverage in blocked line-of-sight (LOS) scenarios has prompted the exploration of RIS.

Motivated by the potential benefits of RIS in enhancing signal coverage and improving energy efficiency while maintaining very low costs, this dissertation studies the RIS technology in a broad range from software development to hardware design, from simulation to measurements, and from electromagnetic theory to communication theory. The dissertation consists of three major parts corresponding to RIS modeling and applications in communication and electromagnetic aspects, as well as the verification of RIS modeling methods.

In the first part, we focus on RIS modeling in communication aspects and implement an RIS module in an open-access system-level simulator (SLS) integrated with a ray tracer. The RIS module involves most of the system-level challenges of RIS technology, especially the large-scale fading and small-scale fading modeling. The RIS-tailored SLS is able to simulate and optimize RIS-empowered single-cell or multi-cell wireless networks in realistic environments. In addition, we develop several RIS phase shift optimization algorithms, such as maximum ratio transmission (MRT), zero-forcing (ZF), and max-min signal-to-interference-plus-noise ratio (SINR)-based approaches, to maximize the minimum received power, SINR, and rate for RIS-assisted multi-user MIMO (MU-MIMO) systems. The RIS phase quantization effects are investigated within these approaches, too.

In the second part, we propose a static scatterer-based approach to improve signal propagation and coverage with passive resonate dipoles. We use theoretical models and ray tracing simulations to evaluate the contributions from such scatterers and investigate several influential factors, such as reflection material, reflection number, frequency, and the number of dipoles in indoor and outdoor scenarios. Results reveal that the contributions from such scatterers are insignificant when the direct link between the transmitting (Tx) and the receiving (Rx) antennas is not blocked.

On the contrary, these scatterers can achieve comparable gains as using an untuned RIS in scenarios where the direct link is totally blocked. Moreover, we discuss two path loss models derived from the communication and electromagnetic theory. The differences and connections between them, as well as their use cases, are evaluated in order to find an accurate and consistent model for RISs.

In the third part, we systematically study the RIS modeling methods from electromagnetic and communication aspects and build a connection between them. We start by designing an RIS based on electromagnetic theory. After verifying the scattering properties of the RIS through measurements, we extracted the parameters from the electromagnetic part and used two theoretical communication models to analyze the large-scale fading through this RIS. The RIS size and the RIS phase quantization effects are also studied in this part. Furthermore, we implement this RIS into a ray tracer and compare the simulation results with theoretical results. Since the RIS models and ray tracing simulations give consistent results, we manufacture a static anomalous reflector (AR) prototype and use the same theoretical models, as well as the ray tracing methods to evaluate the angular response, frequency response, and spatial scalability of two different-sized ARs. In the end, we perform measurements with the manufactured AR prototype and verify our RIS modeling methods.

Acknowledgments

I sincerely thank my supervisor, Prof. Markus Rupp, for his support and help throughout my Ph.D. studies and for giving me the freedom to learn, research, and pursue my goals. I am so grateful to Prof. Stefan Schwarz for his insightful and invaluable advice on my research work, he can always give me a solution when I am stuck in my work. The financial support from the European Union's Horizon 2020 research and innovation program "Meta Wireless" under the Marie Skłodowska-Curie grant agreement No. 956256 is greatly acknowledged.

Outside the institute, a special thanks to Prof. Sergei A. Tretyakov at Aalto University and Dr. Risto Valkonen at Nokia Bell Labs, Espoo, Finland. I had a wonderful cooperation experience with them. I really appreciate the support, and valuable discussions with them during and after my secondment in Nokia, Finland. I also appreciate very much that Prof. Ke Guan and Prof. José Rodríguez-Piñero agree to review my dissertation and be part of my defense examination board.

I thank my colleagues at the Institute of Telecommunications. It is a great pleasure to meet them and to know them. I am thankful for all the discussions and support from them, and the joy they bring to my life.

Finally, I want to thank my husband, Chris, who gives me endless support and encouragement.

Contents

1	Introduction	1
1.1	Motivation and scope of the dissertation	2
1.2	Structure and contribution	4
2	RIS communication model and its application	9
2.1	RIS in the Vienna system-level simulator	11
2.1.1	RIS deployment	12
2.1.2	RIS model	12
2.1.3	Macroscopic fading	13
2.1.4	Cell association	18
2.1.5	Small-scale fading	18
2.1.6	RIS phase shift optimization for SISO scenarios	20
2.1.7	Simulation results	21
2.2	Optimization of RIS-assisted MIMO systems	25
2.2.1	System model	25
2.2.2	Algorithm and problem formulation	26
2.2.3	Performance evaluation results	32
2.3	Final remarks	34
3	RIS electromagnetic model and its application	37
3.1	Improving propagation channels with static scatterers	39
3.1.1	Theoretical analysis	39
3.1.2	Ray tracing simulations	42
3.2	Communication and electromagnetic models for an optimized RIS	46
3.2.1	Comparison between the RIS CM and EM models	47
3.2.2	Simulation results	49
3.3	Final remarks	52
4	RIS model verification with a perfect anomalous reflector	53
4.1	Anomalous reflector design	55
4.2	Theoretical analysis of the large-scale fading	59
4.3	Load quantization analysis	62
4.4	Ray tracing simulations	65
4.4.1	Verification in a SISO scenario	66

4.4.2	Multi-user scenario with only LOS paths	67
4.4.3	Multi-user scenario with multi-path propagations	70
4.5	Final remarks	72
5	RIS model verification with a realistic anomalous reflector	75
5.1	Practical anomalous reflector design and fabrication	76
5.2	EM measurement of the manufactured AR	76
5.3	Communication measurement of the manufactured AR	78
5.3.1	Measurement campaign	79
5.3.2	Theoretical analysis	82
5.3.3	Ray tracing model	84
5.3.4	Results comparison	85
5.4	Final remarks	91
6	Conclusion and outlook	93
6.1	Summary of contributions	93
6.2	Possible future work directions	96
	List of Abbreviations	99
	Notation	101
	Bibliography	102

1

Introduction

Over the past few decades, the development of wireless communication networks has experienced significant evolution. This progress has taken place over multiple generations and continues today. The journey of mobile wireless communications dates back to the 1980s with the introduction of 1st generation (1G) technology, followed by 2nd generation (2G) in the early 1990s, 3rd generation (3G) in the 2000s, and 4th generation (4G) in the 2010s [1]. With strong technical specifications and standards, the 5th generation (5G) of wireless communication launched globally in 2020. The major industries and academies are currently concentrating on deploying beyond fifth-generation (B5G) and sixth-generation (6G) communication systems. The progression from 1G to the highly anticipated 6G has been characterized by exponential technological advancements, facilitating faster communication, enriched multimedia experiences, smart life expansion, and industrial ubiquitous smart mobile society [2].

The 6G technology is expected to improve and expand the capabilities of wireless networks beyond current 5G standards. These technological developments will facilitate the connection of a more significant number of devices and a wide range of new and constantly changing services [3]. According to [4], the main factors that push the development of 6G technology are the need to guarantee the reliability and security of the system, the promotion of sustainability through the use of efficient mobile technology, the acceleration of automation and digitalization, and the goal of reaching unlimited connectivity. As shown in Fig. 1.1, the objectives for technology development are to continue the classical capabilities of network enhancement, such as data rates, coverage, and latency, while exploring new dimensions of network functionality such as network sensing, security, and privacy [4].

One of the most essential concerns for technology is cost efficiency and sustainability. Especially to support a vast range of new and evolving services, exponentially growing traffic demand, and a dramatically higher number of devices, the future wireless network must ensure low costs for both users and service providers. Thus, cost-effective and sustainable solutions are of significant importance. Driven by this factor, new technologies such as reconfigurable intelligent surface (RIS), or sometimes called intelligent reflecting surface (IRS) and metasurface, have recently

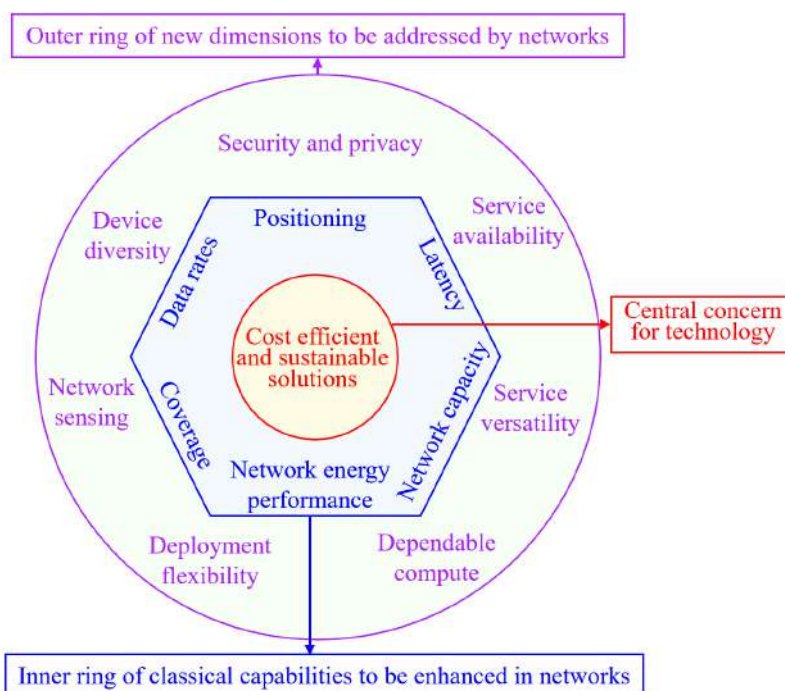


Figure 1.1: Targets for technology development in wireless communications beyond 5G.

emerged in wireless communications as a promising technique because they can improve the spectral efficiency and energy efficiency of a wireless system by artificially altering the wireless propagation environment [5, 6]. In this regard, the main objective of this dissertation is to propose reliable theoretical models, RIS-tailored simulation platforms, and measurement validation strategies for various types of RIS.

1.1 Motivation and scope of the dissertation

Reconfigurable Intelligent Surfaces

RISs have recently gained a lot of interest, as they can control the electromagnetic response of waves impinging onto them, and thereby increase the data throughput, network coverage, spectral and energy efficiency of B5G wireless communications [7–10]. An RIS is a planar structure comprising many elements with reconfigurable properties. Proper tuning of the RIS phase shifts can steer the impinging signals in desired directions and thus achieve certain communication objectives [11–13]. For example, reflected signals can contribute constructively with signals from other paths in the desired direction to enhance the power of the received signal or destructively add to undesired receivers to suppress interference or enhance security/privacy [14]. RIS is a nearly passive device that does not require active power amplifiers or radio frequency chains. Still, it needs external electric power to control the phase shifts

and the operation of the surface. It is low cost, easy to install on building facades or ceilings, and compatible with existing and future wireless systems due to its nearly passive structure [15, 16]. As a result of these compelling benefits, RIS is expected to be one of the essential technologies for 6G wireless networks.

Several fundamental design issues must be tackled to incorporate RIS into future telecommunication standards. These issues include RIS deployment, RIS modeling, large-scale and small-scale fading, system optimization, and cell association in multi-cell networks. Improving the system performance of multi-user MIMO (MU-MIMO) systems with the aid of RIS is another big challenge. RIS-related models must consider electromagnetic wave propagation principles and, meanwhile, achieve the promised benefit in a communication system in realistic environments. Due to the high cost and difficulties of performing measurements with RISs, a reliable simulation platform embedded with RIS is urgently needed to predict, analyze, and optimize the performance of RISs in diverse scenarios.

Scope of Work

Motivated by the advancements of RIS-assisted wireless systems, our aim is to address some of the main challenges in the state of the art and provide solutions to improve the performance of wireless network systems with the aid of RIS. Our goal is to connect the communication and electromagnetic communities in RIS-related studies and provide consistent modeling methods for both sides. In the communication part, we build an open-access software platform for the wireless communication society to simulate, analyze, and optimize the RIS-empowered environment. In the electromagnetic part, we design our own RIS and apply the electromagnetic RIS model to investigate its communication properties using our developed software and validate the results with measurements. More specifically, this dissertation includes three main parts to deal with various aspects of RIS system challenges:

- In the first part (chapter 2), we focus on RIS models in the communication aspect. We implement an RIS module in an open-access system-level simulator (SLS) integrated with a ray tracer, which tackles the main system-level challenges of RIS technology and provides solutions for them. The RIS-tailored SLS is then used as a practical tool to evaluate the performance of RIS-assisted communication systems in realistic and complex environments in order to foster the realization of RIS technology in real life. To boost the benefits of RISs, we develop several algorithms to optimize the RIS phase shifts for improving the performance of RIS-assisted MU-MIMO systems.
- In the second part (chapter 3), we discuss RIS models from an electromagnetic point of view. Based on ray tracing simulations, we find an alternative to improve signal propagations by randomly placing static scatterers like simple resonate dipoles. They are even cheaper and easier to deploy compared to other passive solutions, like using metallic plates, but can achieve similar results as an untuned RIS. Furthermore, we compare different RIS path loss

models and their use cases from both the communication and electromagnetic aspects and implement a more accurate model to the SLS that is derived from electromagnetic theory.

- In the third part (chapters 4 and 5), we use a designed perfect RIS and a manufactured realistic anomalous reflector (AR) to validate our proposed models and RIS implementation in the ray tracer. We analyze the electromagnetic and communication performances of both the RIS and AR through measurements, theoretical analysis, and ray tracing simulations. The comparison results achieve good agreements, which finally achieves our goal of building a complete and consistent system for RIS analysis, from electromagnetic design to communication performance in real environments and to system-level simulations for RIS-assisted wireless networks without the need to perform measurements. Our proposed methods and models can be extended to various types of RISs, and our developed SLS is able to simulate perfect and realistic RISs from both aspects.

1.2 Structure and contribution

This section provides a detailed description of the dissertation structure and the corresponding contributions. The references where the contributions were initially produced or published are also included. At the end of the dissertation, we list all the notation and acronyms used in this work.

Chapter 2 – RIS communication model and its application

This chapter describes the RIS module implemented in the Vienna 5G SLS, which includes RIS deployment, RIS model, macroscopic fading, cell association, small-scale fading, and RIS phase shift optimization. A commonly used free space path loss model for RIS, namely the RIS CM model, has been adopted to be compatible with our SLS. In addition, we modify the ray tracing (RT) model derived from the MATLAB ray tracer to obtain a more precise path loss in a realistic environment. In this way, we realize the advantages of both the RIS CM and RT models. The RIS implementation has been verified through theory, and the system performance of RIS-assisted wireless networks is evaluated through Monte Carlo simulations in the simulator.

In addition, we propose several optimization algorithms to achieve a maximized minimum signal power, signal-to-interference-plus-noise ratio (SINR), and rate in an RIS-assisted MU-MIMO system. More specifically, we propose a new maximum ratio transmission (MRT) based heuristic without/with alternating optimization, a zero-forcing (ZF) based optimization, as well as a new max-min SINR approach to minimize the total transmit power and maximize the minimum SINR, respectively. The received signal power, SINR, and rate achieved from the different proposed optimization approaches are evaluated through simulations. The RIS phase shift

quantization effects are also investigated in the proposed algorithms. The contributions of this chapter have been published in [17–19]:

- L. Hao, A. Fastenbauer, S. Schwarz and M. Rupp, “Towards System Level Simulation of Reconfigurable Intelligent Surfaces,” 2022 International Symposium ELMAR, Zadar, Croatia, 2022, pp. 81-84.
- L. Hao, S. Schwarz, and M. Rupp, “The Extended Vienna System-Level Simulator for Reconfigurable Intelligent Surfaces,” 2023 Joint European Conference on Networks and Communications & 6G Summit (EuCNC/6G Summit), Gothenburg, Sweden, 2023, pp. 1-6.
- L. Hao, S. Schwarz, and M. Rupp, “Analysis and optimization of reconfigurable intelligent surfaces assisted MIMO systems,” 2021 EuCNC/6G Summit, Porto, Portugal, 2021, pp. 13–18.

Chapter 3 – RIS electromagnetic model and its application

This chapter first explores the potential enhancement of radio signal propagation in intricate environments through the deployment of basic resonant dipole scatterers. We employ the MATLAB ray tracer algorithm to examine the impact of dipolar scatterers on the power received at the user’s location. The ray tracing model is modified for a dipolar scatterer model based on its bi-static scattering cross-section. The analytical and simulation results are compared with an untuned RIS to evaluate the benefits of the proposed approach. Next, we discuss and compare the two most commonly used path loss models for RISs derived from the electromagnetic and communication theory points of view. The differences, connections, and use cases of the two models are discussed in this chapter. The framework developed throughout this chapter has been published/accepted in [20–22]:

- L. Hao, F.S. Cuesta, S. A. Tretyakov, and M. Rupp, “Improving Propagation Channels with Static Scatterers,” IEEE Antennas and Wireless Propagation Letters, 2024, pp. 1–5.
- L. Hao, F.S. Cuesta, S. A. Tretyakov, and M. Rupp, “Optimizing propagation channels using static scatterers: Modeling and ray-tracing simulations,” 2024 IEEE International Symposium on Antennas and Propagation and ITNC-USNC-URSI Radio Science Meeting, Florence, Italy, 2024. (Registered)
- L. Hao, F. S. Cuesta and S. A. Tretyakov, “Comparison of Simplistic System-Level RIS Models and Diffraction-Theory Solutions,” 2024 18th European Conference on Antennas and Propagation (EuCAP), Glasgow, United Kingdom, 2024, pp. 1-5.

Chapter 4 – RIS model verification with a perfect anomalous reflector

In this chapter, we systematically study the electromagnetic and communication aspects of an RIS through electromagnetic (EM) simulations, system-level and ray-tracing simulations, and build a connection between the two aspects. We started by designing a periodic AR using a novel array antenna scattering synthesis technique. The designed lossless AR is capable of scattering incident waves in the normal direction to several anomalous angles through the manipulation of reactive loads. We also compare the results with continuous and quantized unit cell reflection phases with one to four-bit resolutions to evaluate the quantization effects. Next, we extract the EM properties of this designed RIS and use them in the SLS and MATLAB ray tracer to analyze the large-scale fading of simple RIS-assisted links. The analysis and results of this chapter are based on the following submitted publications [23, 24]:

- S. K. R. Vuyyuru, L. Hao, M. Rupp, S. A. Tretyakov, and R. Valkonen, “Modeling RIS from Electromagnetic Principles to Communication Systems–Part I: Synthesis and Characterization of a Scalable Anomalous Reflector,” submitted to IEEE Transactions on Antennas and Propagation. Preprint available: <https://arxiv.org/abs/2403.12790>
- L. Hao, S. K. R. Vuyyuru, S. A. Tretyakov, A. Salihu, M. Rupp, and R. Valkonen, “Modeling RIS from Electromagnetic Principles to Communication Systems–Part II: System-Level Simulation, Ray Tracing, and Measurement,” submitted to IEEE Transactions on Antennas and Propagation. Preprint available: <https://arxiv.org/abs/2403.13210>

Chapter 5 – RIS model verification with a realistic anomalous reflector

In this chapter, we elaborate on the concept of scalable AR to analyze the angular response, frequency response, and spatial scalability of a manufactured lossy AR across a broad range of angles and frequencies. We utilize theoretical models and ray tracing simulations to investigate the communication performance of two different-sized scalable finite ARs, one smaller configuration with 48×48 array of unit cells and the other constructed by combining four smaller ARs to form a larger array with 96×96 unit cells. The two AR models are implemented in the MATLAB ray tracer to simulate their communication performance in the measurement scenario. To validate our theoretical approach, we conduct over-the-air communication link measurements in a large indoor scenario to evaluate the received power through an AR link at different angles and frequencies. The analysis and results of this chapter have been included in the following submitted papers [23, 25]:

- S. K. R. Vuyyuru, L. Hao, M. Rupp, S. A. Tretyakov, and R. Valkonen, “Modeling RIS from Electromagnetic Principles to Communication Systems–Part I: Synthesis and Characterization of a Scalable Anomalous Reflector,” submitted to IEEE Transactions on Antennas and Propagation. Preprint available: <https://arxiv.org/abs/2403.12790>

1.2. Structure and contribution

- L. Hao, S. K. R. Vuyyuru, S. A. Tretyakov, M. Rupp, and R. Valkonen, “Analysis of Scalable Anomalous Reflectors through Ray Tracing and Measurements,” submitted to IEEE Transactions on Antennas and Propagation. Preprint available:

<http://arxiv.org/abs/2407.17279>

2

RIS communication model and its application

In recent years, extensive studies have been conducted for RIS-assisted communication systems. In the communication part, the RIS is usually modeled as a collection of many independent passive elements. The main contribution of RIS comes from its variable phase shifts from each element. By optimizing RIS phase shifts within the channel model of the system, different goals can be achieved, such as improving throughput, energy efficiency, SINR, signal strength, and many more. In this context, how to employ RISs in wireless network systems, how to model the large-scale and small-scale fadings for RIS-assisted links, and how to deal with interferences and cell associations are essential problems that need to be solved.

Some of these challenges have been studied in recent literature. For example, the authors in [26] compiled a list of the most frequently used RIS communication models for RIS-based wireless communication systems to evaluate and optimize the system performance. In [27], the authors investigated the impact of a large-scale RIS deployment on the cellular network performance, as well as techniques to improve the cellular network performance by overcoming blockages with a subset of nearby RISs. The RIS deployment strategy is investigated in [27] with stochastic geometry methods.

However, in the current stage of RIS-related research activities, the modeling and optimization of RIS-assisted systems are usually focused on small-scale networks, where only a couple of RISs are analyzed in a simple scenario. In addition, existing research on the effectiveness of RIS-aided communication primarily focuses on theoretical frameworks and treats the impact of different parameters separately. Very little literature is concerned with a large-scale system-level simulation of RIS-aided systems. In paper [28], the authors perform system-level simulations for a RIS-assisted urban city scenario and analyze the performance advantages. However, the influence of the RIS element number, RIS phases, RIS deployment, large-scale and small-scale fadings, cell association, and other essential and detailed information are missing: no system model for RISs is provided, and the system performance is not verified. A more efficient RIS-tailored system-level simulator that allows even larger

simulation scenarios and investigations on more performance measures is needed.

Driven by this phenomenon, the first part of this chapter introduces an extension of the well-established open-source Vienna 5G SLS [29] to support RIS-assisted transmissions in large-scale cellular networks. Most of the system-level challenges of RIS-aided wireless networks are addressed, such as RIS deployment, RIS modeling, macroscopic fading, cell association, small-scale fading, and RIS phase shift optimization for single-input single-output (SISO) scenarios. We run Monte-Carlo simulations to analyze system performance, which is verified by known theory, e.g., the power scaling law explained in [30]. With an integrated interface with the MATLAB ray tracer, the simulator can be used to comprehensively evaluate the system performance of RIS-assisted multicell or single-cell networks in a realistic environment.

The current stage of the simulator can only support RIS phase shift optimization for SISO scenarios due to the simulation time and structure restrictions. However, it would be very beneficial to also include RISs in MIMO networks to further improve the system performance, since RIS-assisted MIMO systems have been verified to be able to achieve higher spectral efficiency and signal coverage compared to traditional MIMO wireless systems [31]. So far, many different optimization algorithms have been developed to optimize RIS-assisted MIMO systems. For example, the authors in [32] studied the achievable rate optimization for an RIS-assisted multi-stream MIMO system and demonstrated that even a small number of RIS elements is sufficient to increase the achievable rate in an indoor environment. By assuming a Rayleigh fading channel in RIS-assisted single-user MIMO systems, it is proven that large RISs can make wireless channels more reliable [33]. To make full use of such RIS-assisted wireless communication systems, both the beamformer at the BS and the phase shifts at the RIS need to be optimally designed [34].

However, in the literature, the commonly used optimization methods aim to minimize the total transmit power [30] or maximize the spectral efficiency [34], while there are very limited literature studies on optimization aimed at maximizing the minimum SINR [35]. Furthermore, the assumptions of these optimization methods are very different [5,30,34–36], making it difficult to understand what kind of method can achieve the best performance for RIS-assisted MIMO systems. Therefore, the optimization method for maximizing the minimum (max-min) SINR still has a large space to investigate, and different optimization methods need to be compared systematically. In addition, most of the research work only considers the reflected link from RIS while neglecting the direct link, which does not fully acquire the network beamforming gain. Moreover, many of the optimization methods are very complicated and hard to implement in practice. A more practical optimization should also constrain the computational complexity and run time to a reasonable level.

Motivated by these aspects, in the second part of this chapter, we seek relatively better approaches that can achieve good performance and, at the same time, keep a low complexity. We propose several optimization algorithms to achieve different optimization goals, such as using the MRT, ZF, and max-min SINR approaches to

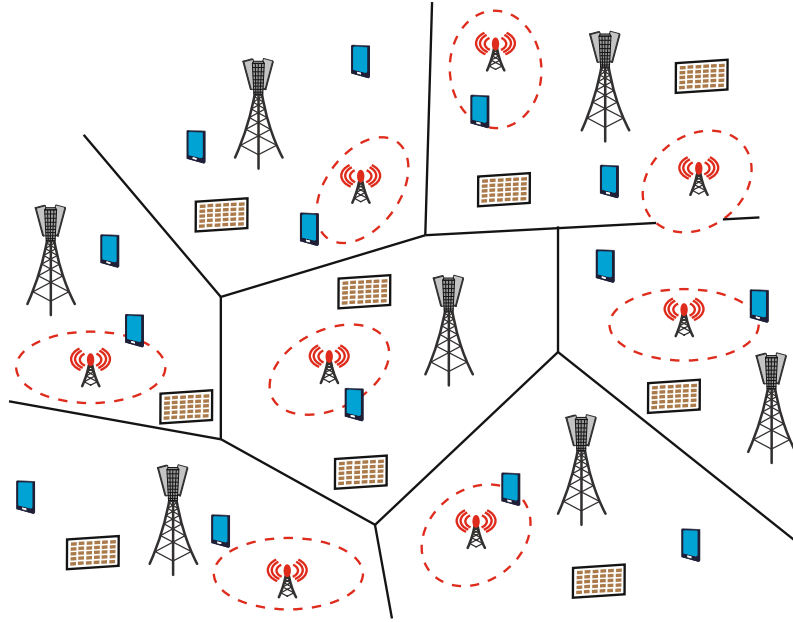


Figure 2.1: RIS-aided multi-cell wireless network.

realize a maximized minimum power, SINR, and rate. The effect of RIS phase quantization in such a network is also investigated in this chapter. The implementation of RIS in the SLS and the optimization algorithms described in this chapter are published in [17–19].

2.1 RIS in the Vienna system-level simulator

With regard to large-scale system-level analysis, the experiment is not a preferred method due to the significant expense and time commitment. As an alternative, a SLS plays a vital role in system performance analysis and optimization. Among existing simulators such as LTE-Sim [37], SimuLTE [38], and Coffee Grinder Simulator [28], the Vienna 5G SLS can simulate large-scale networks with thousands of network nodes and is very flexible to extend. In addition, it is free for academic use. Therefore, we extended the Vienna SLS to include an RIS module and include support for the MATLAB ray tracer in this simulator.

This section introduces the methodology of RIS implementation in the Vienna SLS, which includes the RIS model, path loss model, channel model, and RIS phase shift optimization in the Vienna SLS. As shown in Fig. 2.1, this implementation aims to simulate RIS-aided large-scale multi-cell wireless networks and predict system performance when there are many base stations (BSs), users, and RISs in realistic environments.

2.1.1 RIS deployment

In the SLS, RISs are created as new network nodes in addition to BSs and users in a chosen scenario. There are three types of links defined in the simulator, namely, the BS-RIS link, the RIS-user link, and the direct link (or BS-user link). Various RIS deployment options exist, e.g., Poisson distributed, on facades of buildings, or user-defined. RIS-aided links usually suffer a severe path loss since the signal has to propagate first from the BS to the RIS and then from the RIS to the user. As a result, an RIS should be placed where it has line-of-sight (LOS) connections with both BS and user, to help improve the received signal strength in the block-spot area and improve the system coverage. Therefore, we provide an option to remove/deactivate RISs that do not have LOS connections, as they have only little effect on the system performance. This allows us to reduce the simulation complexity by only considering relevant RISs.

2.1.2 RIS model

The RIS modeling method mainly depends on how it is used. The RIS modeling from an electromagnetic point of view is usually not consistent with the RIS model from a communication aspect. The electromagnetic RIS model is explained in Chapter 3. In this section, we discuss a commonly used RIS model from the communication point of view [5]: the RIS is modeled as an ideal phase shift model because the usage of the RIS is mainly to achieve an optimization goal by optimizing the RIS phase shifts. For example, the optimization goal could be to achieve maximum energy efficiency, SINR, throughput, and so on. In Sec. 2.2, we give an example of an RIS phase optimization problem with this RIS model.

In the SLS, we adopt the RIS model from [5], where the reflection coefficient of the l -th RIS element is given by $\Gamma_l = \alpha_l e^{j\phi_l}$ with $l \in 1, \dots, L$ and L is the element number of the RIS. The terms $\alpha_l \in [0, 1]$ and $\phi_l \in [-\pi, \pi)$ denote the amplitude and phase shift of the l -th RIS element, respectively. In the ideal case, we assume that the RIS reflects all the signal power it receives, i.e., $\alpha_l = 1$. Consequently, a diagonal matrix

$$\Phi = \text{diag}(e^{j\phi_1}, \dots, e^{j\phi_L})$$

represents the RIS phase shifts. Here, $\text{diag}(\mathbf{x})$ denotes a square diagonal matrix with the components of \mathbf{x} on its main diagonal. It should be noted that a far-field assumption is considered in the SLS, which refers to the distance from the transmitting (Tx)/receiving (Rx) antenna to the surface being much larger than the size of the antenna and the wavelength [39]. Hence, the wave directions and channel gain are approximately the same from all RIS elements in the array to the antennas.

2.1.3 Macroscopic fading

Both small-scale fading and macroscopic fading (MF) are included in the simulator. The MF of BS-user, BS-RIS, and RIS-user links are calculated as

$$\text{MF} = G_t - \text{PL} - \text{WL} \quad (2.1)$$

in dB. For a BS-RIS and a BS-user link, G_t is the antenna gain from the BS, whereas G_r is the RIS gain for a RIS-user link. PL is the path loss, and WL is the wall loss. The simulator supports various models to calculate the distance-dependent path loss for the direct link between the BS and the user, such as free space, urban, and suburban path loss models, etc. Wall loss is a parameter defined by blockage modeling. In the simulator, regular or arbitrary city layouts with streets and building blocks can be generated. Each blockage wall is assigned to a wall loss. The wall loss parameter is only used for the direct link because the RIS-assisted links are LOS links as mentioned in Sec. 2.1.1. That is, there are no blockages between the BS and the RIS and no blockages between the RIS and the user. Otherwise, the RIS is not helpful for signal enhancement. Therefore, WL is set to zero for RIS-assisted links. The wall loss parameter is also set to zero when the ray tracing path loss model is selected for any link since the losses due to walls and other surfaces are already included in the ray tracer.

Path loss model from the communication aspect

The original path loss models in the simulator are designed for BS-User links and are not suitable for RIS-assisted links. Therefore, we have implemented a path loss model for RIS that has been proved by measurements [40]. However, a straightforward implementation of this model within our simulator is not possible, as our simulator relies on explicitly modeling the channel between all pairs of antenna elements (including RIS elements). However, the model of [40] represents the composite scattering attenuation of the entire RIS system from multiple RIS elements. As a result, we had to adapt this path loss model for RIS to be compatible with the SLS. Since this model is widely used in the communication society, we name it the RIS CM model for convenience.

Using the RIS model in 2.1.2, we assume an RIS consisting of L elements. Based on the far-field approximation, the distance between the transmitter and each RIS element can be regarded as the same, which is denoted as d_t . The distance between each RIS element and the receiver is the same, which is indicated by d_r . Each RIS element has the same effective aperture A and gain G . The mutual coupling effect between each RIS element is not considered in this model. The reflected signal power from the l -th RIS element can be expressed by

$$P_{re,l} = P_{i,l} |\Gamma_l|^2 = P_{i,l}, \quad (2.2)$$

with $P_{i,l}$ being the incident signal power from the BS to the l -th RIS element, and

2.1. RIS in the Vienna system-level simulator

we assume $|\Gamma_l| = 1$ for perfect reflection without losses. According to Friis formula, $P_{i,l}$ can be obtained by

$$P_{i,l} = \frac{P_t G_t A}{4\pi(d_t)^2}, \quad (2.3)$$

where P_t and G_t are the transmit power and gain of the transmit antenna, respectively. The received signal power at the user side from the l -th RIS element can be written as

$$P_{r,l} = \frac{P_{re,l} G A_r}{4\pi(d_r)^2}, \quad (2.4)$$

where A_r is the effective aperture of the receiving antenna and can be calculated as follows

$$A_r = \frac{G_r \lambda^2}{4\pi}, \quad (2.5)$$

with G_r the gain of the receiving antenna.

The overall received power at the user side from all the RIS elements can be expressed as [41]

$$P_r = \frac{|E_r|^2 A_r}{2Z_0}, \quad (2.6)$$

where Z_0 is the characteristic impedance of the air. The term E_r is the total electric field of the received signal at the user from the RIS, and it can be obtained by

$$E_r = \sum_{l=1}^L E_{r,l}, \quad (2.7)$$

where $E_{r,l}$ is the electric field from l -th RIS element and is calculated by

$$E_{r,l} = \sqrt{\frac{2Z_0 P_{r,l}}{A_r}} e^{-j\psi_{r,l}}. \quad (2.8)$$

Here $\psi_{r,l}$ is the phase alteration of the received signal caused by the signal propagation and the reflection coefficient of the l -th RIS element. By combining (2.2), (2.3), (2.4), (2.7) and (2.8), we obtain

$$E_r = \sqrt{\frac{Z_0 P_t G_t G A}{8\pi^2 (d_t d_r)^2}} \sum_{l=1}^L e^{-j\psi_{r,l}}. \quad (2.9)$$

By combining (2.5) and (2.6), we get

$$P_r = \frac{|E_r|^2 G_r \lambda^2}{8\pi Z_0}. \quad (2.10)$$

The SLS uses the average received signal power obtained from (2.10) for cell association. We assign the BS that leads to the maximum received power or maximum

2.1. RIS in the Vienna system-level simulator

SINR as the desired BS for the user, and other BSs are regarded as interfering BSs. During this phase, the RIS phases cannot be optimized for a user as the user is not yet attached to the BS. Therefore, this received power should be based on random RIS phases. We replace $|E_r|^2$ by its expected value, with expectation taken over the phases $\psi_{r,l}$. To calculate this expected value, we assume that $\psi_{r,l}$ are uniform random in $[0, 2\pi]$ and statistically independent. As a result, we can rewrite (2.10) by inserting (2.9) as

$$P_r = \frac{P_t G_t G G_r \lambda^2 A}{64\pi^3 (d_t d_r)^2} \sum_{l=1}^L |e^{-j\psi_{r,l}}|^2 = \frac{P_t G_t G G_r \lambda^2 L A}{64\pi^3 (d_t d_r)^2}. \quad (2.11)$$

Yet, as soon as a user is connected to a BS, we can optimize the RIS phases for this user. The main difference between our path loss model and the path loss model from [40] is that they assume the RIS phases are already optimized for the user when calculating the path loss, and hence, the phasor in (2.10) is summed coherently in [40]. In their approach, the RIS phase shift optimization happens purely in macroscopic fading, no small-scale fading is involved. The direct link is not considered in that paper, either. However, in the SLS, we need to include all the direct and RIS-assisted links, as well as the macroscopic fading and small-scale fading. We optimize the RIS phase shifts according to the channel information of each link, and hence, the RIS phase shift optimization is done in small-scale fading.

The user receives signals from both the direct link and the RIS-assisted link. Let $\text{MF}_{\text{d,CM}}$ and $\text{MF}_{\text{ris,CM}}$ denote the macroscopic fading of the direct link and RIS-assisted link, respectively. In the SLS, we assume the gain of the user antenna and each RIS element equal to one as default, i.e., $G_r = G = 1$. Of course, these parameters can always be changed by users of the simulator for their own simulations. According to (2.11), the macroscopic fading (MF) for RIS-assisted link can be written as

$$\text{MF}_{\text{ris,CM}} = \frac{P_t}{P_r} = \frac{64\pi^3 (d_t d_r)^2}{G_t \lambda^2 L A}. \quad (2.12)$$

The macroscopic fading for the direct link $\text{MF}_{\text{d,CM}}$ can be obtained from existing path loss models, such as the free space path loss model and path loss models from the 3GPP standards. The overall MF at the user side obtained from the RIS CM model can be written as

$$\text{MF}_{\text{CM}} = \text{MF}_{\text{ris,CM}} + \text{MF}_{\text{d,CM}}. \quad (2.13)$$

Path loss model from ray tracing

The RIS CM model is a free space path loss model that considers only a LOS path between the BS and the RIS and between the RIS and the user. It cannot model the path loss in a realistic environment that includes 3D buildings, blockages, streets, etc. However, this issue can be solved by a ray tracer since it includes the effects of the environment. Since the MATLAB ray tracer is a mature platform and uses

2.1. RIS in the Vienna system-level simulator

the same programming language as the SLS, we create an interface to support the MATLAB ray tracer in the SLS. With this ray tracer, we can obtain more precise MF in a realistic environment and take the influence of the propagation environment into account.

The ray tracer in versions up to MATLAB R2024a cannot model RIS as a multi-element surface and perform ray tracing for each RIS element. In fact, all the network nodes, that is, the BS, the user, and the RIS, are modeled as antennas. When there is no specific radiation pattern or antenna type assigned for the network nodes, the ray tracer will use the isotropic antenna as the default setting for each network node. Therefore, when the RIS acts as an isotropic antenna and radiates uniformly in all directions, it is not correct and does not realize its function. To properly model the RIS and calculate the correct MF, we have to modify the ray tracing model. Since the MATLAB ray tracer generates LOS and reflection rays between each network node, we model RIS first as a receiving antenna that receives power from the BS, then we use the RIS as a transmitting antenna to transmit all the power it receives. That is, we analyze the MF via two separate links: BS-RIS link and RIS-user link. Since the RIS is an isotropic antenna in this model, we can manually modify the RIS using the RIS CM model as a reference.

First, we use the same scenario as in the RIS CM model: one BS and a user, and one RIS with L elements. In the SLS, the MF for the RIS-assisted link from the ray tracer is calculated as

$$\tilde{\text{MF}}_{\text{ris,RT}} = \frac{1}{G_t} \tilde{\text{P}}L_{ur} \tilde{\text{P}}L_{rb}, \quad (2.14)$$

where $\tilde{\text{P}}L_{ur}$ and $\tilde{\text{P}}L_{rb}$ are path losses of the RIS-user and BS-RIS links, respectively. Assuming there is only one LOS path between the RIS and the user, and one LOS path between the BS and the RIS, the path loss of the two links is obtained by

$$\tilde{\text{P}}L_{ur} = (4\pi d_{ur}/\lambda)^2, \quad (2.15)$$

and

$$\tilde{\text{P}}L_{rb} = (4\pi d_{rb}/\lambda)^2, \quad (2.16)$$

with d_{ur} and d_{rb} the propagation distances of these links. Hence, (2.14) becomes

$$\tilde{\text{MF}}_{\text{ris,RT}} = \frac{(4\pi)^4 (d_{ur} d_{rb})^2}{G_t \lambda^4}. \quad (2.17)$$

However, this MF does not include the RIS effect. When the RIS size or element number changes, the MF is the same, which is incorrect. Through comparison between the (2.17) and (2.12), we introduce an RIS size factor $\eta = \lambda^2/4\pi LA$ and multiply it with (2.17), we will get the same results as in (2.12). The modified MF for RIS-link from the RT is obtained by

$$\text{MF}_{\text{ris,RT}} = \eta \tilde{\text{MF}}_{\text{ris,RT}} = \frac{\eta}{G_t} \tilde{\text{P}}L_{ur} \tilde{\text{P}}L_{rb}, \quad (2.18)$$

2.1. RIS in the Vienna system-level simulator

Now we consider a more general scenario in the ray tracer where there are K , N , and M paths (including both LOS and non-line-of-sight (NLOS) paths) for the BS-user, RIS-user, and BS-RIS links, respectively. The indices $(\cdot)_{ub}^{(k)}$, $(\cdot)_{ur}^{(n)}$, and $(\cdot)_{rb}^{(m)}$ denote the variables over the k -th path between the BS and the user, variables over the n -th path between the RIS and the user, and variables over the m -th path between the BS and the RIS, respectively. Since the path loss is obtained by each ray from the ray tracer, we cannot directly obtain the overall path loss for each link. However, we can calculate the overall received power for each link.

First, the received powers from the BS-user, RIS-user, and BS-RIS links are calculated as

$$P_{ub} = \left| \sum_{k=1}^K (\sqrt{P_t/PL_{ub}^{(k)}} \exp(-j\vartheta_{ub}^{(k)})) \right|^2, \quad (2.19)$$

$$P_{ur} = \left| \sum_{n=1}^N (\sqrt{P_{ris}/PL_{ur}^{(n)}} \exp(-j\vartheta_{ur}^{(n)})) \right|^2, \quad (2.20)$$

and

$$P_{rb} = \left| \sum_{m=1}^M (\sqrt{P_t/PL_{rb}^{(m)}} \exp(-j\vartheta_{rb}^{(m)})) \right|^2, \quad (2.21)$$

respectively. In these equations, $PL_{ub}^{(k)}$, $PL_{ur}^{(n)}$, and $PL_{rb}^{(m)}$ are the path loss of the specific propagation path for the three links. The path loss of a LOS path is obtained in the same way as (2.15) and (2.16). However, when the path is an NLOS path, the path loss includes the attenuation due to the reflections through blockages, i.e.,

$$PL_{ub}^{(k)} = \left(4\pi d_{ub}^{(k)} / \lambda \right)^2 \beta^{(k)}, \quad (2.22)$$

where $d_{ub}^{(k)}$ is the propagation distance for the k -th path between the BS and the user, and $\beta^{(k)}$ is the reflection loss for the k -th path. The $PL_{ur}^{(n)}$ and $PL_{rb}^{(m)}$ are calculated in the same way. The reflection loss is dependent on the type of the surface. For example, the reflection surfaces “concrete” and “glass” will lead to different losses. More details on the influence of material type are explained in Chapter 3. The terms $\vartheta_{ub}^{(k)}$, $\vartheta_{ur}^{(n)}$, and $\vartheta_{rb}^{(m)}$ denote the propagation phases of these links. P_{ris} is the transmit power from the RIS, which is assumed the same as the received signal power at that RIS.

Next, we calculate the overall path loss for these links as

$$PL_{ub} = P_t/P_{ub}, \quad (2.23)$$

$$PL_{ur} = P_{ris}/P_{ur}, \quad (2.24)$$

and

$$PL_{rb} = P_t/P_{rb}. \quad (2.25)$$

2.1. RIS in the Vienna system-level simulator

Finally, in a general scenario where each link consists of multiple reflection paths, we replace the $\tilde{\text{P}}L_{ur}$ and $\tilde{\text{P}}L_{rb}$ in (2.18) with $\text{P}L_{ur}$ and $\text{P}L_{rb}$ in (2.24) and (2.25), then we get the final macroscopic fading for the RIS-link as

$$\text{MF}_{\text{ris,RT}} = \frac{\eta}{G_t} \text{P}L_{ur} \text{P}L_{rb}, \quad (2.26)$$

The MF of the direct link from the ray tracing model is obtained as

$$\text{MF}_{\text{d,RT}} = \frac{1}{G_t} \text{P}L_{ub}. \quad (2.27)$$

The overall MF at the user side obtained from the modified ray tracing model can be written as

$$\text{MF}_{\text{RT}} = \text{MF}_{\text{ris,RT}} + \text{MF}_{\text{d,RT}}. \quad (2.28)$$

2.1.4 Cell association

For large-scale multi-cell wireless networks, each user should be assigned to a cell, which leads to the cell association problem. Two cell association strategies are implemented in the simulator: maximum received power and maximum SINR. The received power and the SINR at each user from each BS are calculated as follows:

$$P_r = P_t / \text{MF}, \quad (2.29)$$

and

$$\text{SINR} = P_r / (P_i + \sigma^2). \quad (2.30)$$

In (2.29), P_t is the transmit power at the Tx antenna in Watt, and MF is the total macroscopic fading obtained from different path loss models in Sec. 2.1.3, i.e., from (2.13) or (2.28). The P_i in (2.30) is the received power from all interfering BSs, and σ^2 is the noise power. Since the received power and SINR are calculated by each BS, we assume all BSs other than the calculated BS are interfering BSs. After that, we compare all the received power and SINR values from all the BSs, the user is then assigned to the BS that leads to the highest received power or SINR. Other BSs are regarded as interference. When users are moving, the cell association will be updated accordingly. In this process, small-scale fading and RIS phase shifts are not involved, only macroscopic fading is considered.

2.1.5 Small-scale fading

Small-scale channel fading is generated according to the parameter setups of BS, user, and RIS. The frequency-selective channels should be taken into account in wideband communications. When the user side receives signals from both direct links and RIS-assisted links, the extra delays from BS-RIS and RIS-user links should be considered. As shown in Fig. 2.2, $\mathbf{H}_d \in \mathbb{C}^{N_r \times N_t}$, $\mathbf{H}_t \in \mathbb{C}^{L \times N_t}$ and $\mathbf{H}_r \in \mathbb{C}^{N_r \times L}$

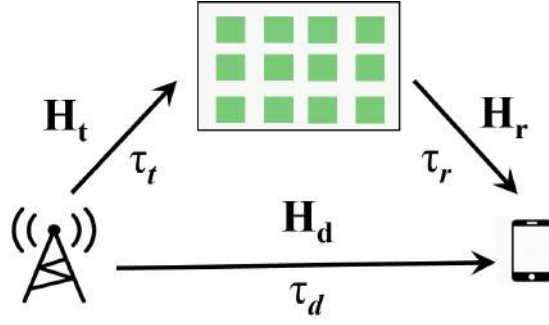


Figure 2.2: Channels and delays

represent the channels of BS-user, BS-RIS and RIS-user links, respectively. Here N_t and N_r are the number of antennas at the BS and user, respectively. The corresponding delays of these channels are τ_d , τ_t , and τ_r , respectively, which are calculated according to the geometrical distances of the network nodes. The delay difference between the RIS-assisted link and the direct link is

$$\Delta\tau = \tau_t + \tau_r - \tau_d. \quad (2.31)$$

The extra delays for BS-RIS and RIS-user links can be calculated as

$$\Delta\tau_t = \Delta\tau \cdot \frac{\tau_t}{\tau_t + \tau_r} \quad (2.32)$$

and

$$\Delta\tau_r = \Delta\tau \cdot \frac{\tau_r}{\tau_t + \tau_r}, \quad (2.33)$$

respectively. The extra delays are then included in the corresponding channels:

$$\mathbf{H}_{t'} = \mathbf{H}_t \cdot \exp(j2\pi f \Delta\tau_t) \quad (2.34)$$

and

$$\mathbf{H}_{r'} = \mathbf{H}_r \cdot \exp(j2\pi f \Delta\tau_r), \quad (2.35)$$

where f is subcarrier frequency. The channel of an RIS-assisted link can be written as

$$\mathbf{H}_{\text{RIS}} = \mathbf{H}_{r'} \cdot \Phi \cdot \mathbf{H}_{t'} \quad (2.36)$$

with $\Phi = \text{diag}(e^{j\phi_1}, \dots, e^{j\phi_L})$ being the diagonal matrix of RIS phase shifts.

Now when we consider a scenario where there are R RISs between one BS and one user, the total channel of the direct and RIS-assisted links including the effect of macroscopic fadings is calculated by

$$\mathbf{H}_{\text{tot}} = \sqrt{\gamma_e} \mathbf{H}_e \quad (2.37)$$

2.1. RIS in the Vienna system-level simulator

in the simulator. Here γ_e is the effective path gain in linear scale and is obtained by

$$\gamma_e = \gamma_d + \sum_{r=1}^R \gamma_{\text{ris}} \quad (2.38)$$

with

$$\gamma_d = 1/\text{MF}_d \quad (2.39)$$

and

$$\gamma_{\text{ris}} = 1/\text{MF}_{\text{ris}}, \quad (2.40)$$

being the path gain of the direct and RIS-assisted links, respectively. The MF_d and MF_{ris} are the same as in (2.13) or (2.28) based on the choice of path loss model. The effective channel \mathbf{H}_e is calculated by

$$\mathbf{H}_e = \sqrt{\frac{\gamma_d}{\gamma_e}} \mathbf{H}_d + \sum_{r=1}^R \sqrt{\frac{\gamma_{\text{ris}}}{\gamma_e L_r}} \mathbf{H}_{\text{RIS},r} \quad (2.41)$$

with $\mathbf{H}_{\text{RIS},r}$ being the r -th RIS-assisted channel obtained from (2.36). The parameter L_r is the element number of the r -th RIS. We normalize $\mathbf{H}_{\text{RIS},r}$ by $1/\sqrt{L_r}$ to compensate for the factor L in (2.11), because the effect of L is already included in the multiplication of $\mathbf{H}_{r'} \cdot \Phi \cdot \mathbf{H}_{t'}$.

2.1.6 RIS phase shift optimization for SISO scenarios

The RIS phase shifts can be chosen as random or optimized for the SISO scenario in the simulator. In order to receive maximum power on the user side, the RIS phase shifts are usually designed to achieve a constructive, coherent combination of the direct link and RIS-assisted link. We assume a single-antenna BS and a single-antenna user with an RIS consisting of L elements. Then the channels of the BS-user, BS-RIS, and RIS-user links become h_d , $\mathbf{h}_{t'}$, and $\mathbf{h}_{r'}$. Since $N_t = N_r = 1$, h_d is a scalar. We assume the BS-RIS and RIS-user links have strong LOS paths, while the BS-user link has NLOS paths. Therefore, $\mathbf{h}_{t'}$ and $\mathbf{h}_{r'}$ are generated based on the Rician model, and h_d is generated according to the Rayleigh channel model. The average power of h_d , $\mathbf{h}_{t'}$ and $\mathbf{h}_{r'}$ are all normalized to one, i.e., $\mathbb{E}(|h_d|^2) = 1$, etc.

In reality, the RIS phase cannot be subcarrier-dependent, as the same phase shifts have to be applied for all subcarriers. Thus, the frequency-selective channels are averaged over the subcarrier domain first, then the optimized phase shift of the l -th RIS element is calculated as

$$\phi_l = \arg(h_d) - \arg(h_{t',l} \cdot h_{r',l}). \quad (2.42)$$

The optimized RIS phase shifts are also calculated according to the associated BS, i.e., using the h_d and $h_{t',l}$ from the desired BS. When the cell association is updated,

the phase shifts will be changed according to the assigned BS. Because in the real world, RISs cannot have different phase shifts for different BSs. The phase shifts should be the same for all available BSs. Currently, the optimization process is done for each user one by one, and the interference between different users is not involved. An example of RIS phase shift optimization in MU-MIMO scenarios is discussed in Sec. 2.2. However, the implementation of such optimization algorithms in the SLS is postponed to further work due to the simulator structure, simulation time cost, the user's needs, etc. Therefore, in the current version of the Vienna SLS, random RIS phase shifts are applied in MU-MIMO scenarios.

2.1.7 Simulation results

A system-level simulation in a simple scenario is always the first step to assess the developing technologies and acts as a stepping-stone for large-scale system-level simulations. Hence, performing system-level simulations in a SISO scenario first and comparing the results with known theory is essential for developing a reliable system-level simulator. In this section, we first verify our models through theory in a SISO scenario, and then we extend the simulations to a complex scenario to evaluate the influence of an RIS.

Verification in a SISO scenario

To verify the implemented RIS CM and RT model, we conduct Monte Carlo simulations in a simple SISO scenario with a strong LOS component, for which we expect both models to show very similar results. We download a region in Vienna from the OpenStreetMap and place one single-antenna BS, one single-antenna user, and an RIS with L elements in the scenario as shown in Fig. 2.3. The BS, RIS, and user heights are 30 m, 20 m, and 1.5 m, respectively. The distance between the BS and the RIS is 62 m, and the distance between the RIS and the user is 49 m. Since RIS mainly contributes to blocked users, we set the path loss for the direct link as 200 dB to assume the direct link is blocked so that we only observe the contribution caused by RIS. The center frequency is 6 GHz, and the bandwidth is 20 MHz for the simulation.

Since the locations of the BS, user, and RIS are fixed, the MF of the BS-RIS and RIS-user links are also fixed in each simulation. However, the channel matrix is generated randomly within each simulation based on the selected channel model in the simulator. We set the Rician model for the BS-RIS and RIS-user links since there is a strong LOS path, and the Rayleigh channel model is chosen for the BS-user link since there is no LOS path between the BS and the user. The final output results are average results over a large number of simulations. Therefore, we plot the resulting curves with a 95% confidence interval, revealing that after running a large number of independent simulations, 95% of values will fall into this range.

According to the power scaling law addressed in [30], the signal-to-noise ratio (SNR) grows as L^2 in the far field with optimized RIS phase shifts. So the SNR will

2.1. RIS in the Vienna system-level simulator

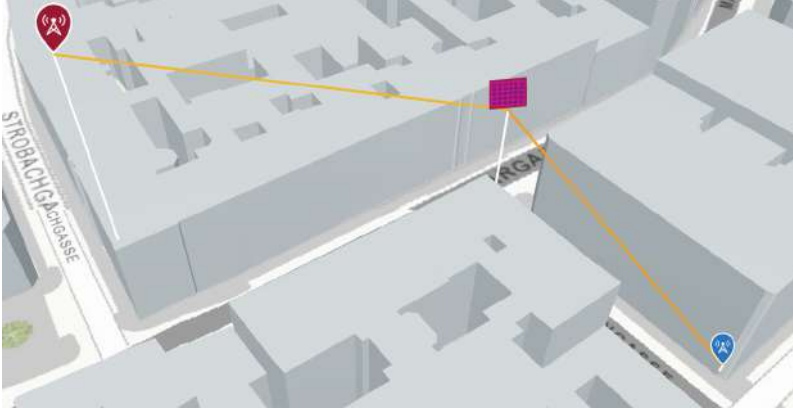
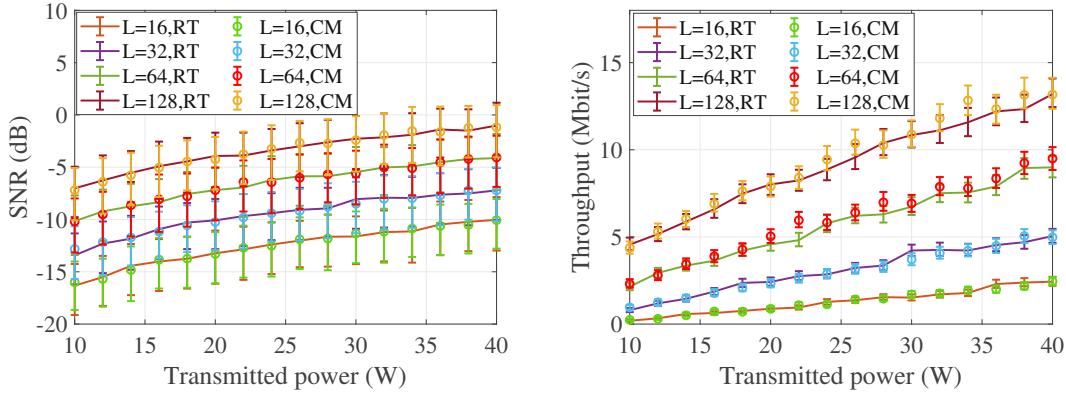


Figure 2.3: A SISO simulation scenario (the red, pink, and blue icons represent BS, RIS, and user, respectively).



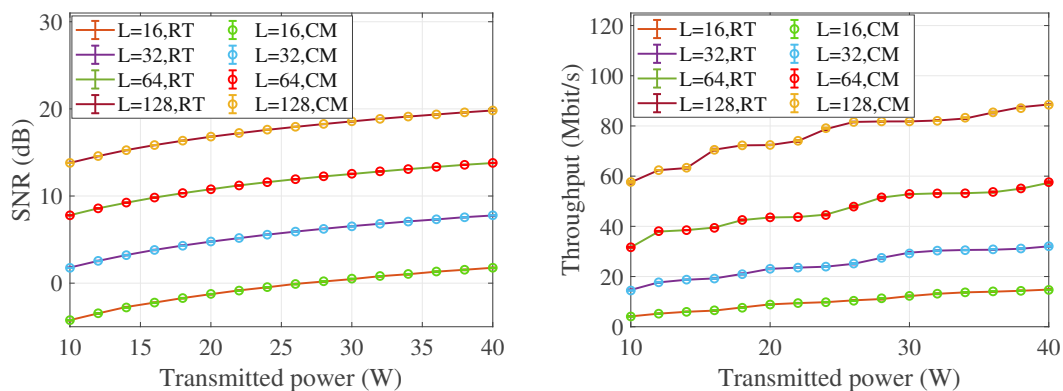
(a) SNR results with random RIS phase shifts in a SISO scenario. (b) Throughput results with random RIS phase shifts in a SISO scenario.

Figure 2.4: Simulation results with random RIS phase shifts in a SISO scenario.

increase 6 dB when doubling L . However, with random RIS phase shifts, the SNR can only improve 3 dB when doubling L . Fig. 2.4(a) shows the simulation results of SNR with random RIS phase shifts, the SNR from the SLS shows consistent results with the power scaling law, where a 3 dB gain can be observed when we double the RIS element L from 16 to 32 to 64 and to 128. In addition, the results from the RIS CM and RT models are almost identical, which verifies that the RIS size factor η leads to the equivalent results from the RIS CM and RT models.

The throughput results with random RIS phase shifts are shown in Fig. 2.4(b). The results from the RIS CM and RT models achieve good consistency. The throughput is improved when increasing L . Fig. 2.5(a) and Fig. 2.5(b) show the results of SNR and throughput with optimized RIS phase shifts, respectively. From Fig. 2.5(a), we can observe that the SNR grows 6 dB when doubling L for both the RIS CM and RT models, which is also consistent with the theory. The throughput improves with the increasing L . Both the SNR and throughput results are much better than

2.1. RIS in the Vienna system-level simulator



(a) SNR results with optimized RIS phase shifts in a SISO scenario. (b) Throughput results with optimized RIS phase shifts in a SISO scenario.

Figure 2.5: Simulation results with optimized RIS phase shifts in a SISO scenario.



Figure 2.6: A complex simulation scenario.

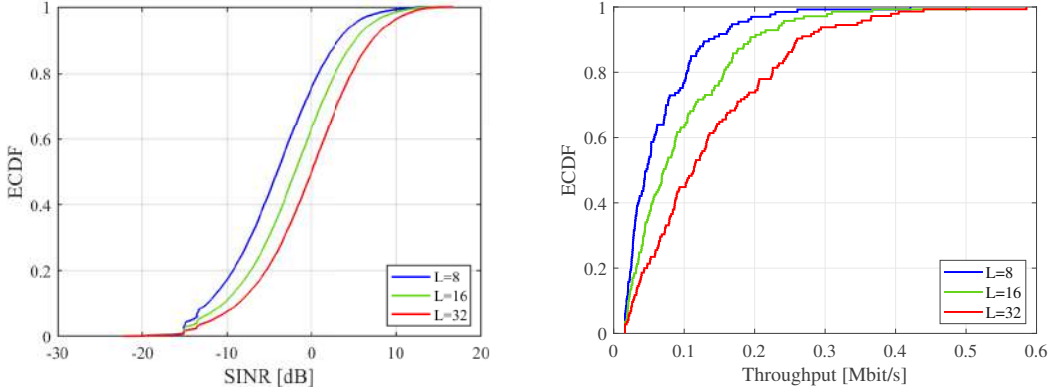
the results with random RIS phase shifts. The results from the RIS CM and RT models are consistent in these figures, too.

In conclusion, the simulation in such a SISO scenario verifies our implementation of RIS in the Vienna SLS and proves that the modified RT model is consistent with the RIS CM model. For more complex scenarios, we can use the modified RT model to replace the RIS CM model for more precise results. For example, the RT model can also include other effects such as penetration loss through different buildings, effects of different materials and reflecting surfaces, etc.

Simulation in a complex scenario

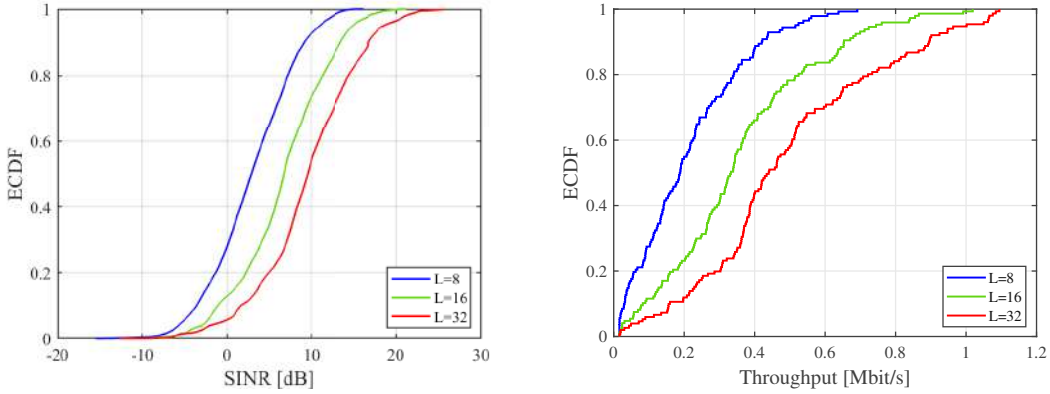
After verification of the RIS module in the SLS, we can conduct simulations in more complex scenarios. Fig. 2.6 shows an example of a complex scenario with RIS. In

2.1. RIS in the Vienna system-level simulator



(a) SINR results with random RIS phase shifts in a complex scenario. (b) Throughput results with random RIS phase shifts in a complex scenario.

Figure 2.7: Simulation results with random RIS phase shifts in a complex scenario.



(a) SINR results with optimized RIS phase shifts in a complex scenario. (b) Throughput results with optimized RIS phase shifts in a complex scenario.

Figure 2.8: Simulation results with optimized RIS phase shifts in a complex scenario.

this scenario, the environment and heights of BSs, users, and RISs are the same as in Fig. 2.3, except that in this scenario, there are two BSs, 15 RISs, and many users randomly located on the street. The center frequency is 3.5 GHz. Similarly, to only observe the influence of RIS-assisted links, we set the path loss for all direct links as 200 dB, assuming that the direct links are all blocked. The RIS-assisted links obtain the path loss from the modified RT model with a maximum of three reflections.

Next, we compare the simulation results in the scenarios with random and optimized RIS phase shifts. In the former case, all RIS phase shifts are random variables. In the latter case, for each associated user-BS pair, we find the RIS that leads to the highest received power at the user, and then that RIS is the desired RIS for that user-BS pair. The received power is only based on the macroscopic fading, and the small-scale fading is not involved. Hence, the RIS with the shortest propagation

path is usually the desired RIS for the user. Next, we optimize the phase shifts of this desired RIS and other RISs remaining random phase shifts for this user.

The results of SINR with random RIS phase shifts are shown in Fig. 2.7(a). From this figure, we can find that with increased L , the empirical cumulative distribution function (ECDF) of the SINR gets improved. A similar trend can be discovered in Fig. 2.7(b) for the throughput. The throughput results get better when L is increased. The maximum throughput value is higher when L is larger.

The SINR and throughput with optimized phase shifts are shown in Fig. 2.8(a) and Fig. 2.8(b), respectively. Compared with the results from random phase shifts, the optimized phase shifts lead to much higher SINR and throughput. When increasing L , the SINR and throughput are both improved. The range of SINR and throughput values in the case of optimized RIS phase shifts are higher than the results with random phase shifts. For example, when we observe the results with $L = 32$, the maximum SINR reaches 26 dB with optimized RIS phase shifts, whereas the maximum SINR is 17 dB with random phase shifts. The maximum throughput with optimized RIS phase is 1.1 Mbit/s, while the random phase shifts lead to around 0.6 Mbit/s.

2.2 Optimization of RIS-assisted MIMO systems

To make full use of RIS-assisted MIMO communication systems, different optimization methods need to be compared systematically. In this section, we propose a new MRT based heuristic without/with alternating optimization, as well as ZF based optimization to minimize the total transmit power, taking the direct path and the reflected paths through the RIS into account. We also propose a new max-min SINR approach combined with a bisection search method to maximize the minimum SINR, which can lead to a good performance while maintaining a low computational complexity. We evaluate and compare the system performance, such as the received signal power, SINR and rate achieved from the proposed different optimization approaches by means of simulations. To make the optimization more practical, we also use quantized RIS-phase shifts in the proposed algorithms and compare the performance achieved by unquantized and quantized phase shifts.

2.2.1 System model

We consider an RIS-assisted multi-user MIMO communication system as shown in Fig. 2.9. It consists of one BS with N_t antennas and N_u single-antenna users. The RIS consists of L elements, and we assume each element of the RIS can only passively reflect the signals from BS to all the users independently. Define ϕ_l as the phase shift of the l -th RIS element, which satisfies $\phi_l \in [0, 2\pi)$, $|\phi_l| = 1, l = 1, \dots, L$. Let $\Phi = \text{diag}(e^{j\phi_1}, \dots, e^{j\phi_L})$ be the diagonal matrix of RIS phase shifts.

Matrix $\mathbf{H} \in \mathbb{C}^{L \times N_t}$ denotes the channel from BS to RIS, $\mathbf{h}_{ui} \in \mathbb{C}^{L \times 1}$ represents the channel from RIS to the i -th user, and $\mathbf{h}_i \in \mathbb{C}^{N_t \times 1}$ is the direct channel from

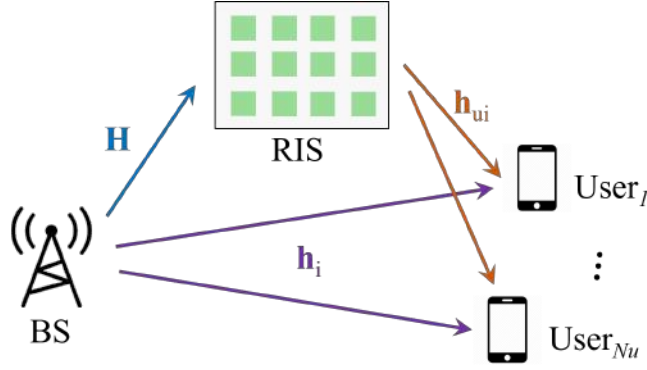


Figure 2.9: An RIS-assisted multi-user MIMO system.

BS to the i -th user. At BS, we assign a beamforming vector to each user. Hence, the transmitted signal from BS can be written as $\mathbf{x} = \sum_{i=1}^{N_u} \mathbf{f}_i s_i$, where $\mathbf{f}_i \in \mathbb{C}^{N_t \times 1}$ is the beamformer applied at BS for transmission to user i , s_i denotes the transmitted symbol intended for user i and satisfies $\mathbb{E}(|s_i|^2) = 1$.

The received signal at the i th user including both the BS-User and BS-RIS-User channels can be expressed as

$$y_i = (\mathbf{h}_i^H + \mathbf{h}_{ui}^H \Phi \mathbf{H}) \mathbf{f}_i s_i + \sum_{j \neq i}^{N_u} (\mathbf{h}_i^H + \mathbf{h}_{ui}^H \Phi \mathbf{H}) \mathbf{f}_j s_j + n_i. \quad (2.43)$$

Here, $n_i \sim \mathcal{CN}(0, \sigma^2)$ denotes additive white Gaussian noise (AWGN) at the i th user.

The signal power received at the i th user can be written as

$$P_i = |(\mathbf{h}_i^H + \mathbf{h}_{ui}^H \Phi \mathbf{H}) \mathbf{f}_i|^2. \quad (2.44)$$

The SINR achieved at the i th user can be calculated as

$$\text{SINR}_i = \frac{|(\mathbf{h}_i^H + \mathbf{h}_{ui}^H \Phi \mathbf{H}) \mathbf{f}_i|^2}{\sum_{j \neq i}^{N_u} |(\mathbf{h}_i^H + \mathbf{h}_{ui}^H \Phi \mathbf{H}) \mathbf{f}_j|^2 + \sigma_i^2}. \quad (2.45)$$

Moreover, the achievable rate of user i is

$$R_i = \log_2(1 + \text{SINR}_i). \quad (2.46)$$

2.2.2 Algorithm and problem formulation

In practice, this system can be applied to increase the received signal power or the achievable rate, which is a function of SINR. Hence, we aim at maximizing the minimum signal power of users or at maximizing the minimum SINR at users

by decoupled optimization of the beamformers at the BS and the phase shifts at the RIS, subject to the maximum transmitted power constraint at the BS. We apply three approaches: MRT, ZF, and max-min SINR, to analyze the signal power, SINR, and rate, respectively, in order to investigate which approach can achieve a better performance.

More specifically, we use a Rayleigh fading channel model in this system. We assume that the BS and users can transmit pilot signals. The BS can estimate the individual channels \mathbf{h}_i to the users, as well as, the effective channel over the RIS, i.e., the product $\mathbf{h}_{ui}^H \Phi \mathbf{H}$. Based on this information, the BS selects beamformers for the total channel (direct and RIS-assisted channel) of the users. This information can be obtained by uplink channel estimation using pilots transmitted by the users. At the RIS, we assume that the RIS can estimate the beamformed channel from the BS to the RIS, i.e., the product $\mathbf{H} \mathbf{f}_i$, as well as, the channel \mathbf{h}_{ui} to the users. The channel $\mathbf{H} \mathbf{f}_i$ can be estimated from beamformed pilot signals transmitted by the BS, whereas the channel \mathbf{h}_{ui} can be estimated from pilot signals from the users. Based on this information, we consider a decoupled optimization at BS and RIS.

MRT-based heuristic without alternating optimization

In this approach, we aim to maximize the minimum signal power received by the users. The purpose is to achieve good signal quality for all users, i.e., a fair resource allocation, rather than having some users with very large power, whereas others only receive very little power. The optimal phase-shift matrix depends on the selected beamformers, and conversely, the optimal beamformers depend on the phase-shift matrix. Hence, this interdependency would actually require a joint optimization of both. However, we assume that this optimization is done independently by BS and RIS, by decoupling the two optimizations. This is achieved by performing the optimization of Φ for unknown \mathbf{f}_i and then selecting \mathbf{f}_i for known Φ . Therefore, this algorithm can be processed in two steps: 1st, select Φ without knowing \mathbf{f}_i . 2nd, select \mathbf{f}_i after knowing Φ .

For the first step, we consider the expected value of power received over the RIS

$$\begin{aligned}
 \mathbb{E}\{|\mathbf{h}_{ui}^H \Phi \mathbf{H} \mathbf{f}_i|^2\} &= \mathbb{E}\{|\mathbf{h}_{ui}^H \Phi \mathbf{h}_{ieff}|^2\} \\
 &= \mathbb{E}\{|\boldsymbol{\theta}^T (\mathbf{h}_{ui}^* \odot \mathbf{h}_{ieff})|^2\} \\
 &= \mathbb{E}\{\boldsymbol{\theta}^T (\mathbf{h}_{ui}^* \odot \mathbf{h}_{ieff}) (\mathbf{h}_{ui}^* \odot \mathbf{h}_{ieff})^H \boldsymbol{\theta}^*\} \\
 &= \mathbb{E}\{\boldsymbol{\theta}^T (\mathbf{h}_{ui}^* \mathbf{h}_{ui}^T) \odot (\mathbf{h}_{ieff} \mathbf{h}_{ieff}^H) \boldsymbol{\theta}^*\},
 \end{aligned} \tag{2.47}$$

where $\mathbf{h}_{ieff} = \mathbf{H} \mathbf{f}_i$, $\boldsymbol{\theta}$ is an $M \times 1$ column vector containing all the diagonal elements of Φ . Since \mathbf{f}_i is unknown yet, we suppose that $\mathbf{H} \mathbf{f}_i$ is random and isotropically distributed. Then the expected value of $\mathbf{h}_{ieff} \mathbf{h}_{ieff}^H = \mathbf{H} \mathbf{f}_i \mathbf{f}_i^H \mathbf{H}^H$ is proportional to a

scaled identity matrix. Hence, Equation (2.47) can be reduced as

$$\begin{aligned}\boldsymbol{\theta}^T \mathbf{h}_{ui}^* \mathbf{h}_{ui}^T \boldsymbol{\theta}^* &= \boldsymbol{\theta}^H \mathbf{h}_{ui} \mathbf{h}_{ui}^H \boldsymbol{\theta} \\ &= \text{tr}(\boldsymbol{\theta}^H \mathbf{h}_{ui} \mathbf{h}_{ui}^H \boldsymbol{\theta}) \\ &= \text{tr}(\boldsymbol{\Theta} \mathbf{h}_{ui} \mathbf{h}_{ui}^H),\end{aligned}\tag{2.48}$$

where $\boldsymbol{\Theta} = \boldsymbol{\theta} \boldsymbol{\theta}^H$, it is a positive semi-definite rank one matrix.

The problem of maximizing the minimum signal power can then be formulated as

P1

$$\max_{\boldsymbol{\Theta}} z \tag{2.49}$$

$$\text{s.t. } \text{tr}(\boldsymbol{\Theta} \mathbf{h}_{ui} \mathbf{h}_{ui}^H) \geq z, \forall i = 1, \dots, N_u, \tag{2.50}$$

$$\text{tr}(\boldsymbol{\Theta}) \leq M \tag{2.51}$$

$$\boldsymbol{\Theta} \succeq 0 \tag{2.52}$$

$$\text{rank}(\boldsymbol{\Theta}) = 1, \tag{2.53}$$

where z is an auxiliary variable. Problem **P1** is not a convex problem. We apply semidefinite programming (SDP) relaxation to approximately solve this problem. Then it can be optimally solved by existing convex optimization toolboxes such as CVX [42].

In general, the solution of the rank-relaxed problem may not have a rank equal to one. Thus, we need to construct a rank-one solution to **P1**. Firstly, we calculate the eigenvectors of the phase shift matrix by the eigenvalue decomposition $\boldsymbol{\Theta} = \mathbf{U} \boldsymbol{\Sigma} \mathbf{U}^H$. Then the phase shifts can be set as equal to the complex-phase shifts of the eigenvector corresponding to the largest eigenvalue $\boldsymbol{\varphi} = \mathbf{U}(:, 1)$. Finally, we get the phase shifts at the RIS as $\boldsymbol{\Phi} = \text{diag}(\exp(j \arg(\boldsymbol{\varphi})))$.

Now we come to the 2nd step, to select \mathbf{f}_i after knowing $\boldsymbol{\Phi}$. Let

$$\mathbf{h}_{itot} = \mathbf{h}_i^H + \mathbf{h}_{ui}^H \boldsymbol{\Phi} \mathbf{H}, \tag{2.54}$$

the beamformer \mathbf{f}_i can be calculated as

$$\mathbf{f}_i = \frac{\mathbf{h}_{itot}^H}{\|\mathbf{h}_{itot}\|} \cdot \frac{1}{\sqrt{N_u}}, \tag{2.55}$$

here, we normalize \mathbf{f}_i to guarantee that the total transmit power equals 1.

MRT-based alternating optimization

The idea of this alternating optimization is to optimize the beamformers and phase shifts in an iterative manner, where the optimal solutions for one parameter are derived in closed form with the other being fixed. The basic process is: 1st, initialize a random $\mathbf{f}_i^{(0)}$. 2nd, run the alternating optimization loop until the phase shifts

become converged.

In the alternating process, we first optimize the phase shift matrix Φ in a similar way as in the approach of MRT-based heuristic without alternating optimization and get the result at the k th iteration as $\Phi^{(k)}$, where $k \geq 1$. After that, we update $\mathbf{h}_{\text{tot}}^{(k)}$ and $\mathbf{f}_i^{(k)}$.

To optimize Φ in step 2, we use the same process as in (2.47) and (2.48):

$$|\mathbf{h}_{ui}^H \Phi \mathbf{H} \mathbf{f}_i^{(k)}|^2 = \text{tr}(\Theta \mathbf{h}_{i\text{RIS}}^{(k)} (\mathbf{h}_{i\text{RIS}}^{(k)})^H), \quad (2.56)$$

where $\mathbf{h}_{i\text{RIS}}^{(k)} = \mathbf{h}_{ui}^* \odot \mathbf{h}_{i\text{eff}}^{(k)}$.

The optimization problem can be formulated as

P2

$$\max_{\Theta} z \quad (2.57)$$

$$\text{s.t. } \text{tr}(\Theta \mathbf{h}_{i\text{RIS}} \mathbf{h}_{i\text{RIS}}^H) \geq z, \forall i = 1, \dots, N_u, \quad (2.58)$$

$$\text{tr}(\Theta) \leq M \quad (2.59)$$

$$\Theta \succeq 0 \quad (2.60)$$

$$\text{rank}(\Theta) = 1. \quad (2.61)$$

Next, we follow the same process as in the first approach, doing the eigenvalue decomposition to get $\Phi^{(k)}$. Then we examine if the results are converged. The convergence criterion is set as $\sum(|\text{diag}(\Phi^{(k)}) - \text{diag}(\Phi^{(k-1)})|^2) \leq L/100$. If the convergence is achieved the alternation will be ended, otherwise, we update the total channel information $\mathbf{h}_{\text{tot}}^{(k)}$ and the beamformers $\mathbf{f}_i^{(k)}$ according to (2.54) and (2.55).

ZF-based optimization

Since the MRT beamforming cannot cancel the inter-user interference and thus results in low SINRs, we propose a ZF-based optimization approach to maximize the minimum signal power and increase the minimum SINRs.

We calculate the ZF beamformers based on the RIS-phase shifts that have been obtained by the approaches of MRT-based heuristic without alternating optimization and MRT-based alternating optimization. I.e., we set the RIS-phase shifts according to the optimization problems (2.49), resp. (2.57), assuming in the latter case that the BS applies MRT (for (2.49) we assume unknown beamformers). We have not been able to formulate an optimization target for RIS-phase shift optimization that leads to convergence when combined with ZF beamforming at the BS. Therefore, instead, we optimize the RIS-phase shifts first under the assumption of MRT, and after that, we replace the MRT beamformers with ZF beamformers. Therefore, in ZF-based optimizations, the beamformers are not optimized.

The design of ZF beamforming satisfies the following constraints:

1. The ZF beamformer is designed to achieve zero interference between the users,

i.e., $\mathbf{h}_{itot}\mathbf{f}_j = 0, \forall j \neq i$. The ZF beamformer employed at the BS is written as

$$\tilde{\mathbf{F}}_{ZF} = \mathbf{H}_{tot}^\dagger = (\mathbf{H}_{tot}^H \mathbf{H}_{tot})^{-1} \mathbf{H}_{tot}^H, \quad (2.62)$$

where $\mathbf{H}_{tot} = [\mathbf{h}_{1tot}^T, \dots, \mathbf{h}_{N_u tot}^T]$ is an $N_t \times N_u$ channel matrix, which gathers all the N_u column vectors \mathbf{h}_{itot}^T . $\tilde{\mathbf{F}}_{ZF}$ is an $N_u \times N_t$ matrix. Depending on the rank of the total channel rank $(\mathbf{H}_{tot}) \leq \min(N_t, N_u)$, $\tilde{\mathbf{F}}_{ZF}$ satisfies $\tilde{\mathbf{F}}_{ZF} \mathbf{H}_{tot} = \mathbf{I}$ when $N_u \leq N_t$ (see Appendix A in [43]).

2. The individual beamforming vectors for user i is $\tilde{\mathbf{f}}_{iZF} = \tilde{\mathbf{F}}_{ZF}^T(:, i)$.
3. The ZF beamformer needs to be normalized to satisfy the total transmit power constraint, i.e.,

$$\mathbf{f}_{iZF} = \frac{\tilde{\mathbf{f}}_{iZF}}{\|\tilde{\mathbf{f}}_{iZF}\|} \cdot \frac{1}{\sqrt{N_u}}. \quad (2.63)$$

Max-min SINR based optimization

The previous approaches are power-based optimization. In this section, we attempt to maximize the minimum SINR for all users so that if the SINR of one user is better than the SINR of another one, we could simply reduce the power of the first user and increase the power of the second user until both users have the same SINR. Thereby, the minimum of the two SINRs would go up, thus achieving a max-min SINR solution.

The SINR calculation in (2.45) can be rewritten as

$$\text{SINR}_i = \frac{|\mathbf{h}_{itot}\mathbf{f}_i|^2}{\sum_{j \neq i}^{N_u} |\mathbf{h}_{itot}\mathbf{f}_j|^2 + \sigma_i^2}. \quad (2.64)$$

In this approach we consider fixed RIS-phase shifts, i.e., we use the RIS-phase shifts obtained from the two MRT-based optimization approaches, respectively. Hence, the effective channel is fixed for the users, only the beamformers are optimized here. The goal of this optimization is to maximize the minimum SINR of all users:

$$\max_{\mathbf{f}_i, \forall i} \min_{i=\{1, \dots, N_u\}} \text{SINR}_i, \quad (2.65)$$

$$\text{s.t.} \quad \sum_i^{N_u} \|\mathbf{f}_i\|^2 \leq 1. \quad (2.66)$$

However, we cannot directly optimize this problem with respect to the beamformers, since it is not a convex optimization problem. But a convex reformulation is possible. First, we introduce the following feasibility problem.

P3

$$\min P_{tot} \quad (2.67)$$

2.2. Optimization of RIS-assisted MIMO systems

$$\text{s.t. } \text{SINR}_i \geq z, \forall i = 1, \dots, N_u. \quad (2.68)$$

$$P_{\text{tot}} = \sum_i^{N_u} \|\mathbf{f}_i\|^2 \quad (2.69)$$

$$P_{\text{tot}} \leq 1. \quad (2.70)$$

Here P_{tot} is the transmit power. Now the problem is to minimize the transmit power while making sure that the SINR is not less than a lower bound z . By combining this feasibility problem with a bisection search over the lower bound z , we can find the solution to (2.65).

For this bisection, we firstly set a lower bound of bisection search for SINR_i as $z_{lb} = 0$ and an upper bound, e.g., $z_{ub} = 50/\sigma^2$. Then we select a z between the lower bound and upper bound as $z = (z_{lb} + z_{ub})/2$. After this step, we solve the optimization problem **P3** and update the lower bound or upper bound of z , which depends on whether the problem is feasible or not. If it is infeasible, we reduce the upper bound of the bisection as $z_{ub} = z$, if it is feasible, we increase the lower bound of the bisection as $z_{lb} = z$ and update the current best beamformers and signal power P_{tot} . The new z will be a value between the new upper bound and lower bound $z = (z_{lb} + z_{ub})/2$. Then we solve **P3** again and update the lower bound or upper bound of z again. By this process we shrink the interval until we find the largest z that leads to a feasible solution to this optimization.

In order to solve **P3**, a further reformulation of the problem is required to obtain a convex optimization problem. The received signal power can be written as $|\mathbf{h}_{\text{itot}}\mathbf{f}_i|^2$. For any beamformer \mathbf{f}_i , we can define w.l.o.g. the following beamformer

$$\tilde{\mathbf{f}}_i = \mathbf{f}_i e^{-j \arg(\mathbf{h}_{\text{itot}}\mathbf{f}_i)}, \quad (2.71)$$

which ensures that the signal power is purely real-valued [44]. I.e., the received power is invariant w.r.t. the absolute phase of the beamformers:

$$|\mathbf{h}_{\text{itot}}\mathbf{f}_i|^2 = |\mathbf{h}_{\text{itot}}\tilde{\mathbf{f}}_i|^2. \quad (2.72)$$

This allows a reformulation of the SINR in terms of the real part of the signal. Therefore, we can rewrite the constraints (2.68) as

$$\frac{\Re(\mathbf{h}_{\text{itot}}\mathbf{f}_i)}{\sqrt{\sum_{j \neq i}^{N_u} |\mathbf{h}_{\text{itot}}\mathbf{f}_j|^2 + \sigma_i^2}} \geq \sqrt{z} \quad (2.73)$$

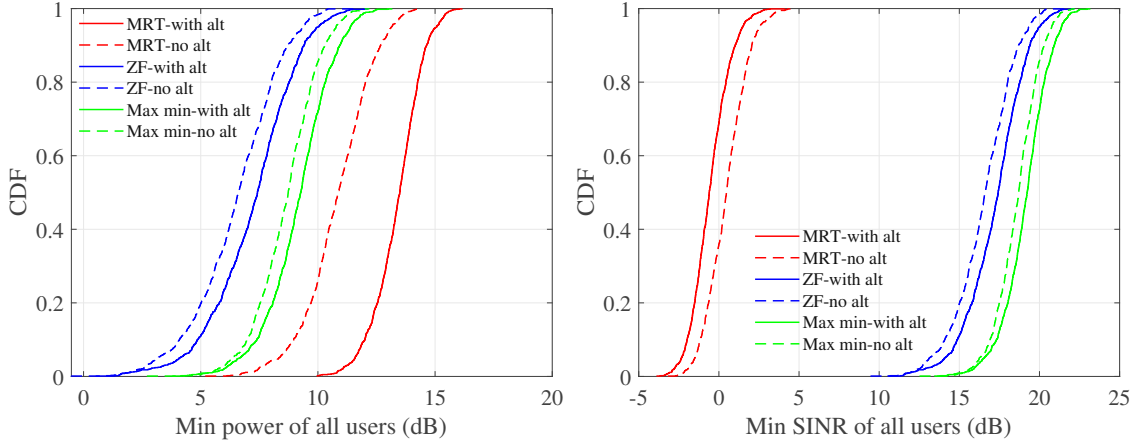
$$\Im(\mathbf{h}_{\text{itot}}\mathbf{f}_i) = 0. \quad (2.74)$$

Enforcing the imaginary part to be equal to zero is equivalent to the phase rotation in (2.71).

Let vector

$$\mathbf{g}_i = \left[\mathbf{h}_{\text{itot}}\mathbf{f}_j, \sqrt{\sigma_i^2} \right]_{j \in \{1, \dots, N_u\}, j \neq i}^T, \quad (2.75)$$

2.2. Optimization of RIS-assisted MIMO systems



(a) Minimum power without phase quantization. (b) Minimum SINR without phase quantization.

Figure 2.10: Results without phase quantization.

where $\mathbf{g}_i \in \mathbb{C}^{N_u \times 1}$ gathers all the sum-terms in the denominator of SINR_i i.e., the interference from other users and the noise variance. Then (2.73) can be reformulated as

$$\frac{\Re(\mathbf{h}_{i\text{tot}}\mathbf{f}_i)}{\sqrt{z}} \geq \|\mathbf{g}_i\|. \quad (2.76)$$

Now the optimization becomes a convex problem and can be solved by CVX.

2.2.3 Performance evaluation results

In this section, we present numerical evaluations of the signal power, SINR, and rate achieved from the different optimization approaches, as well as the results when we consider unquantized RIS-phase shifts and quantized phase shifts. Since the external control signal is generated by the digital-to-analog converter (DAC) with discrete output characteristics, the phase shift of each element of the RIS is discrete in practice [45]. The results of quantized phase shifts are obtained by applying the same algorithms proposed in Sect. 2.2.2, but replace the continuous RIS-phase shifts with quantized phase shifts. For example, when we choose $\frac{\pi}{2}$ as phase resolution, the phase shift set will be $[0, \frac{\pi}{2}, \pi, \frac{3\pi}{2}, 2\pi]$, for $\frac{\pi}{3}$, the phase shift set is $[0, \frac{\pi}{3}, \frac{2\pi}{3}, \pi, \frac{4\pi}{3}, \frac{5\pi}{3}, 2\pi]$, and so on. Accordingly, the beamformers are calculated based on the quantized phase shifts.

In the simulation, we consider a number of $N_t = 10$ antennas at BS to serve $N_u = 5$ single-antenna users. The RIS contains $M = 10$ elements. The noise variance is set as $\sigma_i^2 = 0.1$. We consider a Rayleigh fading channel model, which means that all channels are uncorrelated (the direct channels are uncorrelated from the RIS-assisted channels and the RIS-assisted channels of different users are also uncorrelated). Hence, we do not adopt a geometry-based channel model in this paper. This is justified for scenarios with strong scattering, e.g., indoors, as well as, outdoors in dense scenarios such as urban streets. After 1000 times random realizations, we plot

2.2. Optimization of RIS-assisted MIMO systems

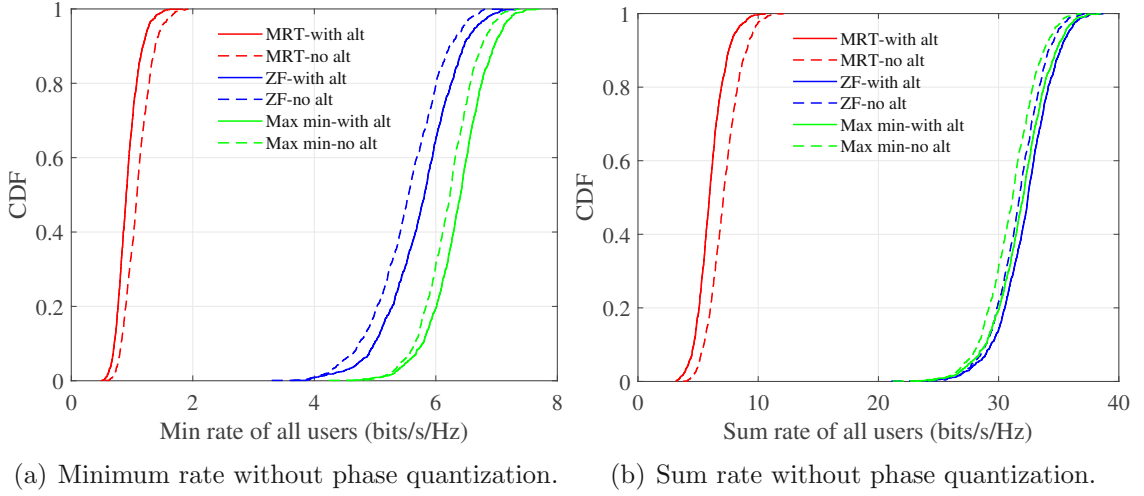


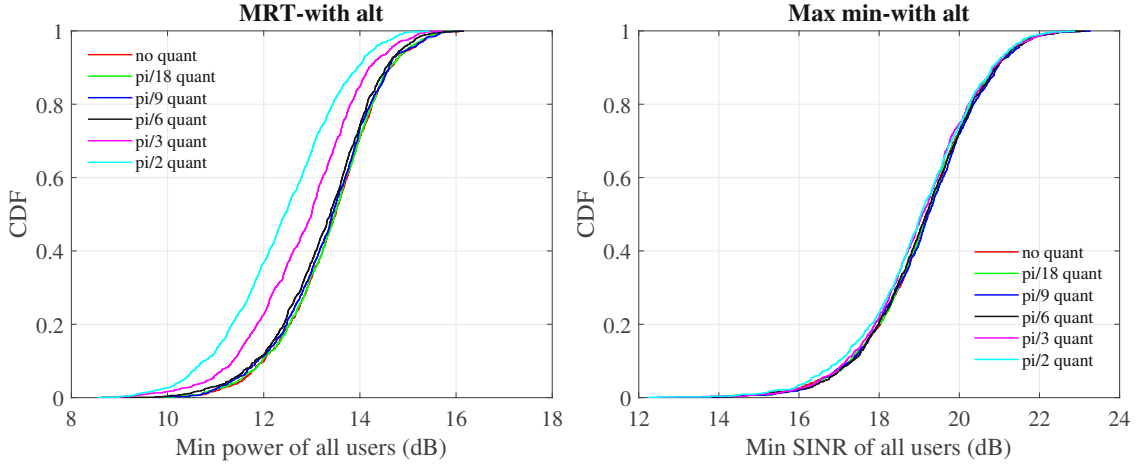
Figure 2.11: Results without phase quantization.

the cumulative distribution function (CDF) of the signal power, SINR, and achieved minimum rate and sum rate from different approaches in Fig. 2.10(a), Fig. 2.10(b), Fig. 2.11(a) and Fig. 2.11(b), respectively. In these figures, the RIS-phase shifts are assumed to be continuous.

Here in the figures, “Max min-with alt” stands for the max-min SINR approach with Φ obtained from MRT-based alternating optimization. Whereas “Max min-no alt” stands for the max-min SINR approach with Φ obtained from MRT based heuristic without alternating optimization. Similar for “ZF-with alt” and “ZF-no alt”. From these figures, we can observe that the MRT-based optimization can achieve the highest minimum signal power among other approaches, whereas the max-min SINR approach can achieve the highest minimum SINR and minimum rate. The ZF and max min SINR approaches can achieve similar sum rates. Also, the minimum rate of them does not have too much difference. However, except for the signal power, the SINR and rate obtained by the MRT approach have the lowest values among others. Moreover, the alternating optimization is shown to achieve higher power, higher SINR and rate than that without alternating optimization for both the ZF and max min SINR methods. For the MRT approach, the alternating optimization performs worse for SINR and rate but better for signal power.

In Fig. 2.12(a) and Fig. 2.12(b), we compare the minimum signal power achieved by the MRT-based alternating optimization, i.e., the approach of “MRT-with alt”, as well as the minimum SINR obtained by the approach of “Max min-with alt”, respectively. The results are obtained with/without phase shift quantization. From the two figures, we can observe that when the phase quantization resolution is getting higher, the minimum signal power will be closer to that without phase quantization. However, the SINR does not increase monotonically with the phase resolution. The reason is that we maximize the minimum signal power at the RIS, whereas at the BS we maximize the minimum SINR. Apparently, maximizing the minimum signal power (as achieved by the unquantized RIS phases) does not directly help in im-

2.3. Final remarks



(a) Minimum signal power with phase quantization. (b) Minimum SINR with phase quantization.

Figure 2.12: Results with phase quantization.

proving the minimum SINR. Therefore, in the future, other optimization strategies at the RIS, which lead to an enhancement of the SINR, have to be investigated.

In summary, we propose several optimization approaches, i.e., MRT with or without alternating optimization, ZF, and max-min SINR optimization, to optimize the beamformers at BS and the phase shifts at RIS for an RIS-assisted MIMO system. Through the simulation results of the different approaches, we find the MRT-based optimization can achieve higher signal power than other approaches, while ZF and max min SINR methods perform similarly with much higher minimum SINR and rate than MRT optimization. We have also investigated the impact of quantized RIS phases, showing that the performance of the MRT-based scheme improves monotonically with increasing phase resolution. When the resolution becomes high enough, the quantized RIS phase will perform almost the same as when the phase shifts are not quantized.

2.3 Final remarks

With the rapid speed of RIS-related studies, system-level simulation is urgently needed to evaluate the performance of RIS-aided wireless networks. This section introduces the RIS module implemented in the Vienna 5G SLS, where many challenges for RIS-based wireless networks at the system level have been considered. Especially the RIS modeling, RIS deployment, macroscopic fading, small-scale fading, cell association, and RIS phase shift optimization are explained. In addition, we integrate the RIS-tailored Vienna SLS with the MATLAB ray tracer to obtain more accurate results in realistic scenarios. Two path loss models for RIS-assisted links from the communication field are implemented in the simulator, and the system performance has been verified with theory in an SISO scenario. After the verification of the RIS

2.3. Final remarks

implementation in the simulator, we can use the Vienna SLS for simulations in more complex scenarios.

In the current version of the Vienna SLS, the RIS phase shifts can be optimized for a SISO scenario, but there can only be random variables for MU-MIMO scenarios. However, we propose several approaches to optimize the beamformers at the BS and the phase shifts at the RIS for an RIS-assisted MIMO system. By comparing the minimum signal power, minimum SINR, and rate achieved by the proposed MRT, ZF, and max-min SINR based optimizations, we conclude that the MRT-based optimization can achieve the highest minimum signal power among other approaches, whereas the max-min SINR optimization can achieve the highest minimum SINR and minimum rate. In addition, the effect of quantized RIS-phase shifts is analyzed, showing that almost optimal performance can be achieved with relatively high phase resolution.

Since the Vienna SLS is a huge package including many different modules and functions, the abovementioned optimization algorithms in the simulator will heavily influence other modules and severely increase the simulation time. However, the simulator serves as a flexible and general tool for users; different users may have different optimization problems and methods. Hence, it is not of significant priority to include our algorithms in the simulator. Our algorithms are just one example among plenty of optimization approaches, and the users can use their own algorithms in the simulator when necessary. In the future, when the simulation time and complexity issues are solved, different optimization approaches for RIS-assisted MU-MIMO scenarios can be implemented in the SLS.

3

RIS electromagnetic model and its application

In wireless communication systems, propagation channels need to be optimized to avoid any blind spots where the signal is too weak for serving users. One of the methods is to deploy more base stations or add active relays between the base stations and the users. However, adding active antennas is expensive and complicated. The other option is to use passive antenna structures, such as nearly passive RISs and fully passive metal reflectors since they are compatible with existing and future wireless systems, and their energy consumption is very low or almost zero [16].

However, either using an RIS or a metal reflector requires the plate to be oriented in such a way that the scattered beams point toward the desired user. In addition, metal plates produce specular reflection; in other words, a signal can only be received when the observation angle is close to the incident angle [46]; any modification in the desired reflection direction would require manual re-orientation of the plate. Therefore, these approaches are not universal and may be inconvenient, involving human control or complex algorithms. From Chapter 2 we know that with an untuned RIS (not optimized for any desired direction), the received power at the user can achieve a 3 dB gain when doubling the RIS element number according to the power scaling law [17, 30]. Inspired by this concept, we aim to find other more convenient and realistic alternatives that can improve the received power by the user without extra control from humans.

In fact, we have identified an alternative of deploying a number of static scatterers in the form of resonant dipoles. These additional scatterers enhance the propagation environment by re-radiating signal waves in all directions. We find that just randomly deploying multiple resonant dipoles as scatterers in the environment can achieve similar results as expected for an untuned RIS. This method is very cheap and convenient since it does not require any signal processing or optimization, yet, it can offer significant improvements in coverage. In the first part of this chapter, we explore in which scenarios it is beneficial to implement static scatterers and in which scenarios they do not offer significant improvements. In addition, we investigate how much improvement the user can receive through randomly located

scatterers and what parameters have a high impact. We explore the contribution of these scatterers in indoor and outdoor scenarios using a modified MATLAB ray tracing model.

Now that randomly located resonate dipoles can achieve similar results as if using an untuned RIS, what if we model an optimized RIS as an antenna array with each element being a resonant dipole? Can it achieve a similar gain as we obtain in Chapter 2 with the RIS CM model? These questions bring out a new path loss model for RIS derived from the electromagnetic theory. As path loss modeling builds an essential connection between the communication and electromagnetic aspects of RIS studies, understanding electromagnetic wave reflections from RIS and modeling signal propagation via RIS reflections in the communication system and software are of significant importance.

There are already several path loss models for RIS proposed in recent years. For example, the authors of [40, 47] proposed a system model for RIS-assisted wireless communications, based on the local reflection coefficient model and the notion of gains of the individual array elements. In the assumption that the reflection phase distribution is optimal for reflection into the desired direction. That model has been implemented and adapted to the Vienna SLS for its RIS module. A physics-consistent analytical model in the presence of an RIS is proposed in [48], which is a free-space path loss model based on the vector generalization of Green's theorem. In [7], the authors used physical optics techniques to derive the path loss model for an RIS that is configured to reflect an incoming wave from a far-field source towards a receiver in the far-field. In [49], simple link budget formulas are derived from electromagnetic solutions for optimally functioning anomalous reflectors, where the collective nature of reflection phenomena was accounted for, and the notion of the local reflection coefficient was not used.

However, there is no deep investigation into these different path loss models for RIS in the literature, and there is no systematic analysis and comparison of the path loss models from the communication and electromagnetic points of view. The RIS modeling and path loss modeling for RIS-assisted links from both aspects are usually not consistent since they use different assumptions and theories. It is essential to find out the differences, gaps, and connections between the communication and electromagnetic aspects of RIS-related studies. Therefore, in the second part of this chapter, we compare the previously introduced RIS CM model from communication theory with a path loss model for RIS derived from the electromagnetic theory, namely, the RIS EM model. We discuss the differences and similarities between these two models, as well as the use cases for them. Finally, we verify our analysis with simulation results. The work described in this chapter is published/accepted in [20–22].

3.1 Improving propagation channels with static scatterers

In this section, we consider the possibility of improving the propagation of radio signals in complex environments using a set of simple purely passive resonant dipole scatterers. We first introduce a necessary modification of the path loss model used for the scatterers in the MATLAB ray tracer, which is based on the bistatic scattering cross-section of dipolar scatterers. Next, we run ray tracing simulations in two indoor scenarios, one with a strong direct link and the other one without a direct link, as well as one outdoor scenario to analyze the influence of the scatterers on the received power at the user position.

3.1.1 Theoretical analysis

We use resonant dipoles (for example, half-wave metal wire or strip dipoles) as scatterers since they are low-cost, very simple to implement, and have an omnidirectional radiation pattern in the azimuthal plane. By placing multiple dipoles randomly in the environment, we can achieve random phases of waves scattered from them. When a dipole with its load is at resonance and there is no resistive loss, the scattered power is maximized [50]. In this case, the scattering cross-section of the dipole is $\delta_{\max} = 4A_e G$, where A_e is the effective area, and G is the gain of the dipole. When the dipole load is conjugate-matched, $\delta_{\text{match}} = A_e G$ [51]. Therefore, in this paper, we use short-circuited resonant dipoles to scatter as much power as possible.

By applying the definition of the scattering cross-section, we can infer that the transmitted power is first captured by the target and subsequently reradiated isotropically. The power delivered to the receiver load P_r is calculated by the radar range equation [39]:

$$P_r = \frac{P_t G_t G_r \delta \lambda^2}{64\pi^3 (d_t d_r)^2}, \quad (3.1)$$

with P_t being the transmitted power and δ is the radar cross-section of the scatterer. Furthermore, G_t and G_r are the gains of the Tx and the Rx antennas, respectively. d_t and d_r denote the distances between the Tx and the scatterer and between the scatterer and the Rx antenna, respectively. However, this model considers a free-space scenario, with only one LOS path between the Tx antenna and the scatterer, and between the scatterer and the Rx antenna. In a real environment, multipath propagation through reflections cannot be ignored. Therefore, we use the MATLAB ray tracer to obtain more accurate received power, which takes the reflection from the environment and losses due to the types of reflection materials into account.

In a LOS scenario, the received power at the Rx antenna from the Tx-dipole-Rx

3.1. Improving propagation channels with static scatterers

link is calculated based on the Friis formula in the MATLAB ray tracer:

$$P_r = P_t \frac{G_t G_{rx} \lambda^2}{(4\pi d_t)^2} \frac{G_{tx} G_r \lambda^2}{(4\pi d_r)^2} = \frac{P_t G_t G_r G_{tx} G_{rx} \lambda^4}{(4\pi)^4 (d_t d_r)^2}, \quad (3.2)$$

with G_{tx} and G_{rx} being the gain of the scatterer towards the directions of the Rx and the Tx antennas, respectively. For reciprocal scatterers, $G_{tx} = G_{rx} = G$. Eq. (3.2) holds the assumption that the load of the scattering antenna is conjugate-matched. As discussed above, in that case, the scattered power is not at its maximum, because the currents flowing at the antenna body are weaker if there is a resistive load. Basically, Eq. (3.2) corresponds to the radar-range equation (3.1) where $\delta = \delta_{\text{match}}$.

Since the difference of δ for lossless resonant and conjugate-matched dipoles is a factor of four, the correct model from ray tracing should be

$$P_r = \frac{4P_t G_t G_r G_{tx} G_{rx} \lambda^4}{(4\pi)^4 (d_t d_r)^2}. \quad (3.3)$$

We stress that Eq. (3.3) is valid only for resonant lossless dipoles, while Eq. (3.1) can be used for arbitrary scatterers.

Now when we consider a multipath propagation scenario, the received power for the Tx-Rx, dipole-Rx, and Tx-dipole links is calculated the same as (2.19)-(2.21) in Chapter 2 when we replace the RIS with a dipole. The reflection losses due to different material types are also included in the path loss calculation in the MATLAB ray tracer. The final received power at the Rx antenna can be classified as from the direct link, i.e., from the Tx antenna to the Rx antenna only through wall reflections, and from the dipole-assisted link, that is, the transmitted signals are reflected by dipoles and then reach the Rx antenna. There are also wall reflection paths from the Tx antenna to the dipole and from the dipole to the Rx antenna in the dipole-assisted link.

The received power at the Rx antenna from Tx through wall reflections is denoted as P_d . The received power from all the dipoles is denoted as P_{dip} , and the total received power from both the direct link and from all dipoles is written as

$$P_{\text{tot}} = P_d + P_{\text{dip}} \quad (3.4)$$

in Watt. The contribution due to the dipoles is denoted as

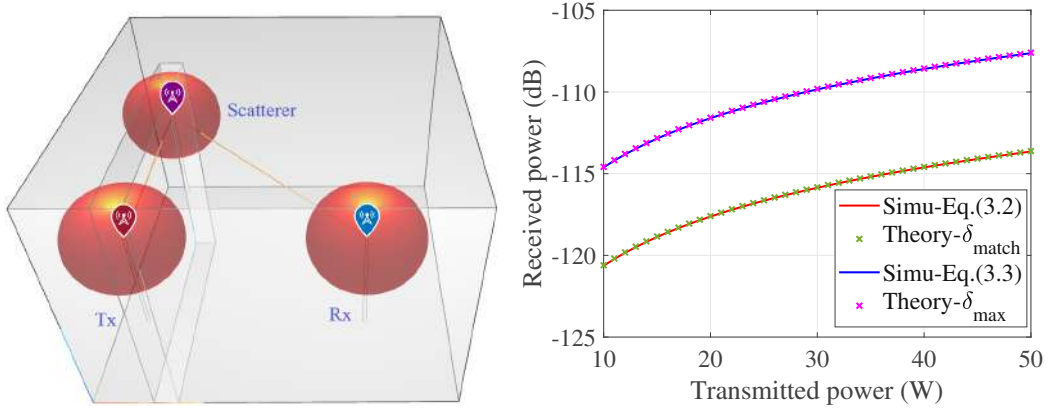
$$\rho = P_{\text{tot}}/P_d \quad (3.5)$$

in linear scale. Assuming there are in total R dipoles, the P_{dip} is calculated as

$$P_{\text{dip}} = \sum_{r=1}^R 4P_{ur,r}, \quad (3.6)$$

where $P_{ur,r}$ is the received power at the Rx antenna from the r -th dipole and is

3.1. Improving propagation channels with static scatterers



(a) A SISO scenario with 3 dipoles being the Tx, Rx, and the scatterer. (b) Comparison of ray tracing simulation results and theoretical results.

Figure 3.1: Comparison of simulation and theoretical results in a SISO scenario.

calculated by (2.20). The factor of four in Eq. (3.6) is the correction factor for the radar cross-section of a lossless resonant dipole, see Eq. (3.3).

To verify this model, we set up a simple SISO scenario as shown in Fig. 3.1(a) and use the MATLAB ray tracer to calculate the received power. In the simulation, we use a resonant dipole as a Tx and Rx antenna, and the same dipole as a scatterer. The resonant frequency is 30 GHz, and the maximum gain of the dipole is 2.1 dB. According to the relation between the antenna gain and the effective area,

$$A_e = G\lambda^2/(4\pi), \quad (3.7)$$

we can calculate

$$\delta_{\max} = 4A_e G = 4G^2\lambda^2/(4\pi) = 0.8372\lambda^2, \quad (3.8)$$

and

$$\delta_{\text{match}} = A_e G = G^2\lambda^2/(4\pi) = 0.2093\lambda^2. \quad (3.9)$$

In the scenario where the Tx and Rx antennas are blocked, there is only one LOS path between Tx and the scatterer and one LOS path between the scatterer and the Rx. For the distances $d_t = 2$ m and $d_r = 2.8$ m, the received power from Eq. (3.1) with $\delta = \delta_{\max}$ and $\delta = \delta_{\text{match}}$, Eq. (3.2), and Eq. (3.3) are shown in Fig. 3.1(b). The results show that the original ray tracing model from Eq. (3.2) gives the same results as if we use $\delta = 0.2093\lambda^2$ in Eq. (3.1). The modified ray tracing model from Eq. (3.3) gives the same results as the correct theoretical model from Eq. (3.1) with $\delta = 0.8372\lambda^2$. In the following simulations, we use the modified ray tracing model (3.6) to calculate the received power at the Rx antenna.

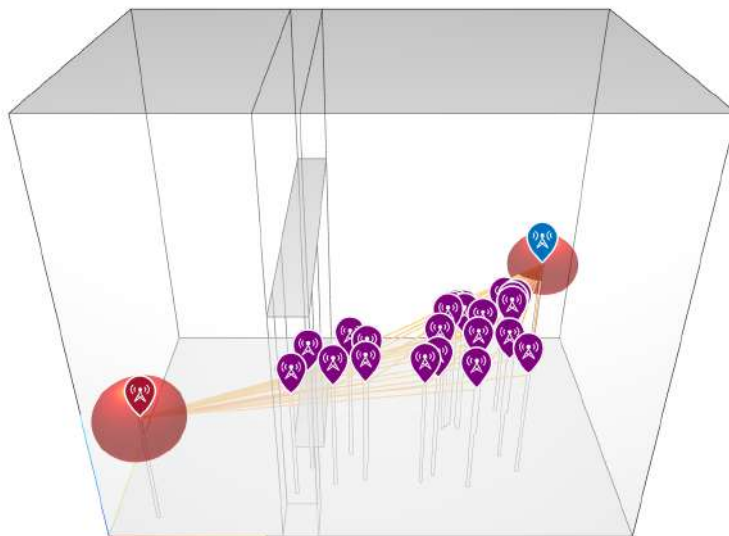


Figure 3.2: An indoor room scenario with a strong direct link. The red, blue, and purple markers represent the Tx, Rx, and dipoles, respectively.

3.1.2 Ray tracing simulations

Indoor scenario with a strong direct link

Firstly, we set up an indoor two-room scenario for MATLAB ray tracing simulation, as shown in Fig. 3.2. A big room with the size of $6 \times 4 \times 5 \text{ m}^3$ corresponding to the length \times width \times height is separated from a small room ($2 \times 4 \times 5 \text{ m}^3$ and $3.6 \times 4 \times 5 \text{ m}^3$) by an open door in between. The Tx and Rx antennas are located in different rooms. Between them, there are 23 randomly placed dipoles. The heights of the Tx, Rx, and dipoles are all 1.5 m. The dipoles and the Tx and Rx antennas are all in the far-field of each other. There are no LOS paths between the Tx and Rx antennas, but there are strong reflection paths from the walls that can reach the Rx antenna. Each dipole has LOS connections with both the Tx and Rx antennas.

When considering the reflections from the environment, different wall materials can cause different reflection losses. Therefore, we set the material as “Concrete”, “Plasterboard”, “Wood”, and “Ceiling board”, respectively, to observe their influences. The simulation results with one reflection and three reflections at 30 GHz are displayed in Table 3.1 and Table 3.2, respectively. From both tables, we can observe that the direct link contributes much stronger power than the dipole-assisted link. In this case, the contribution from the dipoles is seen to be insignificant. The results with three reflections are better compared to the one reflection scenario due to more propagation paths, but the difference is not so significant since there are many destructive paths from the wall reflections. From the comparison of the four different materials, we find that the material loss from the lowest to the highest is “Concrete” $<$ “Plasterboard” $<$ “Wood” $<$ “Ceiling board”. The higher improvement from the dipoles can be seen when the material loss is higher.

3.1. Improving propagation channels with static scatterers

Table 3.1: Results with one reflection and different material types.

Material	Concrete	Plasterboard	Wood	Ceiling board
P_d (dB)	-81.2658	-83.7207	-86.5063	-89.9846
P_{dip} (dB)	-114.4580	-115.1207	-115.3476	-115.3150
P_{tot} (dB)	-81.2637	-83.7176	-86.5006	-89.9719
ρ (dB)	0.0021	0.0031	0.0057	0.0127

Table 3.2: Results with three reflections and different material types.

Material	Concrete	Plasterboard	Wood	Ceiling board
P_d (dB)	-82.1522	-85.0051	-87.8605	-90.9118
P_{dip} (dB)	-114.0701	-115.1212	-115.4183	-115.3106
P_{tot} (dB)	-82.1494	-85.0009	-87.8529	-90.8961
ρ (dB)	0.0028	0.0042	0.0076	0.0157

Table 3.3: Results with one reflection and different frequencies

Frequency (GHz)	10	30	60
P_d (dB)	-84.6241	-89.9846	-93.3166
P_{dip} (dB)	-95.5249	-115.3150	-127.0857
P_{tot} (dB)	-84.2848	-89.9719	-93.3148
ρ (dB)	0.3393	0.0127	0.0018

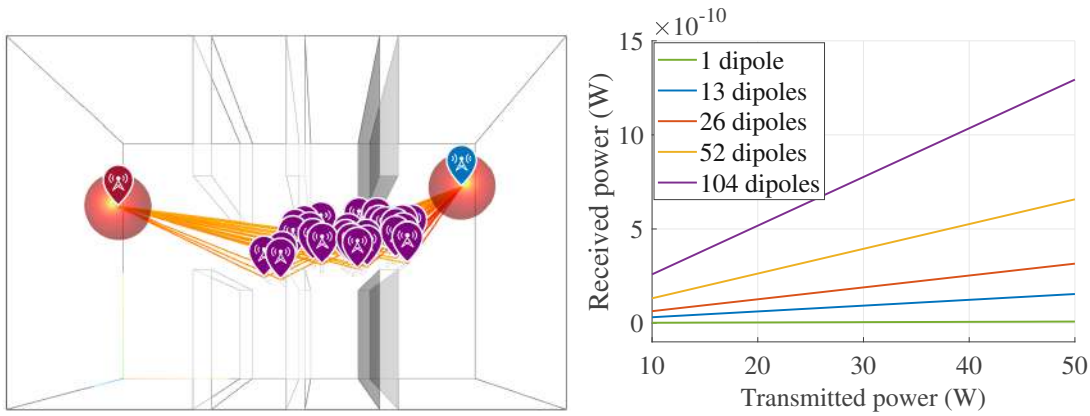
Next, we run simulations within the same scenario at the frequencies of 10 GHz and 60 GHz and set the material type as “Ceiling board” to compare the results with one reflection. The results are shown in Table 3.3. It is evident that at lower frequencies the received power is higher than at higher frequencies. The contribution from the dipoles at a lower frequency is also stronger than at a higher frequency. Hence, it is more useful to place scatterers in lower-frequency systems than at higher frequencies.

Indoor scenario without a direct link

In this section, we simulate a library scenario as shown in Fig. 3.3(a), where the direct link is totally blocked by six high shelves inside the room. The Tx and Rx antennas are placed at the two ends of the room, and several dipoles are randomly placed in the corridor. The material of this scenario is set as “Wood”, and we set three reflections in the simulation. It should be noted that, in this scenario, no reflection paths from the Tx antenna can reach the Rx antenna, even if we set the reflection number as six or higher. This refers to a completely blinded spot where the Rx antenna can only receive signals through the dipolar scatterers. Hence, the number of dipoles plays a key role in this scenario.

When the number of scatterers is zero, the received power at the Rx antenna is zero Watt no matter how much power is transmitted at the Tx antenna. Then

3.1. Improving propagation channels with static scatterers



(a) A Library scenario with the direct link being totally blocked. The red, blue, and purple markers represent the Tx, Rx, and dipoles, respectively. (b) Received power results with different numbers of dipoles in an indoor scenario without a direct link.

Figure 3.3: Simulation scenario and results when no direct link exists.

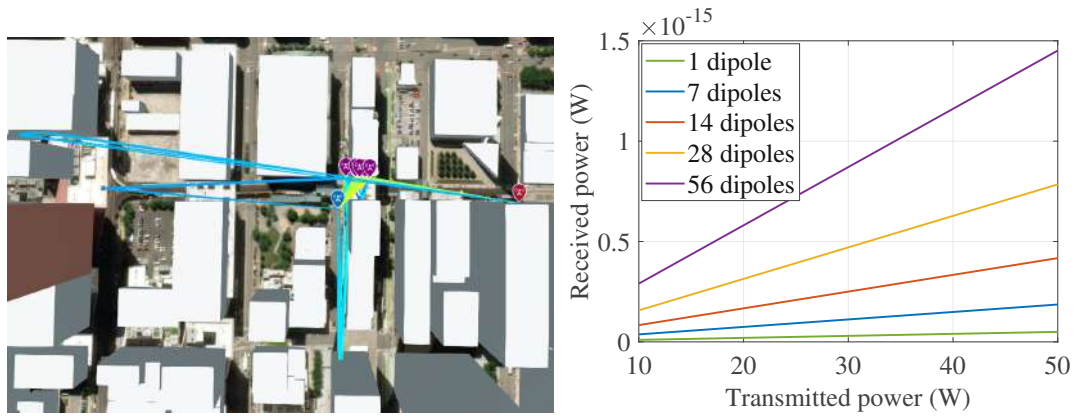
we change the number of dipoles as 1, 13, 26, 52, and 104 to observe the received power at the Rx antenna. The results are straight lines in linear scale as displayed in Fig. 3.3(b). The simulation results show that with a single dipole, the received power is very low and close to zero. When the number of dipoles grows large, the received power also increases a lot. For example, we can observe 3.11 dB, 3.19 dB, and 2.94 dB difference when the number of dipoles increases from 13 to 26, from 26 to 52, and from 52 to 104, respectively. Compared to the results for a model of an untuned RIS in [18], the received power improvement seen here is very close to 3 dB when doubling the number of dipoles. The reason for this agreement is that the model of an untuned RIS in [18] neglected field interactions between the RIS elements, which is a reasonable assumption for the studied case of randomly positioned dipoles.

Outdoor scenario without a direct link

In this section, we run ray tracing simulations in an outdoor scenario: a small part of the Chicago city exported from OpenStreetMap. The setup is shown in Fig. 3.4(a), in which we place the Tx and Rx antennas next to two buildings and place several dipoles on the street where the scattered waves can reach both the Tx and the Rx antennas. However, there is no reflection path between the Tx and the Rx antenna, i.e., the Rx antenna can only receive signals through the dipolar scatterers. It should be noted that the Tx and Rx antennas are all the same as the dipoles we placed on the street as static scatterers. The heights of them are also the same.

In the simulation, we set three reflections for both the Tx-dipoles and dipoles-Rx links and vary the number of dipoles to be 1, 7, 14, 28, and 56. The received power results for different numbers of dipoles are shown in Fig. 3.4(b). The received power

3.1. Improving propagation channels with static scatterers



(a) An outdoor scenario with the direct link being blocked. The red, blue, and purple markers represent the Tx, Rx, and dipoles, respectively. (b) Received power results with different numbers of dipoles in an outdoor scenario.

Figure 3.4: Simulation scenario and results in an outdoor environment.

with a single dipole is very low. The power difference between 14 and 7 dipoles is 3.51 dB. The difference between 28 and 14 is 2.74 dB, and the difference between 56 and 28 is 2.67 dB. It is found that the power difference with doubled dipole numbers is also close to 3 dB, but it has more deviations compared to the indoor scenario. In addition, when the number of dipoles increases, the differences get smaller. This is a more realistic situation because when the number of scatterers gets larger and larger, the gain cannot always increase by the same amount. Otherwise, the gain would reach infinity when the scatterer number grows infinitely, which is obviously wrong. From the comparison between the indoor and the outdoor scenario, we can conclude that the improvement due to the increase of the dipole numbers is higher in a rich scattering environment than in a sparse scattering environment.

Summary

In summary, this section explores the potential enhancement of radio signal propagation in intricate environments through the deployment of basic resonant dipole scatterers. With a modified ray tracing model based on the bi-static scattering cross-section of a short-circuited resonant dipole, we obtain simulation results in indoor and outdoor scenarios where the direct link is not blocked or totally blocked. By comparing the results with different reflection materials, different frequencies, and different numbers of dipoles, we conclude that the deployment of extra scattering components is nearly ineffective when a direct link is present. Conversely, in scenarios where there is no LOS path, the proposed approach can considerably boost the power delivered. This cost-effective and straightforward method could complement other channel optimization strategies, such as the application of RISs.

3.2 Communication and electromagnetic models for an optimized RIS

The path loss model is an essential connection between the communication and electromagnetic aspects of RIS studies. The accuracy of the path loss model for RIS is crucial for both communication and electromagnetic studies. Therefore, this section compares two path loss models for RIS that come from communication-theory and electromagnetic-theory considerations.

In Chapter 2, we introduced an RIS CM model that has been implemented in the Vienna SLS for RIS-assisted links, see Eq. (2.11), which is derived from the communication aspect. This model assumes a large-scale scenario where there are multiple BSs, RISs, and users. The BSs and the RISs are not assigned to any user yet, in other words, each user is not aware from which BS and RIS it will receive signals. The model does not account for directivity patterns of the BS, RIS, and the user antennas, although they may be included as angular dependencies of the corresponding gains. In this scenario, we define the RIS unit cells in a random configuration, as each RIS does not have any targeted user to serve.

This assumption is made due to the structure of the SLS that first calculates the large-scale fading of each BS-RIS-user link based on the distances between them. Then it performs cell association, to assign BSs to users according to the large-scale fading. Once each BS is assigned to some users, the RIS elements phase can be optimized to serve the associated BS-user pairs. The RIS phase shift optimization is a concept from the communication theory. Basically, it is assumed that the phase shifts of each unit cell are tuned to make them the same as the phase of the BS-user link so that the users can receive coherent, constructive signals from both the direct and RIS-assisted links. This step requires information on the small-scale fadings from the BS-RIS-user and BS-user links, hence, the RIS phase shifts optimization happens in a later step after the small-scale fading of each link is obtained.

After the RIS is optimized to serve the desired user in the desired direction, the received power at the desired user from the BS through the RIS is equivalent to

$$P_r = \frac{P_t G_t G G_r \lambda^2 L^2 A}{64\pi^3 (d_t d_r)^2}. \quad (3.10)$$

The difference of factors L^2 in Eq. (3.10) and L in Eq. (2.11) comes from the non-coherent combination of electric field for random RIS and coherent combination for optimized RIS, as explained in detail in Chapter 2.

In reality, however, RIS elements are strongly coupled, and reflection from RIS is a collective electromagnetic phenomenon that cannot be modeled in terms of effective areas and gains of array elements. It is important to learn to what extent and under what conditions such simplistic communication-theory models can be used.

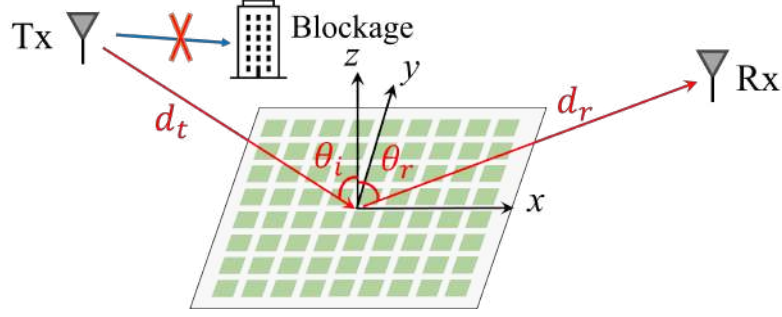


Figure 3.5: Illustration of the Tx-RIS-Rx path with the direct path between the Tx and the Rx being blocked.

3.2.1 Comparison between the RIS CM and EM models

A recent paper [49] introduces an electromagnetic model of links via RIS functioning as an anomalous reflector. For simplicity, we refer to it as RIS EM model. In this model, the RIS is modeled as a homogenizable metasurface, whose radiation pattern can be found in terms of the effective electric and magnetic surface currents induced on the metasurface. Under the metasurface framework, the optimized anomalously reflecting RIS carries only one propagating Floquet current harmonic that radiates into the desired direction and a set of evanescent Floquet modes whose field in the far zone can be neglected.

The simplest version of the path loss formula for far-zone links when reflections from supporting walls are negligible, reads

$$P_r = P_t G_t G_r \eta_{\text{eff}} \left(\frac{S_1}{4\pi d_t d_r} \right)^2 |\cos \theta_i \cos \theta_r|, \quad (3.11)$$

where the definitions of P_r , P_t , G_t , G_r , d_t , and d_r are the same as in Eq. (3.10). Efficiency $0 < \eta_{\text{eff}} \leq 1$ is a correction parameter for any loss caused by absorption, approximations in design, and imperfections of RIS implementations. Here, S_1 is the geometrical area of the RIS panel; θ_i and θ_r are the incident and reflection angles of signal waves at the RIS position. The angles are counted from the normal to the RIS plane. This model considers an ideal setup, where the RIS is optimized to provide anomalous reflection towards the user at θ_r from the incident waves at θ_i . An illustration of the Tx-RIS-Rx path is depicted in Fig. 3.5.

While the RIS CM model and the RIS EM model have many similarities, there are important differences:

- Note the presence of factor λ^2 and missing angular factors in Eq. (3.10).
- Note also that in the RIS EM model, there is no notion of gain of a single unit cell of a metasurface and that the product LA in Eq. (3.10) is in general not the same as the RIS area S_1 in Eq. (3.11).

The RIS CM model of Eq. (3.10) is derived from the assumption that the RIS is

formed by L small controllable scatterers, neglecting field interactions between the elements. Each element as a small antenna is characterized by its effective area A and gain G . That is, it is assumed that each small antenna receives power equal to the product of the effective area A and the amplitude of the Poynting vector at the antenna location and then re-radiates this power as a transmitting antenna with gain G . However, the received power is defined by the effective area only if the antenna is loaded by the matched load whose resistive part absorbs received power, while the very operational principle of reconfigurable RIS elements is that the antennas are loaded by tunable reactive loads. That is, the antennas are never matched and the received and re-radiated power is never equal to the available power at the antenna port.

As the simplest example, let us assume that the RIS is formed by small electric dipole antennas, arranged in a periodical lattice with the period equal to $\lambda/2$. Assuming $\eta_{\text{eff}} = 1$ and substituting $S_1 = L(\lambda/2)^2$ into Eq. (3.11) we get

$$P_r = \frac{P_t G_t G_r}{(4\pi d_t d_r)^2} \frac{L^2 \lambda^4}{16} |\cos \theta_i \cos \theta_r|. \quad (3.12)$$

Let us next substitute the corresponding values of the effective area and gain into (3.10) and compare the result with the received power calculated with the electromagnetically consistent model of a properly configured RIS of the same size, given by Eq. (3.12). The gain of a lossless electric dipole antenna equals $G = 3/2$, and the effective area can be found using the general relation between the effective area and gain of any reciprocal antenna $A = G\lambda^2/(4\pi)$. Note that the effective area is not equal to the geometrical area of the unit cell, which is, in our example, equal to $\lambda^2/4$. Substitution to Eq. (3.10) gives

$$P_r = \frac{P_t G_t G_r}{(4\pi d_t d_r)^2} \frac{9L^2 \lambda^4}{64\pi^2}. \quad (3.13)$$

We see that the difference between Eq. (3.12) and Eq. (3.13) is a multiplication factor $\frac{4\pi^2}{9} |\cos \theta_i \cos \theta_r|$. We can try to recover the angular factors assuming that the gain and effective area into the directions of illumination and re-radiation are proportional to the corresponding cosine factors (while in fact, the correct factors would be the cosine squared), but the amplitude of the received power is anyway far from the EM estimate of Eq. (3.11). Importantly, let us stress again that in this CM model, the reflection phase for each antenna element is the same, the one of an antenna tuned to its resonance by loading its port by the complex-conjugate impedance. That is, while the RIS is assumed to be tuned to coherently reflect into the desired direction, the model is for a set of identical dipoles tuned to the resonance. Actually, the effective area and gain are not appropriate parameters for describing the response from passive scatterers, the appropriate parameter is the bi-static scattering cross-section [39, 52].

On the other hand, if we arbitrarily assume that the effective area of a single element equals the geometrical area of the unit cell ($\lambda^2/4$ in our example) scaled

by the angular factor $\cos \theta_r$ and calculate the corresponding gain as $G = 4\pi A/\lambda^2$, scaled by $\cos \theta_i$, we get the same result as the EM model of Eq. (3.11)! Indeed, the equation takes the form

$$P_r = \frac{P_t G_t G_r (LA)^2}{(4\pi d_t d_r)^2} |\cos \theta_i \cos \theta_r|. \quad (3.14)$$

The factor LA in this equation is the total area of the RIS (if we assume that the unit cells have no gaps between them), which is the same as S_1 in Eq. (3.11). Now, the only difference between Eqs. (3.14) and (3.11) is the correction parameter η_{eff} . When we include this parameter in Eq. (3.14), the two models become the same.

This replacement of the effective area by the geometrical area is wrong from the point of view of the electromagnetic theory (as discussed above, the effective area of a small antenna is not equal to its geometrical area, and the received power of a lossless antenna loaded by a tunable reactance is not defined by the antenna effective area), but it appears that we get the correct estimation for an RIS that is operating as a perfect anomalous reflector.

We stress that this coincidence is valid only for perfectly operating anomalous reflectors, where parasitic scattering into all possible reflection directions is completely suppressed. Conventional RIS metasurfaces designed as phase-gradient reflectors always suffer from parasitic scattering [53], meaning that this approach will give some overestimation of the received power.

Finally, we note that the RIS EM model (3.11) can be written in an equivalent form in terms of the effective gain of the RIS panel, and defined as

$$G_{\text{tx}} = \frac{4\pi S_1}{\lambda^2} |\cos \theta_r| \quad (3.15)$$

when the RIS acts as a transmitter and

$$G_{\text{rx}} = \frac{4\pi S_1}{\lambda^2} |\cos \theta_i|, \quad (3.16)$$

when it acts as a receiver. Substituting these definitions in Eq. (3.11) we get

$$P_r = \frac{P_t G_t G_r G_{\text{tx}} G_{\text{rx}} \lambda^4}{(4\pi)^4 (d_t d_r)^2} \eta_{\text{eff}}. \quad (3.17)$$

3.2.2 Simulation results

In this section, we perform simulations to compare the numerical differences between the two models. We consider an example of a dipole antenna array with $\lambda/2$ spacing between elements. By using the antenna toolbox in MATLAB, we can create a rectangular dipole array with different sizes and tune each element to resonate at a desired frequency. In the simulations, we create a 3×3 rectangular array with resonating dipole antennas as the unit-cell elements, i.e., 9 dipole antennas in this

3.2. Communication and electromagnetic models for an optimized RIS

array. We vary the frequency from 20 GHz to 40 GHz. Then for each frequency, we can obtain the radiation pattern of this array and thus also find the total gain of this array. We use the maximum gain of the array to approximate the RIS gains G_{tx} and G_{rx} , respectively. This is reasonable because we can orient the array to make its maximum directivity toward the Tx or the Rx antennas to imitate the reflection property of an RIS. In addition, we set $\eta_{\text{eff}} = 1$, $G_t = G_r = 1$, and $d_t = d_r = 5$ m. The RIS is in the far field of both Tx and Rx antennas. Then we calculate the path gain as

$$P_{\text{EM}} = \frac{G_t G_r G_{\text{tx}} G_{\text{rx}} \lambda^4}{(4\pi)^4 (d_t d_r)^2} \eta_{\text{eff}}. \quad (3.18)$$

from the RIS EM model (3.17) and

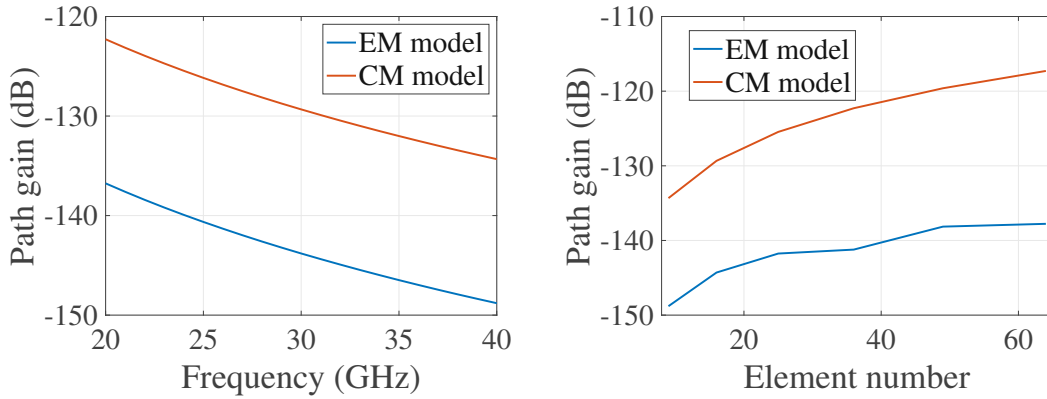
$$P_{\text{CM}} = \frac{G_t G G_r \lambda^2 L^2 A}{64\pi^3 (d_t d_r)^2} \quad (3.19)$$

from the RIS CM model (3.10). Note that in Eq. (3.19) we use $G = 3/2$ and $A = \frac{3\lambda^2}{8\pi}$ for each unit cell. The results are shown in Fig. 3.6(a), which gives the difference between the two models of around 14.47 dB. This difference comes from the $G_{\text{tx}} G_{\text{rx}}$ in Eq. (3.18) and $\frac{9L^2}{4}$ with $L = 9$ in Eq. (3.19) while the remaining terms of the two equations are the same. From the simulation, the maximum gain of the dipole antenna array is almost a constant value of 4.07 dBi over the whole frequency range. It is expected because the gain of a resonant dipole does not depend on the resonance frequency and is a constant value of $3/2$.

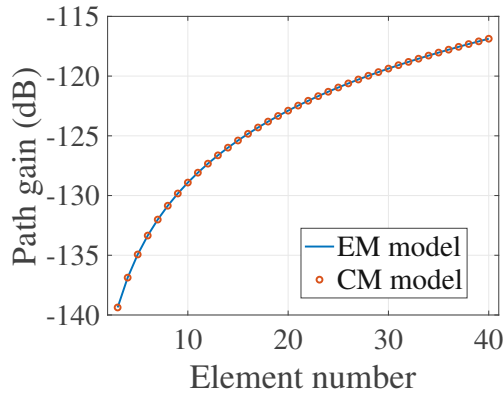
Since the element number L in Eq. (3.19) is another important parameter that causes the difference between the two models, we now vary the L value from 3×3 , 4×4 , ..., 8×8 , and create 6 dipole arrays with these 6 different sizes all resonate at 40 GHz. The path gain results from the two models are shown in Fig. 3.6(b). The differences between the two models are larger as the number of elements increases. We notice that with the RIS CM model, the path gain increases monotonically with the element number L , which is obvious from Eq. (3.19). However, with the RIS EM model, the path gain does not always increase with the element number, because the total gain of an RIS supercell is not proportional to the element number. This is a more general case in reality, otherwise, the antenna gain would be infinitely large when the unit cell number grows to infinity.

On the other hand, the two models become equivalent when the total effective area of the RIS is assumed to be the same for the two models. To simulate such a scenario, We set $LA = S_1 |\cos \theta_r|$, $G = 4\pi A |\cos \theta_i| / \lambda^2$, $\theta_i = 50^\circ$, $\theta_r = 0^\circ$, frequency equals to 40 GHz and $A = \lambda^2/4$. Then we vary L from 3 to 40 and compare the results from both Eqs. (3.10) and (3.11). The results for both models are shown in Fig. 3.6(c), and they are obviously the same. However, we stress that this assumption is not valid in general. To obtain accurate and correct results, the RIS EM model should be used to model the whole RIS instead of multiplying the element number with the effective area and gain of unit cells. Therefore, the RIS EM model is

3.2. Communication and electromagnetic models for an optimized RIS



(a) Path gain vs. frequency between the EM and CM models. (b) Path gain vs. element number between the EM and CM models.



(c) Path gain vs. element number between the EM and CM models in a special case.

Figure 3.6: Simulation results of the path gain from the two models.

implemented as a new path loss model for RIS-assisted links in the Vienna SLS.

In summary, we compared two different path loss models derived from the electromagnetic and communication theory points of view. The RIS EM model is derived by modeling the RIS as a metasurface optimized for anomalous reflection into the desired direction. In the RIS CM model, the path loss is derived by summing up reflections from all array elements with the assumption that all of them function as independent relays. The properties of each element are quantified by their effective areas and gains, which are not applicable to lossless scatterers. Interestingly, however, if one formally substitutes the effective areas of unit cells with the corresponding geometrical areas scaled by cosine factors, the RIS CM model gives the same result as the RIS EM model (but only for perfectly functioning RISs). We considered a simple example of a rectangular array with its elements being resonant dipole antennas, in which case the path gain results show about 14.47 dB difference between the two models. The simulation results validate our analysis and demon-

strate that, in a general case, the RIS CM model can give very wrong results. As an improvement, the RIS EM model has been implemented in the Vienna SLS for RIS-assisted links.

3.3 Final remarks

This chapter first explores the potential enhancement of radio signal propagation in intricate environments through the deployment of basic resonant dipole scatterers. Since the radiation pattern of a dipole is omnidirectional in the azimuthal plane, users at any azimuth angle could be served by the dipole scatterers regardless of their position. We modify the MATLAB ray tracing model based on the bi-static scattering cross-section of a dipolar scatterer and examine the impact of these static scatterers on the power received at the user's location. The simulation results in a scenario in which the direct link is totally blocked are similar to those from an untuned RIS which was explained in Chapter 2. However, our approach with the static scatterers is much more convenient and easy to realize since it does not involve human control and signal processing, and dipoles are very cheap to get.

While the randomly deployed resonant dipoles work similarly to an untuned RIS, in the second part, we discuss two path loss models for a tuned RIS; one is the RIS CM model we explained in Chapter 2, and the other one is the RIS EM model derived from electromagnetic theory. The estimations given by the two models are rather different, but surprisingly, we find that the CM model gives the same result as the EM model for perfectly functioning anomalous reflectors if one replaces the effective areas of the unit cells with their geometrical areas, scaled by the corresponding angular factors. Simulation results validate our analysis and show the numerical differences between the two models when we vary the frequency and the number of elements in RISs. In conclusion, the RIS EM model is more reasonable and accurate in general scenarios, while the RIS CM model is too idealized. However, in a large-scale multicell network scenario, using the RIS EM model for system-level simulations requires the information of incidence and reflection angles of each RIS, which also potentially involves the problem of how to place the RISs in the environment. The RIS CM model can still be used in system-level simulations to roughly estimate the system performance without these concerns. However, the results will be overestimated and can be used as an upper limit.

4

RIS model verification with a perfect anomalous reflector

The RIS models in the literature are mostly based on theoretical analysis and simulations. The best way to verify the RIS models we explained in the previous chapter is to design an RIS from electromagnetic theory and test if our models can work well with such RISs. Therefore, in this chapter, we first introduce the process of designing an RIS. Next, we evaluate the communication performance of our designed RIS through communication models and software.

Electromagnetic design of RIS

There are already some methods for designing high-efficiency periodic metasurfaces [53–57] and metagratings [58–61] in the literature. These approaches are primarily based on the generalized law of reflection [62] or the phased-array principle [63]. It is evident that the scattering power efficiency of these conventional phase-gradient reflectors gradually declines as deflection angles increase [53]. This issue has been addressed by employing a periodic reflector configuration, which allows for manipulating the propagating Floquet modes by optimizing evanescent fields near the reflector [56]. In [54], a periodic reflector is designed using a supercell period comprising two meta-atoms, allowing for independent control over two propagating Floquet modes. In [56], individual Floquet modes are analyzed by controlling the structural periodicity and defining multichannel metasurfaces. However, that design requires multiple component dimensions to achieve an optimized scattering matrix, making it impractical to deploy in a real environment in realizing multiple and reconfigurable reflection angles within a single design. Additionally, optimizing the meta-atoms of the supercell through full-wave EM simulations proves inefficient, demanding substantial computational resources and prolonged optimization times. An arithmetic optimization method has been developed using array antenna scattering synthesis for periodic reflectors comprising reactively loaded patch elements in a supercell [64]. The method transfers the load optimization to the circuit-based algebraic optimization domain, offering a numerically efficient solution compared to

computation-intensive full-wave EM simulations. Yet, this paper confines the reflector design to generate beams into discrete angles aligned with a single supported Floquet harmonic, restraining its scalability for practical deflectors suitable for use as RISs.

Therefore, in this chapter, we adopt the scattering synthesis methodology in [64] to design a multimode periodic anomalous reflector. Our design goal is to use a fixed dimension and structure to achieve multiple anomalous scattering directions and simultaneously suppress specular reflections when a plane wave illuminates the anomalous reflector. We achieve this goal by applying the Floquet theory to an electrically large supercell of a periodic array. By optimizing the reactive loads of the elements in this supercell, we can maximize the scattering efficiency for each desired scattering mode while suppressing the scattering at other propagation modes.

Communication modeling and simulation of RIS

The next step is to pass the EM properties of the designed RIS to our communication system and evaluate the performance of the RIS-assisted links. To simulate and analyze large-scale wireless networks in realistic scenarios, simulation platforms such as ray tracing and system-level simulators serve as practical tools. There have been studies on RIS functionality in ray tracing tools, for instance, the authors in [65] introduce a macroscopic model for evaluating the multimode re-radiation and diffuse scattering from an RIS. That model can be integrated with ray-based models such as ray tracing and ray launching for realistic radio propagation simulations. In addition, the authors in [66] extend the model to include metasurface scattering at the beginning or at the end of the interaction chain and perform ray tracing simulations in an indoor scenario for a lossy, phase-gradient AR. In [40, 47], the authors demonstrate the scaling law governing the power reflected from an RIS is influenced by various factors, such as the RIS size and the mutual distances between the RIS and the Tx/Rx with measurements. The authors of [67] give an overview of RIS-based channel measurements and experiments, large-scale path loss models, and small-scale multipath fading channel models, as well as channel characterization issues of RIS-assisted wireless communication systems. In [28], the authors evaluate the system performance of an RIS-assisted cellular network through system-level simulations, such as the outdoor and indoor coverage and ergodic rate with different-sized RISs and under different frequency bands.

Gaps and issues

Even though a broad range of RIS-related research activities have been done in recent years, there is still a lack of a systematic study of RIS from the EM design to communication models. The above-mentioned models are based on the notion of the local reflection coefficient from different points of the RIS panels, but this field model is not necessarily efficient or even electromagnetically consistent, and in practice, it is not possible to independently control the response of each individual

4.1. Anomalous reflector design

array element. In addition, there are no works on analyzing an RIS in a ray tracer or in a system-level simulator. It is necessary to study if and how such optimal and scanning anomalous reflectors can be practically realized, and it is essential to build connections between the theory and practice, as well as between the EM design part and the communication analysis part.

We aim to fill the gap by proposing a methodology to combine outputs from electromagnetic RIS design into an RIS-tailored SLS and a ray tracer to systematically study the communication link performance of our designed RIS. More specifically, we propose two theoretical methods to calculate the large-scale fading through the RIS. One is to utilize the simulated receiving and transmitting gain of the designed RIS to build an electromagnetically consistent path loss model for an RIS. The other one is to use the path loss model for a perfectly working RIS that has been explained in Chapter 3. In addition, we implement the designed RIS model into the MATLAB ray tracer and compare the simulation results with theoretical results. After verifying the connections between electromagnetic and communication aspects through simulations and theory, the proposed communication model can be used for a broad range of RIS designs to perform large-scale system-level and ray-tracing simulations in realistic scenarios. The work described in this chapter is submitted to the publications [23, 24].

4.1 Anomalous reflector design

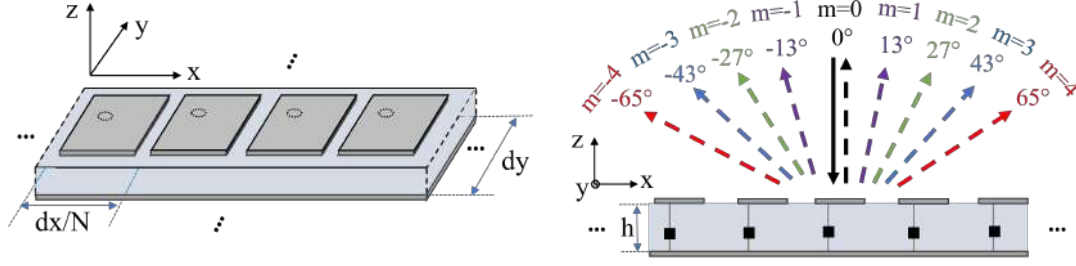
To design an AR that is capable of reflecting incident waves in multiple directions with high efficiency, we use the scattering synthesis approach proposed in [64]. According to the Floquet-Bloch theory [68], when a plane wave is illuminating an infinite periodic metasurface at the incident angle θ_i , the reflected field is a superposition of plane waves propagating in different directions θ_{rm} according to the following relation, e.g. [69]:

$$\sin \theta_{rm} = \sin \theta_i + \frac{2\pi m}{kd}, \quad (4.1)$$

where $m = 0, \pm 1, \pm 2, \dots$ is the index of propagating harmonics, and d is the period of the metasurface. The wave number is defined as $k = 2\pi/\lambda$. To design a metasurface structure, we have to define the center frequency, the periodicity d , the number of propagation harmonics, and the incident and reflection angles. For our design, we choose a TE-polarized periodic structure working at the center frequency of 26 GHz. We want to observe multiple reflection directions obviously and these directions are separate enough, therefore, we choose the incident angle of the AR as $\theta_i = 0^\circ$ and the highest propagating harmonic as $m = 4$. The maximum reflection angle as $\theta_{rm} = 65^\circ$ corresponds to $m = 4$. Substituting to (4.1) we obtain

$$\sin 65^\circ = \sin 0^\circ + 4\lambda/d, \quad (4.2)$$

4.1. Anomalous reflector design



(a) Illustration of the metasurface structure with N elements. (b) Illustration of the incidence wave and reflection waves at different propagating harmonics.

Figure 4.1: The structure and propagation modes of the designed anomalous reflector.

Table 4.1: Dimensions of the supercell array

Parameters	Values
supercell dimension ($d_x \times d_y$)	$4.4135\lambda \times 0.2758\lambda$ (50.89 mm \times 3.1806 mm)
unit cell dimension ($d_x/16 \times d_y$)	$0.2758\lambda \times 0.2758\lambda$ (3.1806 mm \times 3.1806 mm)
squared patch dimension	$0.2328\lambda \times 0.2328\lambda$ (2.6838 mm \times 2.6838 mm)
substrate height (h)	0.338 mm
probe feed position (x_p, y_p)	(0, 1.068) mm

which results in $d = 4.4135\lambda$ as the supercell length of our designed AR. This structure also allows for propagation harmonics at $\pm 43^\circ$ when $m = \pm 3$, $\pm 27^\circ$ when $m = \pm 2$, and $\pm 13^\circ$ when $m = \pm 1$, and 0° when $m = 0$, respectively, and all the other modes are evanescent. Figure 4.1(a) gives an illustration of our designed AR structure and Fig. 4.1(b) shows the corresponding propagation modes. According to [64], nearly perfect anomalous reflection could be achieved with less than two loaded scatterers per half wavelength. Then we choose $N = 16$ as the number of unit cells in the supercell as it can achieve nearly perfect reflections for our designed propagation modes, which results in a unit cell dimension of $d/16 = 0.2758\lambda$.

After defining the dimension and desired reflection angles, we start by designing a single unit cell with the dimension of $dx/N \times dy = 0.2758\lambda \times 0.2758\lambda$ in the xy -plane in the CST Microwave Studio. The unit cell is a squared patch antenna resonating at 26 GHz with a 50Ω matching impedance. The material of the squared patch and the ground plane is set as perfect electric conductor (PEC). The substrate material is lossless Rogers RO4350B with a relative permittivity $\epsilon_r = 3.66$. The patch dimensions and the feeding position are presented in Table 4.1. Next, we duplicate this unit cell along the x direction to form a supercell with the dimension of $dx \times dy = 4.4135\lambda \times 0.2758\lambda$, i.e., 16 unit cells in the x -direction. The incidence and scattering waves are in the xz -plane.

Our goal is to let the RIS fully reflect the incident wave from $\theta_i = 0^\circ$ in each of the four angles $\theta_r = 13^\circ, 27^\circ, 43^\circ$, and 65° without reflection waves in other than the main desired directions. We achieve this goal by replacing the unit cell feeds

4.1. Anomalous reflector design

Table 4.2: Reflection efficiency with optimized and quantized loads.

resolution	mode 1 (13°)	mode 2 (27°)	mode 3 (43°)	mode 4 (65°)
continuous	99.6%	99.3%	99.5%	99.1%
4 bit	99.4%	99%	95.6%	98.4%
3 bit	97%	98.1%	95.2%	87%
2 bit	93.1%	92.3%	91.6%	83.7%
1 bit	51.1%	47.1%	41.2%	36%

Table 4.3: Summary of the optimized and quantized load reactances.

Mode	Bit	Optimized load reactances (Ω)
1	Cont	34, 20, 22, 75, 57, 88, 298, 162, -288, -153, -114, 18, -64, -2, 3, -17
	4 bit	-5, 113, -5, 215, 29, 1791, 68, -300, -83, -83, -57, -15, -27, -5, 5, 29
	3 bit	-134, 45, -57, -27, 16, -5, -5, 45, 45, -27, 1791, -57, 1791, 113, -134, -134
	2 bit	1791, -57, 1791, 1791, -57, -57, -57, -57, 45, -57, 45, -5, -5, 45, 45, -5
	1 bit	45, -57, -57, -57, -57, -57, -57, 45, -57, 45, 45, 45, 45, 45, 45, 45
2	Cont	-1, -364, -66, -18, -44, 108, -28, 323, -2, -359, -77, -12, -44, 107, -27, 319
	4 bit	29, 5, 215, 16, -300, 5, -57, -5, 45, -5, 215, 16, -300, -15, -57, 5
	3 bit	113, -5, 1791, -27, -134, -27, 16, -27, 113, -5, 1791, -57, -134, -27, 16, -27
	2 bit	-57, -5, -5, 45, 45, 45, 1791, -57, -57, -5, -5, 45, 45, 45, 1791, -57
	1 bit	45, -57, -57, -57, 45, -57, 45, 45, 45, -57, -57, -57, -57, 45, 45, 45
3	Cont	-57, 365, -15, -215, 263, -51, 85, 143, -905, -111, 140, -43, 712, -65, -134, 221
	4 bit	68, -300, 16, 5, 16, 215, 215, -134, 29, 29, 45, 1791, -83, -5, -15, 113
	3 bit	45, -5, 1791, -134, -57, 16, 45, 113, 1791, -57, -27, 45, 45, 1791, -134, -27
	2 bit	-57, -5, 45, 45, 1791, -57, -57, 45, -5, 1791, -57, -57, -5, 45, 45, 1791
	1 bit	-57, 45, 45, -57, -57, -57, 45, 45, 45, -57, -57, 45, 45, 45, -57, -57
4	Cont	255, -210, 31, 22, 255, -212, 31, 22, 252, -212, 32, 23, 253, -212, 33, 22
	4 bit	-300, 16, 29, 215, -300, 16, 29, 215, -300, 29, 29, 215, -300, 29, 29, 215
	3 bit	-134, 45, 45, 1791, -134, 45, 45, 1791, -134, 45, 45, 1791, -134, 45, 45, 1791
	2 bit	1791, -57, 45, 45, 1791, -57, 45, 45, 1791, -57, 45, 45, 1791, -57, 45, 45
	1 bit	45, -57, -57, 45, 45, -57, -57, 45, 45, -57, -57, 45, 45, -57, -57, 45

with reactive loads and optimizing the load impedance of each unit cell following the optimization method in [64]. The objective function of our optimization problem is to maximize the power reflection efficiency at each of the four propagation modes. Reflection efficiency is defined as the ratio of the radiated power to the input power of the antenna, the value is between zero and one and is usually quoted in terms of a percentage [70]. At the beginning, we assume the RIS has continuous phases, which corresponds to a set of continuous load impedances. Therefore, the values of the load impedance have no restriction, they can be extremely large or small. For example, we set a range of [-1000 1000]; the impedance of each unit cell can be any random integer within this range. Then we use the genetic algorithm to achieve a maximized reflection efficiency of the supercell for each mode. The achieved reflection efficiency for each propagation mode after the load impedance optimization

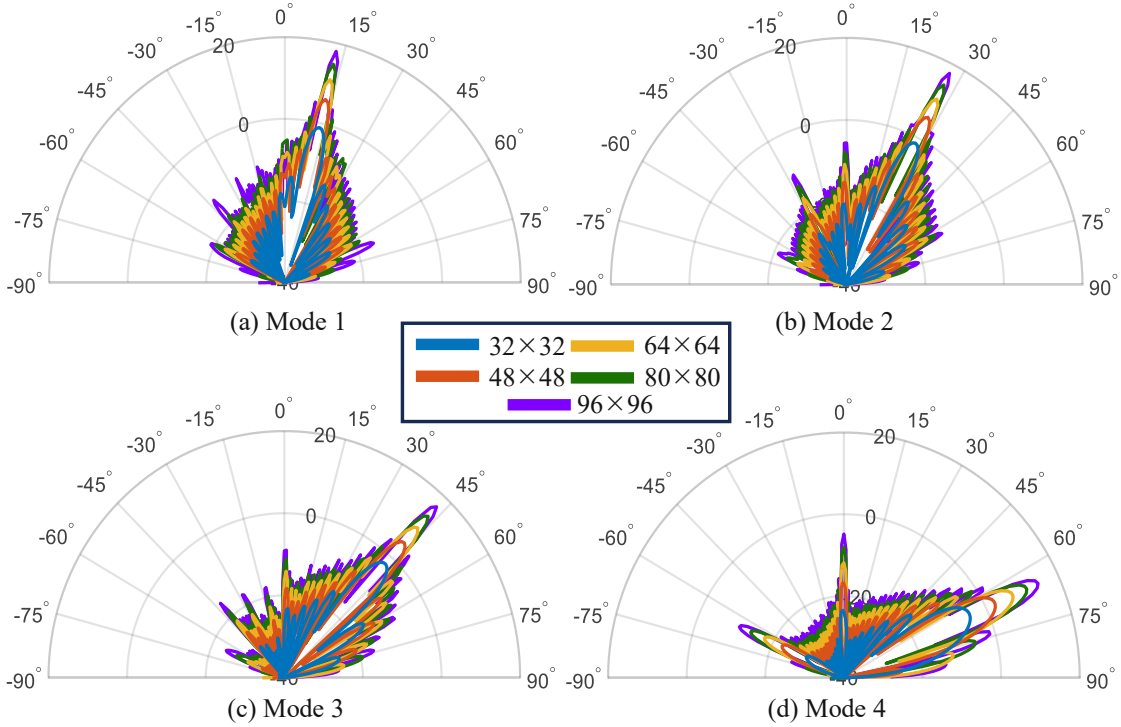


Figure 4.2: Simulated far-field radiation pattern of the five different sized arrays employing optimized continuous loads for propagating harmonics from 1 to 4, reported in dB(V/m) scale.

is listed in Table 4.2 marked as “continuous”, which shows nearly perfect reflections for each mode. The optimized load reactance values for the RIS unit cells for the four different propagation modes are listed in Table 4.3. The positive value means the load is inductive, and the negative value means the impedance is capacitive. The quantized values marked as “4 bit”, ..., “1 bit” in Table 4.2 and Table 4.3 are explained in Sec. 4.3.

The initial simulation is performed for an infinite array of supercells under periodic boundary conditions. Next, we crop the initial infinite supercell structure into five finite sizes using the array factor approximation function in CST and obtain the radiation properties of those finite arrays. The number of unit cells in the five finite arrays is 32×32 , 48×48 , 64×64 , 80×80 , and 96×96 , corresponding to a total number of 1024, 2304, 4096, 6400, and 9216 individual scatterers, respectively. Note that our designed supercell dimension is 16×1 unit cells in $x \times y$ directions, so we choose the finite array dimension as an integer times 16. For example, 32×32 -sized array corresponds to 16×2 in the x -direction and 1×32 in the y -direction; 48×48 -sized array is a repeating of 16×3 in the x -direction and 1×48 in the y -direction. The results of far-zone E -fields of the five finite-size arrays are plotted in Fig. 4.2, which shows a dominant scattering beam into the desired direction while

eliminating the side lobes in all other directions. It also shows that a larger size of the array results in a stronger radiation beam in the desired direction and the beam gets narrower.

4.2 Theoretical analysis of the large-scale fading

In this section, we consider and compare two theoretical models of large-scale fading in RIS-assisted links. At this stage, we assume a far-field propagation scenario with a single LOS-path communication link. One of the studied methods is based on a theoretical estimation of the response of perfectly functioning RISs [49], incorporated in the Vienna SLS, and the other one is based on numerically simulated RIS directivity patterns. Since our designed AR can reflect waves in four different directions by reconfiguring the load impedance of each unit cell, in the following text, we name it RIS for convenience.

First of all, we analyze the large-scale fading of the designed RIS from Sec. 4.1 using the path loss model (3.11) as explained in Chapter 3 since this model is used for a perfectly working RIS, and we denote it as method 1. The received power at the Rx antenna from method 1 is calculated as

$$P_1 = P_t G_t G_r \eta_{\text{eff}} \left(\frac{S_1}{4\pi d_t d_r} \right)^2 |\cos \theta_i \cos \theta_r|. \quad (4.3)$$

According to the design parameters, we set the RIS areas as $S_1 = 32 \times 32 A$, $48 \times 48 A$, $64 \times 64 A$, $80 \times 80 A$, and $96 \times 96 A$ where $A = (0.2758\lambda)^2$ is the area of one unit cell. Other parameters are set as $\eta_{\text{eff}} = 1$ assuming perfect reflection without system loss, $G_t = G_r = 1$ assuming the Tx and Rx antennas are both omnidirectional antennas. The far-field distances of the five RIS sizes are 1.80, 4.04, 7.19, 11.23, and 16.17 m for the sizes of $32 \times 32 A$, $48 \times 48 A$, $64 \times 64 A$, $80 \times 80 A$, and $96 \times 96 A$, respectively, according to the calculation $R = 2D_i^2/\lambda$ with D_i the largest dimension of the antenna. Therefore, we set $d_t = 17$ m and $d_r = 17.22$ m to fulfil the far-field condition. The incidence and reflection angles are $\theta_i = 0^\circ$ and $\theta_r = 13^\circ, 27^\circ, 43^\circ, 65^\circ$ for propagation modes 1 to 4, respectively.

For periodic metasurfaces, the distribution of reflected fields over all angles can be estimated based on the results of Section II in [49], also for imperfect RISs that produce some parasitic scattering into undesired Floquet modes. Propagation of signals due to reflections in some objects is conventionally modeled in terms of the bi-static scattering cross-section that can be determined based on the analytical model in [49]. For reflections into the desired direction, that model gives a very simple analytical formula. While using the theory of [49] it is possible to estimate the bi-static cross section for any reflection direction, for integration of the RIS models into ray-tracing simulators it is more convenient to use the model for the scattering performance of RIS in terms of the RIS panel gains in the directions of illumination and observation. Therefore, we use Equation (3.17) as a second

4.2. Theoretical analysis of the large-scale fading

method to evaluate the large-scale fading of the designed RIS. This theoretical model combines analytical estimations of the propagation loss with the radiation pattern results from EM simulations. The received power from method 2 is written as

$$P_2 = \frac{P_t G_t G_r G_{\text{tx}} G_{\text{rx}} \lambda^4}{(4\pi)^4 (d_t d_r)^2} \eta_{\text{eff}}. \quad (4.4)$$

In this equation, we set the same values for G_t , G_r , d_t , d_r and η_{eff} as in the method 1. The parameter G_{rx} is the gain of the RIS in the direction from RIS to Tx, and G_{tx} is the gain in the direction from RIS to Rx. Note that Eq. (4.4) is the same as Eq. (6) in [71], but here we use it for the whole RIS panel, and not for a single array element, as in [71]. The product of the two gains of the RIS panel is related to its bi-static scattering cross-section σ as

$$G_{\text{rx}} G_{\text{tx}} = \frac{4\pi\sigma}{\lambda^2}, \quad (4.5)$$

which is a function of both angles of incidence and observation. This equation establishes the relation between the results given by the two used methods.

The two RIS gains are obtained from the CST simulation of the RIS, i.e., we obtain the electric field far-field pattern $F(\theta, \phi)$ of the RIS from CST simulations, then we calculate the directivity of the RIS according to [39]:

$$D(\theta, \phi) = \frac{4\pi F(\theta, \phi)}{\int_0^{2\pi} \int_0^\pi F(\theta, \phi) \sin \theta d\theta d\phi}. \quad (4.6)$$

The RIS gain is calculated as

$$G(\theta, \phi) = e_{\text{cd}} D(\theta, \phi), \quad (4.7)$$

where e_{cd} is the panel efficiency. If the RIS losses can be neglected, we have $e_{\text{cd}} = 1$.

The RIS gain values for four different modes, each with five different sizes loaded by optimized continuous load impedance, are listed in Table 4.4. It is worth noting that each RIS model needs both the gain values of G_{rx} and G_{tx} . Corresponding to our RIS designed for the normal incident angle and four reflection angles, G_{rx} is obtained at 0° , and G_{tx} is obtained at 13° , 27° , 43° , and 65° .

The received power results obtained from the two methods are shown in Fig. 4.3, where we can observe that for all four modes, the two methods give very close results. The differences between the two methods are about 0.2 dB to 0.6 dB for mode 1, mode 2, and mode 3 when the RIS sizes change from $32 \times 32 A$ to $96 \times 96 A$. For mode 4 the difference is from 0.7 dB to 0.8 dB with the five sizes.

This agreement is expected because Eq. (4.3) is valid for a theoretically perfect RISs, and from Sec. 4.1 we saw that the RIS design with continuous loads gives a nearly perfect performance. In fact, it can be shown that for ideal RISs with continuous current distribution, the considered two path loss models are equivalent.

4.2. Theoretical analysis of the large-scale fading

Table 4.4: Different-size RIS gains (in dB) with continuous and quantized loads

Mode	Bit	$32 \times 32 A$		$48 \times 48 A$		$64 \times 64 A$		$80 \times 80 A$		$96 \times 96 A$	
		G_{tx}	G_{rx}	G_{tx}	G_{rx}	G_{tx}	G_{rx}	G_{tx}	G_{rx}	G_{tx}	G_{rx}
1	Cont	29.86	30.04	33.36	33.61	35.84	36.19	37.76	38.27	39.33	40.04
	4 bit	29.86	30.03	33.35	33.61	35.84	36.19	37.76	38.26	39.32	40.03
	3 bit	29.78	29.95	33.28	33.52	35.76	36.10	37.68	38.18	39.26	39.95
	2 bit	29.57	29.73	33.06	33.30	35.54	35.88	37.47	37.95	39.04	39.70
	1 bit	27.20	27.28	30.69	30.81	33.17	33.34	35.10	35.35	36.68	37.02
2	Cont	29.49	30.04	32.99	33.61	35.47	36.19	37.39	38.27	38.97	40.04
	4 bit	29.45	30.01	32.95	33.58	35.43	36.16	37.36	38.23	38.93	40.00
	3 bit	29.45	29.99	32.94	33.56	35.42	36.14	37.35	38.22	38.93	39.98
	2 bit	29.23	29.76	32.71	33.33	35.20	35.90	37.12	37.97	38.70	39.72
	1 bit	26.46	27.03	29.94	30.53	32.42	33.04	34.35	35.02	35.94	36.68
3	Cont	28.69	30.03	32.16	33.61	34.63	36.19	36.54	38.26	38.09	40.03
	4 bit	28.51	29.87	31.99	33.44	34.45	36.01	36.36	38.09	37.92	39.84
	3 bit	28.51	29.86	31.98	33.43	34.45	36.01	36.36	38.08	37.93	39.84
	2 bit	28.37	29.68	31.82	33.24	34.28	35.81	36.19	37.87	37.74	39.62
	1 bit	24.97	26.37	28.46	29.88	30.94	32.39	32.87	34.38	34.44	36.03
4	Cont	26.72	30.04	30.07	33.61	32.47	36.19	34.35	38.27	35.90	40.04
	4 bit	26.65	30.00	30.01	33.57	32.41	36.15	34.29	38.22	35.84	39.98
	3 bit	26.16	29.56	29.52	33.11	31.93	35.67	33.81	37.72	35.36	39.46
	2 bit	25.97	29.36	29.32	32.90	31.73	35.45	33.61	37.50	35.17	39.22
	1 bit	22.31	25.89	25.70	29.34	28.13	31.81	30.06	33.77	31.65	35.40

The model of (4.3) assumes that the RIS captures all the power that is incident on its surface and retransmits it without imperfections. This means that if we consider the same RIS as a conjugate-matched receiving antenna, its effective area A_{eff} is equal to the geometrical area of the panel cross-section, that is, $A_{\text{eff}} = S_1 |\cos \theta_i|$. Likewise, in the transmit regime, we have $A_{\text{eff}} = S_1 |\cos \theta_r|$. Using the general relation between the effective area and gain, valid for any linear and reciprocal antenna, $G = 4\pi A_{\text{eff}}/\lambda^2$, We can find the RIS gains for an ideal RIS in terms of the panel area and the incidence and reflection angles are the same as (3.15) and (3.16). Substituting Eq. (3.15) and (3.16) into (4.4) we obtain the same equation as (4.3). Therefore, method 1 and method 2 for our designed RIS are equivalent since they operate perfectly. The small differences between the two methods are from the RIS gain differences between the CST simulation and the ideal theoretical values given by Eqs. (3.15) and (3.16), and they result from the spatial discretization of the reflecting surface.

From [18] we conclude that when the RIS size is doubled, the received power should achieve 6 dB gain for a tuned RIS. In these four figures, the received power has about 7 dB, 5 dB, 4 dB and 3 dB differences for the RIS sizes $32 \times 32 A$ to $48 \times 48 A$, from $48 \times 48 A$ to $64 \times 64 A$, from $64 \times 64 A$ to $80 \times 80 A$, and from $80 \times 80 A$ to $96 \times 96 A$, respectively. Since the RIS size $64 \times 64 A$ is four times

4.3. Load quantization analysis

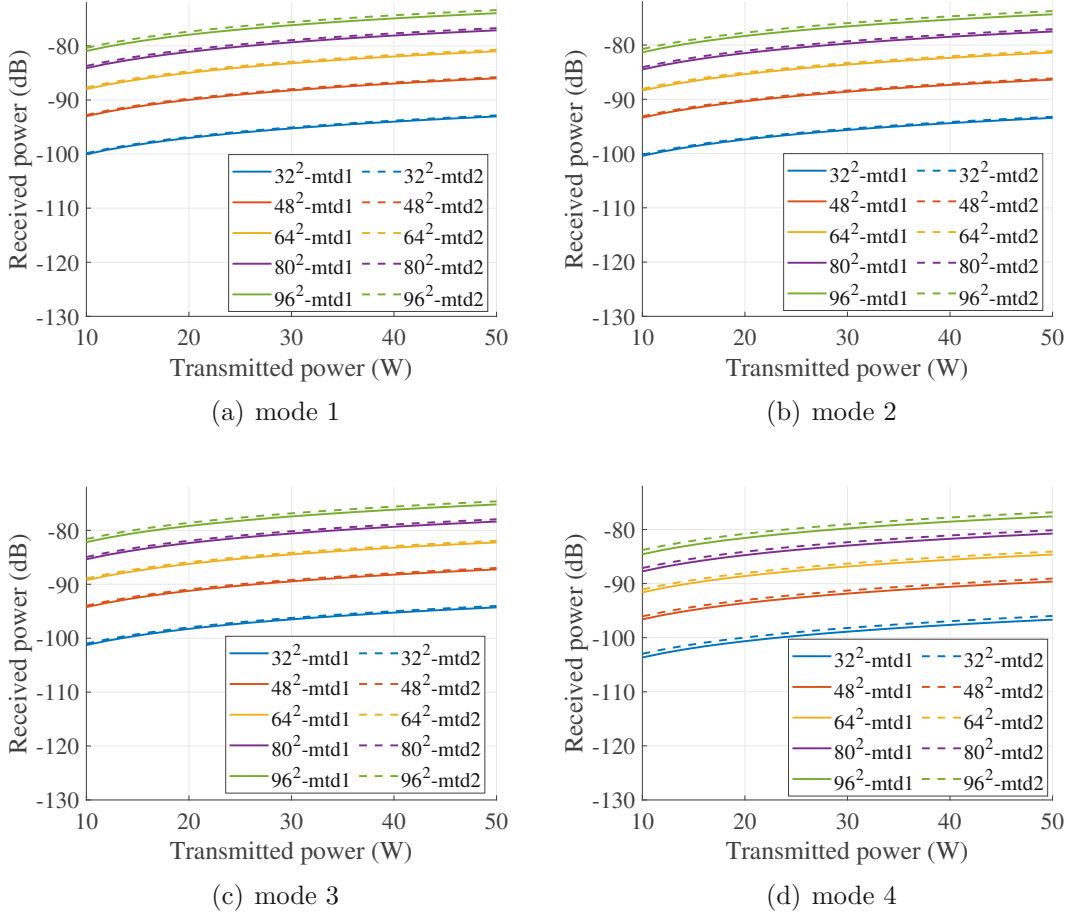


Figure 4.3: Results comparison between the two methods with different RIS sizes.

larger than the size 32×32 A , the received power with 64×64 A size is 12 dB higher than for the 32×32 A -sized RIS. Similarly, the difference between 48×48 A and 96×96 A -sized RIS is also 12 dB, which is consistent with the power scaling law [30].

4.3 Load quantization analysis

The RIS gain values used in Sec. 4.2 are from the optimization of continuous reactive loads, corresponding to the assumption that the controllable loads can have arbitrary reactive impedances and the RIS can have continuous phase shifts. However, in reality, the RIS cannot achieve continuous phase shifts. To analyze a more realistic case, we use quantized RIS phase shifts. For 4-bit quantization resolution, the RIS can achieve $2^4 = 16$ discrete phases. We want the phase to change a total of 360° within the supercell. For the 16 unit cells, the phase gradient between adjacent cells is therefore $360^\circ/16 = 22.5^\circ$. Based on the traditional phase-gradient method [63],

4.3. Load quantization analysis

we can obtain 16 impedance values corresponding to the 16 phases as an initial set. That means, we first run CST simulations with a single unit cell with parametric load variation. Then, we record the phase of the reflection coefficient as a function of the load reactance and make a mapping such that we map the desired set of linearly changing reflection phases into a set of load impedances. The same procedures are done for 1 to 3 bit resolutions. The obtained discrete RIS phases for 1 to 4 bit resolutions, as well as the corresponding impedance values, are summarized in Table 4.5.

Next, we use the genetic algorithm again to optimize the impedance values for the 16 unit cells. Differently from the continuous load optimization, here we have to restrict the impedance values to the 16, 8, 4, and 2 discrete values for 4, 3, 2, 1-bit resolutions, respectively. The reflection efficiency of the RIS with optimized quantized load reactance values for the four different modes are listed in Table 4.2, and the optimized load values of the RIS unit cells are listed in Table 4.3. We can observe that the efficiency is reduced for all the propagating Floquet modes when the quantization resolution decreases from 4-bit to 1-bit. Specifically, the 1-bit quantization leads to very poor efficiency due to the very limited two discrete load values. Generally, the reflection efficiencies for mode 1 ~ 3 are all above 90% with 2 ~ 4 bit resolutions. However, the efficiency of mode 4 with 2 ~ 3 bit resolutions is less than 90%, which is worse than the other three Floquet modes. With a larger θ_r , the quantization effect becomes slightly higher.

To further investigate the influence of the quantized RIS phase shifts or the

Table 4.5: Quantized RIS phases and corresponding load reactances

RIS Phase	Discrete Load Reactance (Ω)			
	4 bit	3 bit	2 bit	1 bit
180°	45	45	45	45
202.5°	29			
225°	16	16		
247.5°	5			
270°	-5	-5	-5	
292.5°	-15			
315°	-27	-27		
337.5°	-39			
0°	-57	-57	-57	-57
22.5°	-83			
45°	-134	-134		
67.5°	-300			
90°	1791	1791	1791	
112.5°	215			
135°	113	113		
157.5°	68			

4.3. Load quantization analysis

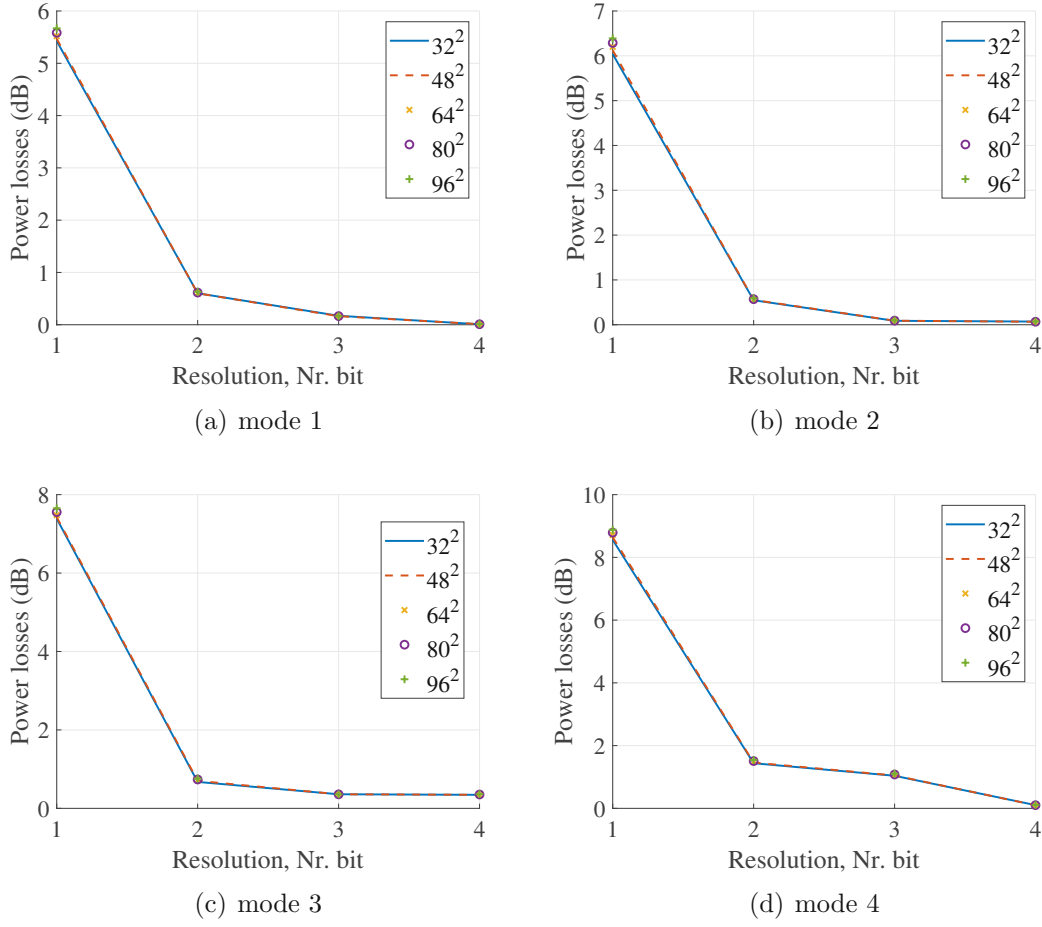


Figure 4.4: Power losses due to load quantization.

load impedance, we calculate the RIS gains in the same way as in Sec. 4.2 but use the CST simulation results obtained from quantized load impedances, which are summarized in Table 4.4. Here we observe that with an increased quantization resolution from 1-bit to 4-bit, the RIS gain values in the desired directions become higher and gradually get close to the gain when using continuous loads. This is because the unit cell loads optimization results become more efficient when we have more load impedance values (2 values for 1-bit and 16 values for 4-bit). That is, the reflection wave is more concentrated in the desired directions, and the side lobes are better suppressed. For example, with 1-bit resolution, we are unable to optimize the unit cell loads to make the reflection waves focus nearly 100 percent on the desired direction because we only have two different load values, which correspond to two RIS phases. That results in strong side lobes in other directions, and thus the reflection wave in the desired direction gets weaker. Consequently, the RIS gain in the desired direction is also quite low. However, with a higher quantization resolution with more discrete load values, the optimization results get better.

In Fig. 4.4 we compare the received powers between the designs based on con-

4.4. Ray tracing simulations

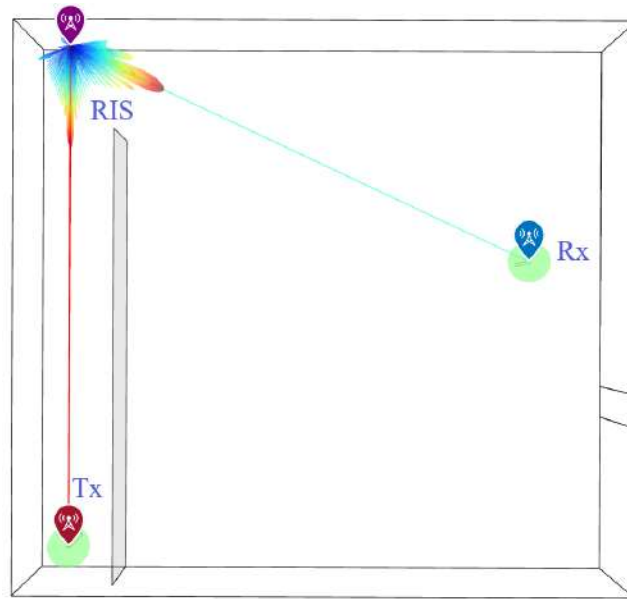


Figure 4.5: A SISO scenario with RIS in the MATLAB ray tracer.

tinuous and quantized load values. Figures 4.4(a), 4.4(b), 4.4(c), and 4.4(d) show the results for modes 1, 2, 3, 4, respectively. The differences between the panels of 5 different sizes are almost the same for all four modes. As expected, when the resolution increases from 1-bit to 4-bit, the differences between the continuous loads designs and the discrete loads become smaller for all four modes. It can be observed that for 1-bit resolution, the scattering losses are quite high for all four modes, while the 4-bit resolution leads to very similar results as for the continuous loads. The 3-bit resolution gives already relatively good results, i.e., 1.11 dB for mode 4, and less than 0.4 dB loss for modes 3, 2, and 1 are good enough.

4.4 Ray tracing simulations

The results in Sec. 4.2 are based on the free-space path loss model, with only one LOS path between the Tx and RIS, and one LOS path between the RIS and Rx. To analyze wave propagation in more realistic environments, ray tracing is a very useful method since it accounts for the effect of the environment. There are several ray tracers already in academic and industrial use, such as the MATLAB ray tracer, the Wireless InSite from Remcom [72], the CloudRT from Beijing Jiaotong University [73], and more. However, there are still no ray tracers that would include an accurately modeled RIS module. To simulate an RIS-assisted scenario, we have to first model an RIS into the ray tracer. In this section, we first incorporate a model of the designed RIS in the MATLAB ray tracer and verify the simulated results against the theory. After that, we extend the simulation scenario from a simple SISO case to a multipath scenario and analyze the simulation results.

4.4. Ray tracing simulations

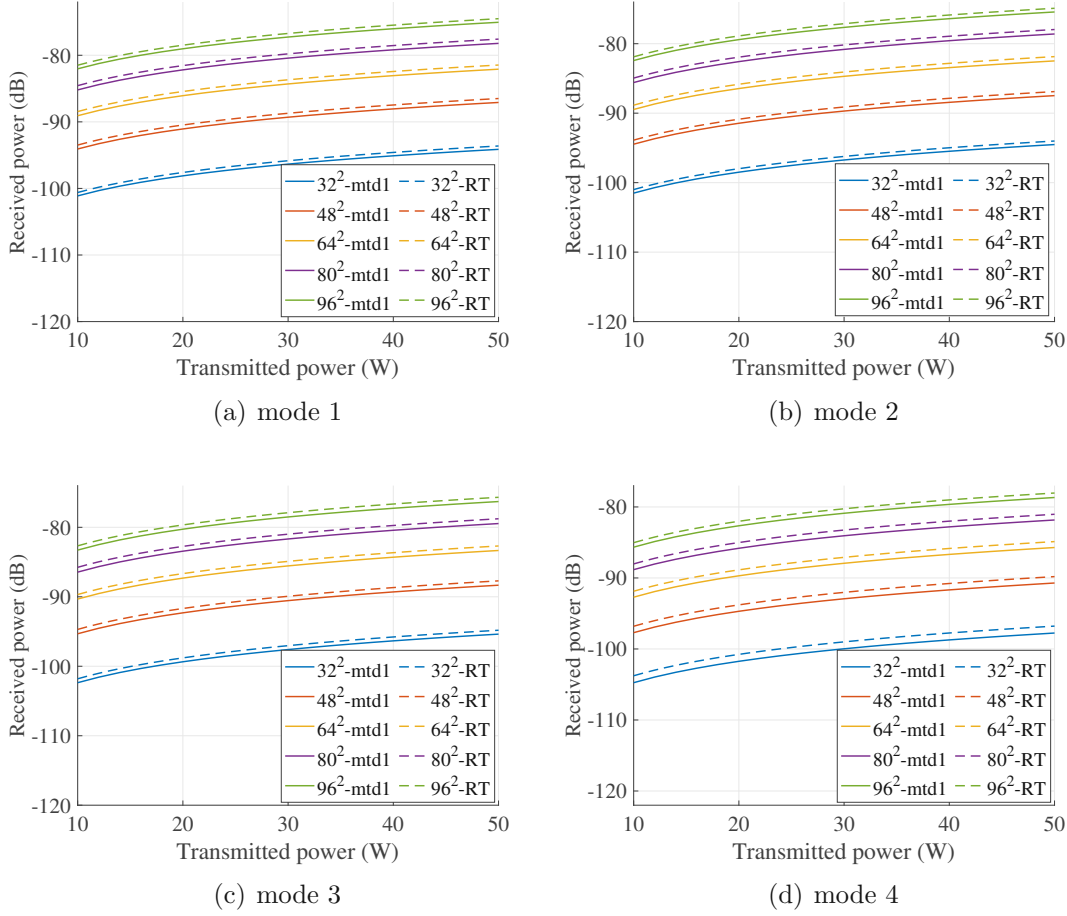


Figure 4.6: Results comparison between method 1 and the RT with different RIS sizes.

4.4.1 Verification in a SISO scenario

We utilize the MATLAB ray tracer to accommodate RIS functionality by modeling the RIS as two separate antennas with imported E-field data from CST. For each RIS size at each propagation mode, we have two RIS patterns, one towards the incident direction and the other towards the realized reflection angle. Therefore, in the ray tracer, we first simulate the Tx-RIS link where the RIS is used as a receiver. Next, we simulate the RIS-Rx link where the RIS is used as a transmitter.

To verify the RIS modeling in the ray tracer, we set up the same SISO scenario in the ray tracer as in Sec. 4.2, see Fig. 4.5. The center frequency is 26 GHz. The Tx and Rx antennas are initially omnidirectional (0 dB gain). The distance between the Tx and RIS is 17 m, and the distance between the RIS and Rx is 17.22 m. When the RIS is used as a receiver for the Tx-RIS link, the RIS pattern is toward 0° , facing the Tx antenna. When the RIS is used as a transmitter for the RIS-Rx link, the reflection pattern of the RIS is towards 13° , 27° , 43° , and 65° for modes 1, 2, 3, 4,

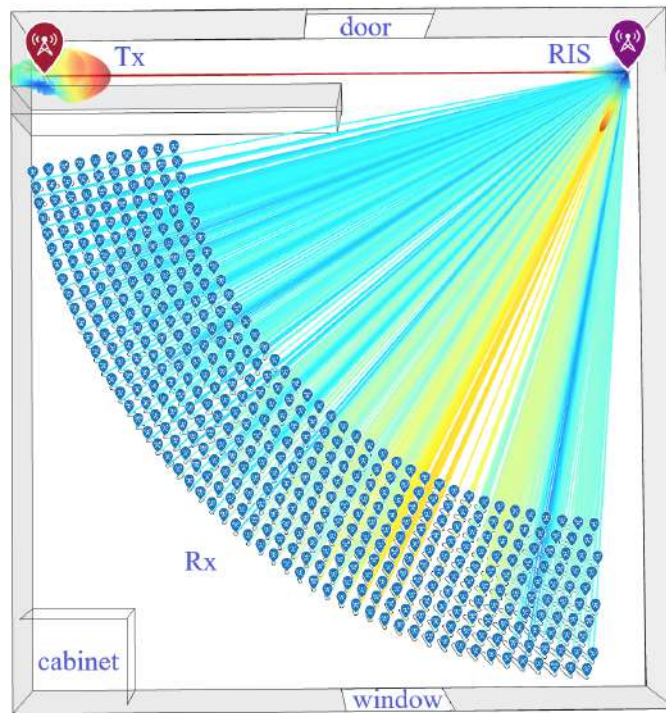


Figure 4.7: An indoor multi-user scenario with RIS in the MATLAB ray tracer.

respectively. The Tx and Rx direct link is blocked by a wall so that there is no LOS path between them. First, the reflection path number is set as 0, so that we only observe the LOS paths between Tx-RIS and RIS-Rx. All walls, ceilings, and floors in this scenario are considered perfect absorbers to provide a direct point of comparison with the LOS path loss models considered above.

The comparison results between the ray tracing simulation and method 1 from Sec. 4.2 are plotted in Fig. 4.6. Figures 4.6(a), 4.6(b), 4.6(c), and 4.6(d) show results for modes 1, 2, 3, 4, respectively. From the four figures we can observe that the ray tracing simulation results are very close to the theoretical results that we have obtained from method 1. The larger the RIS size, the larger the differences between the two results for all four modes. However, even the largest difference that appears for mode 4 is about 0.6 dB. The comparison results indicate that our strategy of modeling RIS in the ray tracer seems correct for the LOS link.

4.4.2 Multi-user scenario with only LOS paths

In this section, we extend the simulation to a multi-user scenario, as shown in Fig. 4.7. The room size is $24 \times 25 \times 3$ (m^3) in terms of width \times length \times height. There is one 1×1 m^2 window on the southern wall, and a 1.3×2.5 m^2 door on the northern wall. In the southwest corner of the room, there is a small cabinet with a height of 2 m. The material of the whole indoor room is set as “concrete” since the MATLAB ray tracer up to version 2024a does not support multiple materials for an imported 3D object. The direct link between the Tx and Rx antennas is

4.4. Ray tracing simulations

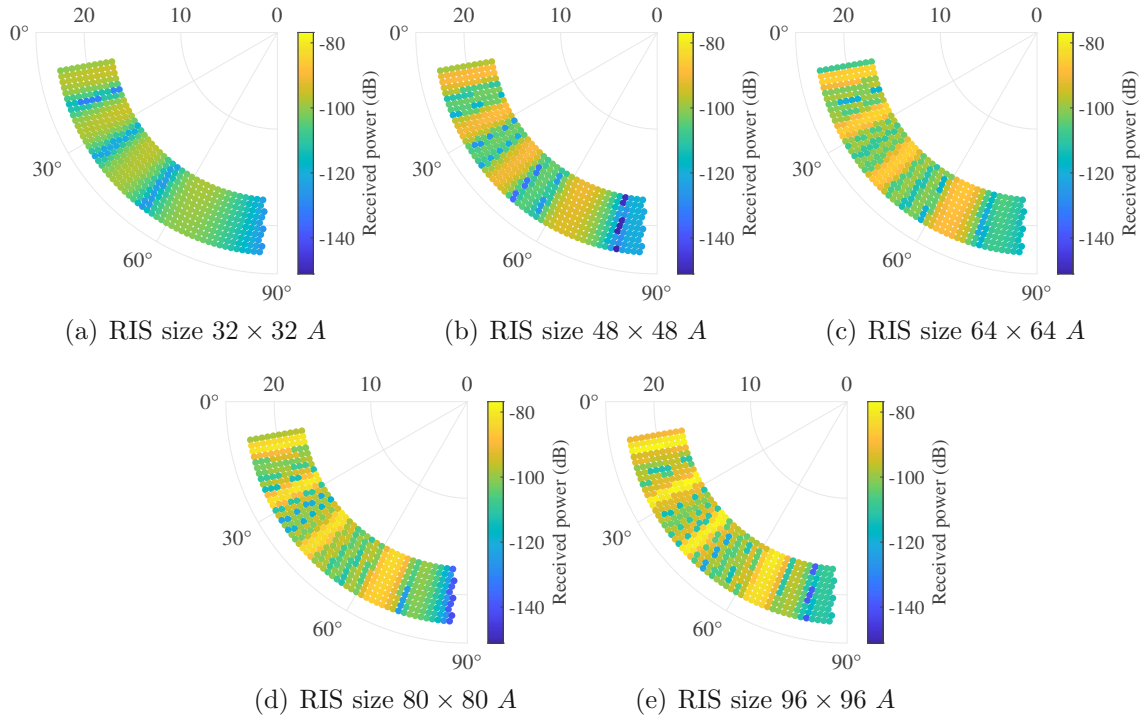


Figure 4.8: Received power vs. angles and distances between the Rx's and the RIS with different RIS sizes without reflections.

blocked by two inner walls in the room. The Tx antenna is a horn antenna with a maximum gain of 18.5 dBi toward 0° from the RIS. To investigate how the Rx antenna location influences the received power, we place 450 test omnidirectional Rx antennas at different locations in the room, shown as blue icons. The spacing between the adjacent Rx antennas is 0.6 m.

The RISs for mode 1 to mode 4 with five different sizes are placed at the same location in the room with their receiving beams toward the Tx antenna. The distance between the Tx and the RIS is set to 22 m, and the distance between the RIS and the Rx antenna is from 17.4 m to 22.8 m to fulfill the far-field assumption. The Rx antennas are placed at 10 arcs with the RIS location being the center point of the arcs. The angle range of the Rx antennas toward the RIS is from 10° to 85.4° from northwest to southeast in the room. The height of Tx, Rx, and the RIS is 1.5 m.

To investigate whether the Rx antennas at different locations benefit from the RIS, we simulate the LOS path from the Tx to the RIS and from the RIS to each Rx antenna for all four modes. Then we take the maximum received power for each Rx antenna among all four modes. In this way, the Rx antennas located at 13° , 27° , 43° , and 65° should all receive strong power due to the RIS assistance. The received power for all the users at different angles and distances from the RIS is plotted in Fig. 4.8. Figures 4.8(a), 4.8(b), 4.8(c), 4.8(d), and 4.8(e) display the results for the $32 \times 32 A$, $48 \times 48 A$, $64 \times 64 A$, $80 \times 80 A$, and $96 \times 96 A$ RIS sizes, respectively. The radius of the polar plot is the distance between the Rx and the RIS. The RIS is

4.4. Ray tracing simulations

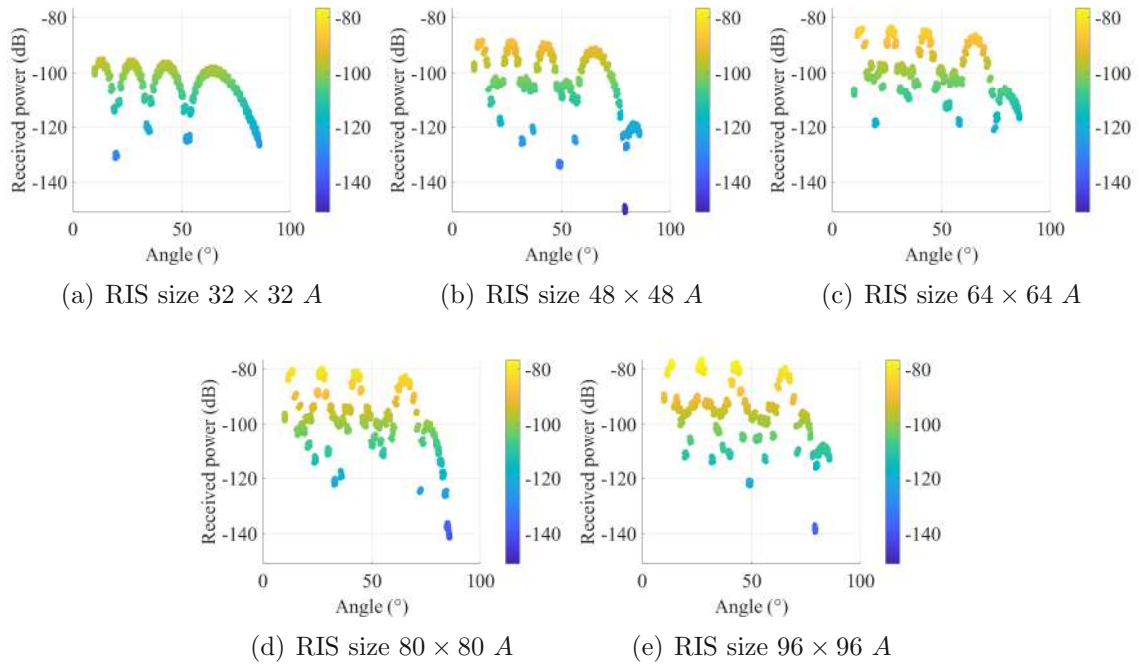


Figure 4.9: Received power vs. the angles between the users and the RIS for different RIS sizes without reflections.

located at point 0 in these figures. The color of these figures' curves represents the received power.

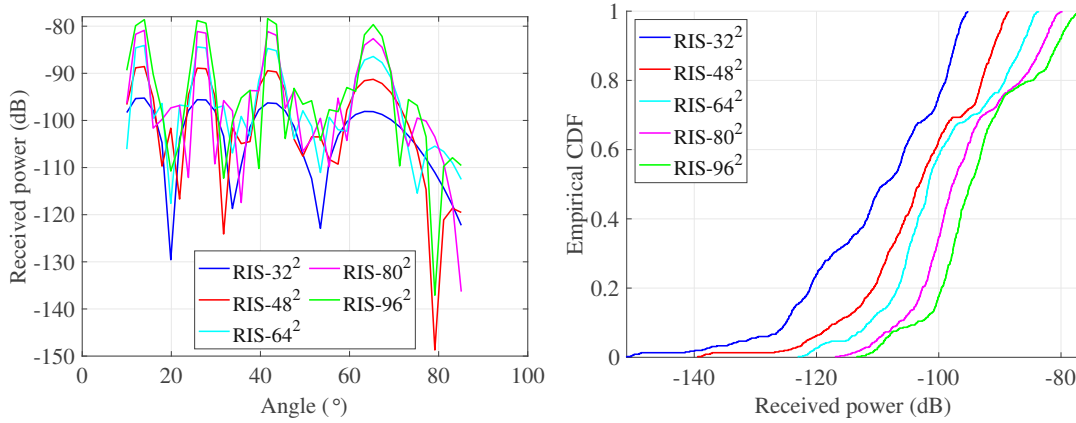
From Fig. 4.8 we can observe that the Rxs located at 13° , 27° , 43° , and 65° receive the highest power. The Rxs at other angles receive lower power because there is no strong reflection from the RIS in those angle ranges. With an increased distance between the RIS and the Rx antenna, the received power is slightly reduced. However, since the distance change is not so much from 17.4 m to 22.8 m, the power reduction is not so significant. The maximum received power at the Rxs increases from -92.4 dB to -74.5 dB with the RIS size increasing from $32 \times 32 A$ to $96 \times 96 A$.

To have a more detailed look at the received power at different angles, we plot the received power versus the angle results in Fig. 4.9. At each angle, there are multiple points representing multiple Rx antennas at that angle with different distances from the RIS. From Fig. 4.9(a) to 4.9(e) are the results for $32 \times 32 A$ to $96 \times 96 A$ RIS sizes, respectively. It is obvious that the received power at the Rxs forms four strong beams at the four RIS reflection directions, which is related to the RIS scattering pattern. When the RIS size increases, the scattering pattern of the RIS at each reflection angle also becomes more directive and stronger.

Next, we choose 39 Rx antennas that are on the first arc at the 17.4 m distance from the RIS. The received powers at the Rx antennas for five RIS sizes are plotted in Fig. 4.10(a). The calculated differences of received powers at different RIS reflection angles are consistent with the results for the SISO scenario in Sec. 4.4.1. When the angle toward the Rx antenna is not at one of the RIS reflection angles, the received

4.4. Ray tracing simulations

power of these Rx antennas is much lower. The differences between the five RIS sizes at those angles are also not very significant. The ECDF results are plotted in Fig. 4.10(b) to compare the overall received power at all the Rx antennas for the five RIS sizes.



(a) Received power vs. the angles toward the users at the same distances to the RIS (b) ECDF of the received power comparison.

Figure 4.10: Received power comparison for different RIS sizes without reflections.

4.4.3 Multi-user scenario with multi-path propagations

In this section, we consider a multi-path propagation scenario. The setup is the same as in Sec. 4.4.2, except that in this scenario we include reflection paths. It should be noted that since our RIS is designed for illumination at normal incidence and reflections into a set of four angles, it can be effectively used only for these paths and for the reciprocal ones. The RIS scattering patterns for illuminations from other directions need to be calculated separately (for RIS realized as periodical arrays, this issue is considered in [69]). For simplicity, here we consider only one LOS path for the Tx-RIS link, but three reflection paths for the RIS-Rx link. To investigate the difference of the received power at the RIS between the LOS path and reflection paths, we run simulations with 0, 3, and 6 reflections, and find that the difference between the LOS and 3 or 6-reflections paths is smaller than 1 dB, which is very small. Hence, even though it is not so realistic to assume only one LOS path between the Tx and the RIS, it is still reasonable to use this assumption for simulations.

The received power results versus the distances to the Rx antenna and the angles are shown in Fig. 4.11. In addition to the results with five RIS sizes that are shown in Figs. 4.11(b)-4.11(f), the results without RIS are plotted in Fig. 4.11(a). From these figures, we notice that when there is no RIS, only some Rx antennas located in the range of $[10^\circ 41^\circ]$ receive relatively high power, while many Rx antennas receive only noise. However, when including an RIS in this scenario, almost all Rx antennas can be covered and can receive a significant amount of signal power.

4.4. Ray tracing simulations

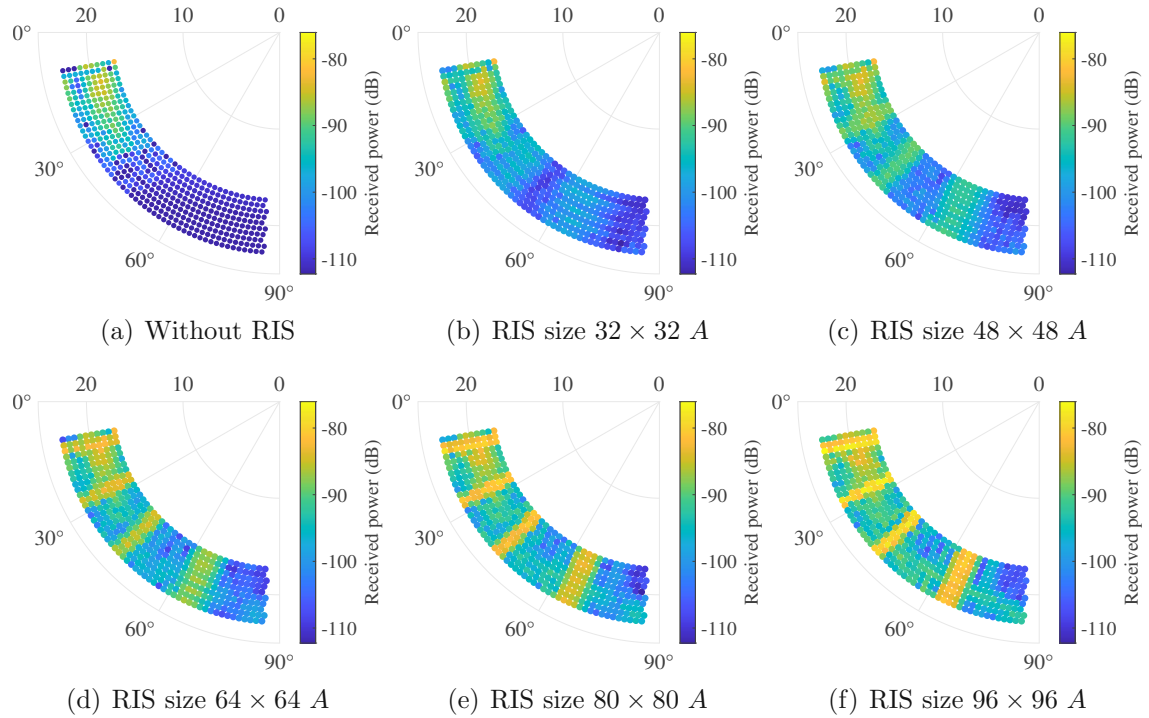


Figure 4.11: Received power vs. angles and distances between the users and the RIS of different sizes with 3 reflections.

The received power as a function of the angle is plotted in Fig. 4.12. When the RIS size is very small, i.e., $32 \times 32 A$ and $48 \times 48 A$, the reflection paths in the room from the Tx-Rx link are dominant while the contribution from the RIS is relatively small. The four peaks at the four RIS reflection angles become more and more strong when the RIS size increases. With a larger than $64 \times 64 A$ sized RIS, the received power at the RIS targeted users achieve significant improvement. When comparing to the LOS scenario in Fig. 4.9, the received powers at the users that are not located along the RIS reflection directions have also improved due to the multi-path reflections. It is obvious that after multiple reflections from the walls, floors, ceilings, and cabinet, the transmitted signals have a good chance of reaching those Rx antennas in blind spots.

Similarly, in Fig. 4.13(a) we compare the results for RIS of five sizes with 39 Rx antennas at the first arc that are 17.4 m away from the RIS. Compared to the case without RIS, the scenarios with RIS lead to significant improvement of received power at these Rxs, especially at the RIS reflection directions and with a larger RIS size. The ECDF results of the received power are plotted in Fig. 4.13(b). The curve for the case of “No RIS” does not start from zero because some Rxs receive just noise, and they are not included in this figure.

4.5. Final remarks

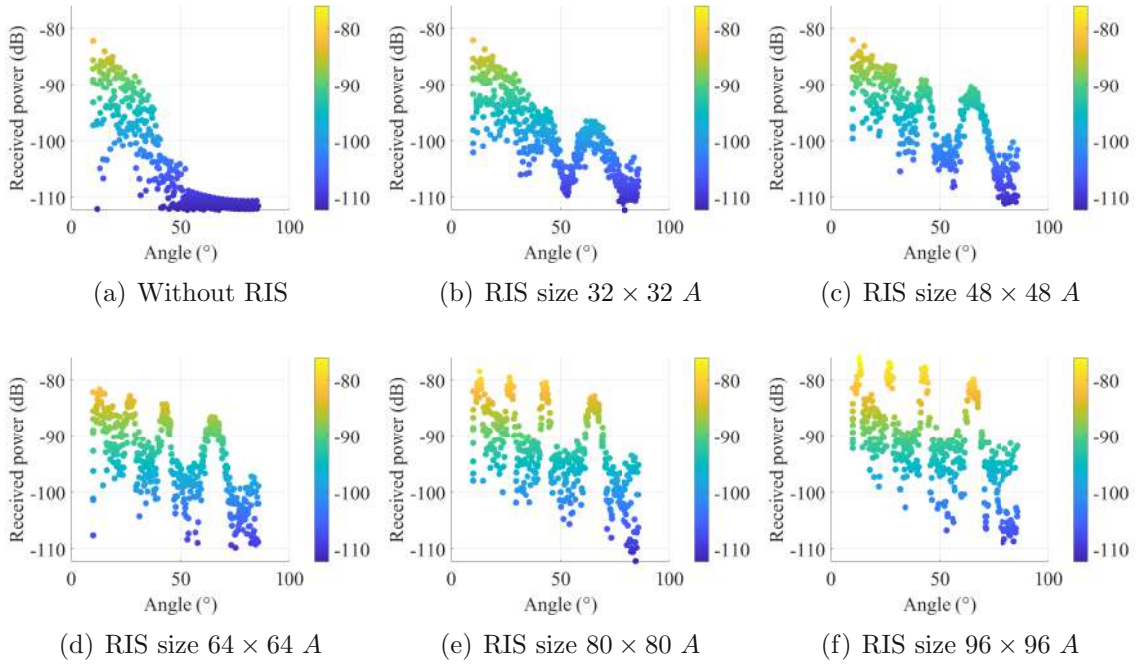
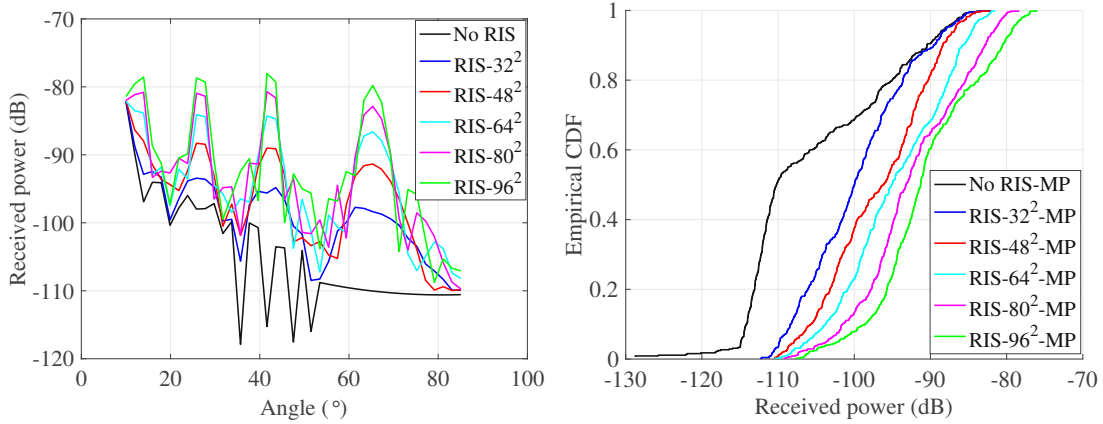


Figure 4.12: Received power vs. angles of the users and the RIS of different sizes with 3 reflections.



(a) Received power vs. angles of the users which have the same distances to the RIS

Figure 4.13: Received power comparison with different RIS sizes with 3 reflections.

4.5 Final remarks

In this chapter, we introduced a designed periodic multimode RIS that supports multiple reflection directions based on a recently developed, computationally simple array scattering synthesis method. By optimizing the load impedance of each unit cell, with continuous and 1 to 4-bit resolution quantized reactive loads, the

RIS can be configured to reflect waves toward one main direction while suppressing reflections in other directions. The designed lossless RIS can achieve almost perfect reflection efficiencies in the desired directions. Furthermore, we investigated the quantization effect on the RIS implementation and concluded that with a 3-bit quantization resolution, the RIS can already achieve very good results. Next, we analyzed the large-scale fading of RIS-assisted communication links through EM simulation, system-level, and ray tracing simulations. We implemented the RIS into the MATLAB ray tracer by importing the radiation patterns of the designed RIS into the ray tracer. In addition, we transfer the other EM properties of the designed RIS to the RIS-tailored Vienna SLS, such as RIS gain, geometrical area, incident angle, and reflection angle, to evaluate the large-scale fading theoretically.

The theoretical analysis and ray tracing simulation results demonstrate that our strategy of implementing an RIS as an antenna in a ray tracer is correct, which can also be applied to other ray tracers. The ray tracing simulation results from a SISO and multi-user LOS scenario prove that the maximum received powers at the Rx antennas fulfill the power scaling law [30], which is actually from the communication theory where it just considers the RIS element number and phase shifts and does not involve any EM properties of the RIS, but our RIS model is from EM perspective and modeled as a whole antenna. So far, we have reached a good agreement when applying the communication theory to a perfectly designed RIS from the EM perspective. In addition to the comparison between the scenario with multiple reflections and without reflections, we can conclude that the contributions of an RIS are highly dependent on its reflection directions, the RIS sizes, and the reflections from the environment. The user located at the RIS reflection angles can receive the highest power, the bigger RIS size also contributes more power to the user, and reflection paths in the environment can contribute to the user coverage improvement.

5

RIS model verification with a realistic anomalous reflector

In Chapter 4, we verified our RIS models and implementations in the ray tracer with a perfectly designed RIS. The theoretical analysis and simulations achieve good agreement. In this chapter, we further verify our methods of RIS analysis with a realistic AR, and compare our analysis results with measurements. Current researches usually focus on the electromagnetic parameters of ARs, such as the anomalous reflection efficiency and scattering pattern, but no proper analysis is done of communication aspects in realistic environments. On the contrary, the majority of research communication aspects of the use of an AR are based on simplified or even idealized models that have not been validated for realistic ARs that are designed using electromagnetic theory methods. There is also a lack of work on the frequency selectivity and spatial scalability of ARs.

In this chapter, we are filling these gaps by bringing the electromagnetic parameters of an EM-designed and manufactured AR to different communication models and software that are often used in communication system modeling. We theoretically evaluate large-scale fading of AR-assisted communication links and use a ray tracer to simulate a realistic indoor scenario in the presence of an anomalous reflector. The theoretical and ray tracing models have been compared and verified by measurements. More precisely, we elaborate on the concept of scalable AR to analyze the angular response, frequency response, and spatial scalability of a manufactured 3-bit AR across a broad range of angles and frequencies. We utilize two theoretical models and ray tracing simulations to investigate the communication performance of two different-sized scalable finite ARs, one smaller configuration with 48×48 array of unit cells and the other constructed by combining four smaller ARs to form a larger array with 96×96 unit cells. To validate the developed theoretical approach, we conducted measurements in a dense indoor scenario to evaluate the received power through an AR link at different angles and frequencies. In addition, models of scalable deflectors are implemented in the MATLAB ray tracer to simulate the measurement scenario.

Since the implementation of the AR in a ray tracer has been verified by simula-

tion and measurements, this method can be used for any type of AR. As long as the scattering pattern of the AR is available from analytical estimations, simulations, or test measurements, we can use a ray tracer to obtain very accurate results for communication links in complex environments without the need to perform measurements in every particular setting. The work expressed in this chapter is based on our submitted publications [23, 25].

5.1 Practical anomalous reflector design and fabrication

Continuing with the perfect AR in Sec. 4.1, we aim to manufacture an AR prototype and perform measurements with it in a real environment to validate our RIS models. Due to the equipment limitations, we could not manufacture a reconfigurable AR as we used in Chapter 4 at the moment. However, we can tweak the design a bit and produce a static AR prototype that can reflect the normal direction incident wave in one fixed angle. Thus, we manufacture four pieces of 48×48 -sized ($13.24\lambda \times 13.24\lambda$) AR with an in-house printed circuit board (PCB) manufacturing facility as a dual-layer laser-etched PCB including galvanic through-hole plating process. This practical AR is designed for a center frequency of 26 GHz and it reflects wave at 65° (mode 4).

We use the same manufacturing process as stated in [64], where each unit cell is constructed by a square copper patch applied on top of a PCB which uses Rogers RO4350B (LoPro) laminate with a 0.52 mm thickness (relative permittivity $\epsilon_r = 3.55$, loss tangent $\tan \delta = 0.0037$). We model the materials in CST as lossy and assign a surface roughness of 0.001 mm for the copper layer. The square patch dimension is 2.385 mm, with its feeding position located at $(x_p, y_p) = (1, 0)$ mm. These dimensions are optimized to achieve resonance at 75Ω input impedance tailored for the desired frequency of 26 GHz. Each unit cell within a supercell is loaded with a reactive impedance implemented by shorted and open coplanar waveguide (CPW) strips according to the simulation-based optimization described in [64]. The load impedance of the prototype is optimized with a 3-bit quantization since this resolution is assumed to be sufficient for the reactive loads based on the analysis in Sec. 4.3. The detailed phase and reactance, as well as the strip length of the design, are listed in Table 5.1. The final manufactured AR prototype is shown in Fig. 5.1. This approach balances the precision and practicality of the proposed design technique in the implementation process and simplifies hardware requirements for manufacturing.

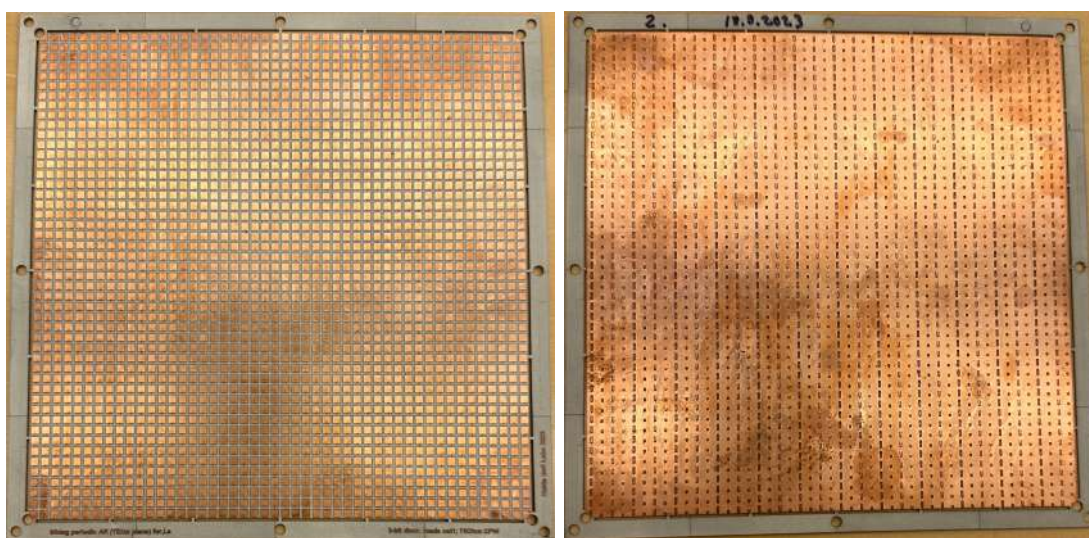
5.2 EM measurement of the manufactured AR

To verify the EM property of the manufactured AR prototype, we conduct a measurement in an anechoic chamber in the Nokia campus in Espoo, Finland. The

5.2. EM measurement of the manufactured AR

Table 5.1: CPW strip dimensions

No.	Phase	Reactances (Ω)	Strip (mm)	Term.
1	0	106	1.18	short
2	$\pi/4$	49	0.89	short
3	$\pi/2$	13	0.54	short
4	$3\pi/4$	-19	1.79	open
5	π	-58	1.44	open
6	$-3\pi/4$	-133	1.06	open
7	$-\pi/2$	-583	0.62	open
8	$-\pi/4$	294	1.48	short



(a) Front side.

(b) Back side.

Figure 5.1: A manufactured 48×48 -sized anomalous reflector.

measurement scenario and devices are shown in Fig. 5.2, where we place the Tx and the AR in a fixed location with a distance of 3 m, and move the Rx antenna from -90° to 90° with a 5° step with respect to the AR with a fixed distance of 2 m. The Tx and Rx antennas are the same horn antennas with a 18 dBi gain at 26 GHz. During measurement, the Tx antenna is connected to an R&S vector signal generator (VSG), and the Rx antenna is connected to a vector signal analyzer (VSA). The LOS path between the Tx and the Rx antenna is blocked by a wave absorber, whereas there are always LOS paths for the Tx-AR and AR-Rx links.

Since the far-field distance for this AR is about 4.04 m, the Tx and the Rx antennas are actually in the radiating near-field of the AR. However, we can still use the measured results to estimate the main lobe shape of the AR scattering pattern. In addition to the designed frequency 26 GHz, we also conduct measurements at 25 and 27 GHz. The normalized scattering pattern results of the AR obtained from the measurement and CST simulations are shown in Fig. 5.3. The measurement results

5.3. Communication measurement of the manufactured AR

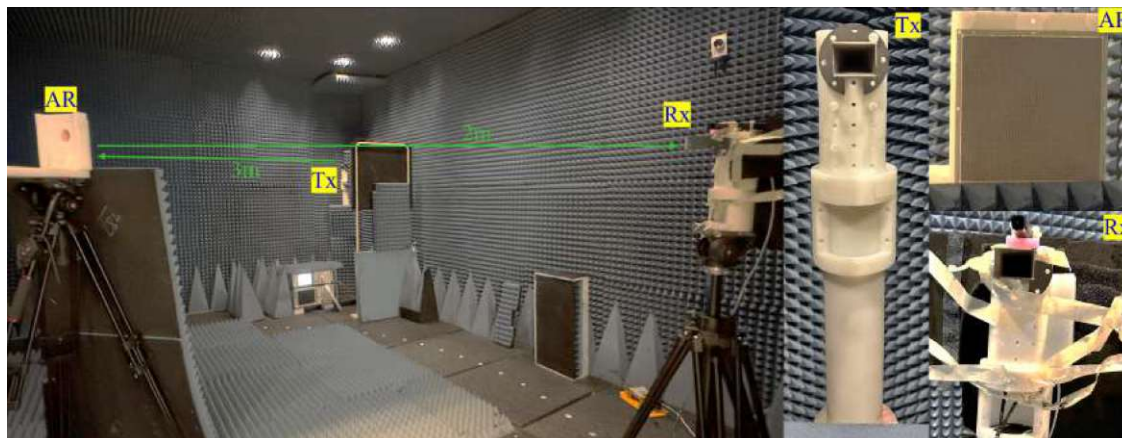


Figure 5.2: Measurement scenario.

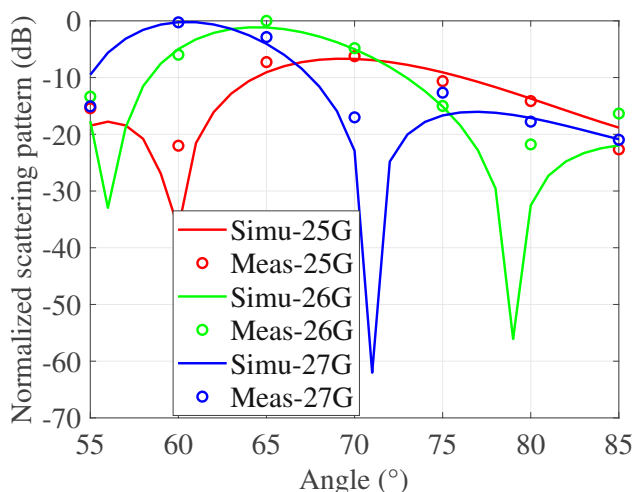


Figure 5.3: Normalized scattering pattern of the 48×48 -sized AR at different frequencies and angles from CST simulation and measurement.

are in good agreement with the CST simulation results in the main beam directions. It should be mentioned that the AR was originally only designed for 26 GHz, but the results indicate it also works well at 25 and 27 GHz, with the main reflection direction shifted for 5° . For example, the main reflection direction occurs at 70° , 65° , and 60° from 25 GHz to 27 GHz, respectively.

5.3 Communication measurement of the manufactured AR

In this section, we aim to use this realistic AR in our theoretical models and ray tracing tool to verify our implementations and communication models, as well as to evaluate the performance of this reflector in a real environment. Therefore, we



(a) The measurement scenario in an auditorium.

(b) 48×48 -sized AR. (c) 96×96 -sized AR.

Figure 5.4: Measurement scenario and equipment.

perform over-the-air measurements at 26 GHz with the same prototype in an auditorium at the Nokia Bell Labs office in Espoo to test the communication link performance and our ray tracing model.

5.3.1 Measurement campaign

Measurement scenario and setups

The measurement was conducted in a $14 \times 8 \times 3$ (m^3) sized auditorium at the Nokia Bell Labs office in Espoo, Finland. As shown in Fig. 5.4(a), the Tx and Rx antennas are the same horn antennas with a maximum gain of $G_t = G_r = 18$ dBi and a beam width of 22° at 26 GHz. The heights of the Tx, Rx antennas, and the AR center are 1.5 m. The distance between the Tx and the AR is $d_t = 5.5$ m, and the distance between the AR and the Rx antenna is always $d_r = 7$ m. Throughout the measurement campaign, we avoided moving objects in the room.

The measurement setup is shown in Fig. 5.5. The Tx horn antenna is connected to an R&S VSG SMW200A via a cable and then connected to a control computer. The Rx horn antenna is connected to a low-noise-amplifier (LNA) Miteq JS4 with a noise figure of 2.7 dB, and the LNA is then connected to a R&S FSW VSA via cables. The VSA is connected to the VSG via an Ethernet cable and reference clock for synchronizing the signals. The parameters of the devices are listed in Table 5.2. The transmitted power from the Tx antenna is $P_t = 6$ dBm, the Tx cable loss is $L_t = 2.5$ dB, the sum of the LNA gain and the Rx cable loss is $G_a = 19.9$ dB at 26 GHz. The VSG generates a 5G NR PUSCH signal within a channel bandwidth of 400 MHz or 100 MHz for 16 quadrature amplitude modulation (QAM) or 64 QAM orthogonal frequency-division multiplexing (OFDM) modulation scheme.

Reference measurement of LOS links

To obtain accurate measurement results and have a fair comparison with simulation results, we first conduct a reference measurement with only LOS links between the Tx and the Rx antenna. Next, we compare the measured results with theory to find

5.3. Communication measurement of the manufactured AR

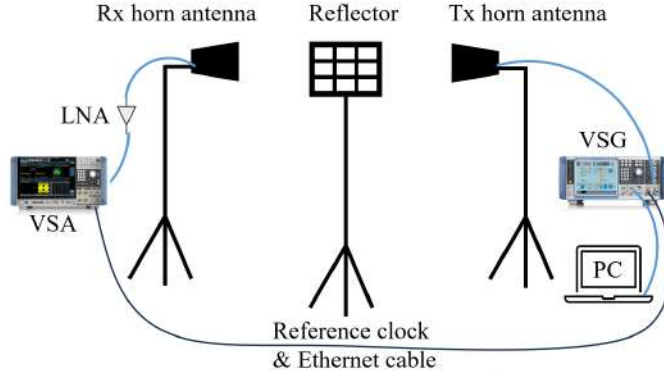


Figure 5.5: Measurement setup.

Table 5.2: MEASUREMENT PARAMETERS

	Item	value
Transmit power	P_t	6 dBm
Cable loss at Tx side	$(-L_t)$	-2.5 dB
Tx antenna gain	G_t	18 dB
Rx antenna gain	G_r	18 dB
LNA gain + cable loss at Rx side	G_a	19.9 dB
Distance between the Tx and AR	d_t	5.5 m
Distance between the Rx and AR	d_r	7 m

out how much power difference we obtain between them. During the measurement, we fix the Tx antenna position and move the Rx antenna to 8 different locations, i.e., $55^\circ, 60^\circ, 62.5^\circ, 65^\circ, 70^\circ, 75^\circ, 80^\circ$, and 85° from the AR, respectively. At each Rx location, we orient the Tx and Rx antennas to let their main beam directions face each other, and we measure the received power at the Rx antenna through the LOS path from the Tx antenna. Firstly, we conduct measurements with 16 QAM modulated waves with a 400 MHz bandwidth for each frequency. Since this kind of measurement takes a long time with the used instrumentation, we measure only at three distinct frequencies, i.e., 25, 26, and 27 GHz with the OFDM modulated signals. For reference, we also use continuous wave signal to sweep from 24.5 GHz to 27.5 GHz with a step of 0.25 GHz to have proper frequency responses and a quicker measurement setup.

We denote the received power value from modulated wave measurement as $\mathbf{P}_{m,mod}$ which is a 3×8 matrix containing the results at three frequencies and eight angles. The received power $\mathbf{P}_{m,con}$ from continuous wave measurement is a 13×8 matrix corresponding to the 13 sweep frequencies. Then we calculate the free space path loss between the Tx and the Rx at each wavelength λ_i and each location d_i using the Friis formula

$$P_{FSPL,i} = \left(\frac{\lambda_i}{4\pi d_i} \right)^2 \quad (5.1)$$

in W , where $d_i \in [5.88, 6.25, 6.67, 6.79, 7.27, 7.70, 8.10, 8.42]$ (m) denotes the 8 dis-

5.3. Communication measurement of the manufactured AR

Table 5.3: POWER DIFFERENCES BETWEEN THEORY AND MEASUREMENTS

$\mathbf{P}_{\text{diff,mod}}$ (dB)	55°	60°	62.5°	65°	70°	75°	80°	85°
25 GHz	0.87	0.78	1.05	0.77	0.25	0.14	0.28	1.52
26 GHz	1.46	1.55	0.21	1.08	0.68	0.26	1.05	0.28
27 GHz	1.04	2.13	1.11	1.56	1.33	1.79	-0.04	1.85

tances between the Tx and the Rx antenna corresponding to the 8 angles. The λ_i corresponds to the 13 frequencies from 24.5 GHz to 27.5 GHz. The final calculated received power from theory is

$$P_{\text{theory},i} = P_t + G_t + G_r + P_{\text{FSPL},i} - L_t + G_a \quad (5.2)$$

in dBm. When collecting the results from all the frequencies and locations, we can denote them in matrices as \mathbf{P}_{FSPL} and $\mathbf{P}_{\text{theory}}$ both with the size of 13×8 . The power difference between the theoretical and measurement results is

$$\mathbf{P}_{\text{diff,mod}} = \mathbf{P}_{\text{theory}} - \mathbf{P}_{\text{m,mod}} \quad (5.3)$$

in dB and

$$\mathbf{P}_{\text{diff,con}} = \mathbf{P}_{\text{theory}} - \mathbf{P}_{\text{m,con}} \quad (5.4)$$

in dB. Note that we only pick three values of the 25, 26, and 27 GHz frequencies from $\mathbf{P}_{\text{theory}}$ for the power difference with modulated wave $\mathbf{P}_{\text{diff,mod}}$, but use the whole 13×8 matrix of $\mathbf{P}_{\text{theory}}$ for the power difference with continuous wave $\mathbf{P}_{\text{diff,con}}$.

In Table 5.3, we list the $\mathbf{P}_{\text{diff,mod}}$ with modulated measurement results at the three frequencies. These small differences may come from the losses in the measurement system that we could not count in our model. The losses due to measurement devices may have a little deviation between the measurement and simulation. For instance, the antenna gain variability at different frequencies is about 0.5 dB. The LNA gain and the Rx cable loss together have about 1.6 dB variation, and the Tx cable loss has around 0.065 dB variability in the frequency range. When we take $\mathbf{P}_{\text{diff,mod}}$ or $\mathbf{P}_{\text{diff,con}}$ into account, and use them to correct the calculated and simulated results with the AR, we can eliminate the influence of these factors and obtain more accurate results between the simulation model and the measurement.

Measurement with the 48×48 -sized AR

After the LOS links measurements, we perform over-the-air measurements in the auditorium with the manufactured 48×48 -sized AR (152.6 mm×152.6 mm) as shown in Fig. 5.4(b), to evaluate its beamforming performance in the communication aspect, i.e., the large-scale fading through the Tx-AR-Rx link. We fix the positions of the AR and the Tx antenna with a distance of 5 m and make their main beam directions face each other. Then we move the Rx antenna from 55° to 85° with a 5° step and with a fixed distance of 7 m. Since the simulated half power beam width (HPBW) of the 48×48 -sized AR is 9°, a 5° step is enough to catch the peak power.

5.3. Communication measurement of the manufactured AR

Every time when we move the Rx antenna, we redo the orientation of the Rx antenna to make its main beam direction always face the AR. There are LOS paths between the Tx and the AR and between the AR and the Rx antenna, while the direct link between the Tx and the Rx antennas is blocked by a wave absorber. Same as the previous LOS measurement, we first perform measurements with 16 QAM modulated OFDM waves with 400 MHz bandwidth at the frequency 25, 26, and 27 GHz, and obtain the results of received power and error vector magnitude (EVM) at the Rx antenna through the Tx-AR-Rx link. The EVM is a parameter in communications systems to indicate the received signal quality throughout the measured channel bandwidth for evaluating the conditions of the received signal demodulation. Next, we repeat the measurements with continuous waves from 24.5 GHz to 27.5 GHz. In the end, we obtain 3×7 and 13×7 different received power values at the Rx antenna from the 7 different locations and from the 3 and 13 frequencies corresponding to modulated waves and continuous waves, which are denoted as $\mathbf{P}_{s,\text{mod}}$ and $\mathbf{P}_{s,\text{con}}$, respectively.

Measurement with the 96×96 -sized AR

To explore the spatial scalability of the manufactured AR, we combine four identical pieces of the 48×48 -sized AR to form a big AR with the size of 96×96 (305.3 mm \times 305.3 mm). We use copper tape to glue the edges to ensure continuous alignment of elements with neighboring small ARs in the same plane and thus to avoid or minimize the misalignment of the AR elements. The combined 96×96 -sized AR is displayed in Fig. 5.4(c). We then repeat the measurement with the big AR in the auditorium to investigate its performance. All the measurement settings are the same as with the small AR, except that we did all measurements at an additional angle of 62.5° for the 96×96 -sized AR since the simulated HPBW of the 96×96 -sized AR is 5° and the peak power is likely to occur between 60° and 65° . Therefore, we have 8 angles for the big AR measurements. In addition to the 16 QAM modulated waves, we also perform measurements using 64 QAM modulated waves with 100 MHz bandwidth. It should be noted that the far-field distance for the 48×48 and 96×96 -sized ARs are 4.04 m and 16.17 m, respectively, the far-field distance of the big AR is not fulfilled anymore in our measurement. Therefore, the 48×48 -sized AR is in the far-field region of the Tx and the Rx antennas, but the 96×96 -sized AR is in the radiating near-field region. Finally, we obtain two received power matrices from modulated and continuous wave measurements denoted as $\mathbf{P}_{b,\text{mod}}$ and $\mathbf{P}_{b,\text{con}}$, respectively.

5.3.2 Theoretical analysis

Similar to Chapter 4, we analyze the large-scale fading of this realistic AR with the same path loss models. The first method uses Eq. (3.11) to estimate the path loss of far-zone links through a perfectly working AR. Therefore, we expect reduced performance with our manufactured AR using this model, since it consists of lossy

5.3. Communication measurement of the manufactured AR

materials and 3-bit quantized load impedance. The parameters of the AR with this method read $S_1 = (0.2758\lambda)^2 N$ with the number of unit cells $N = 48^2$ for the smaller AR and $N = 96^2$ for the big AR. The η_{eff} is set to one as the same as the previous chapter. The received power at 26 GHz and at the 65° location through the AR from method 1 is calculated as

$$P_1 = P_t G_t G_r \eta_{\text{eff}} \left(\frac{S_1}{4\pi d_t d_r} \right)^2 |\cos \theta_i \cos \theta_r| \quad (5.5)$$

in W . For each AR, we obtain one scalar value of the received power P_1 at 65° with one distance d_r since the manufactured AR is designed for illumination at normal incidence and the 65° reflection angle at 26 GHz. Considering the measurement setup parameters, the final received power at the Rx antenna should be $P_{r1} = P_1 - L_t + G_a$ in dBm.

Next, we use the same path loss model for method 2 in Chapter 4, which is written as:

$$P_{2,i} = \frac{P_t G_t G_{\text{rx}} G_{\text{tx},i} G_r \lambda_i^4}{(4\pi)^4 (d_t d_{r,i})^2} \quad (5.6)$$

in W for each location and each frequency. We use a 13×8 matrix \mathbf{P}_2 to denote the results for all 13 frequencies and 8 angles. The difference of this model between this section and in Chapter 4 is that the G_{rx} and G_{tx} values are from the perfectly designed RIS in Chapter 4, while in this section, we use the values for the manufactured AR. They are obtained from CST simulations in the same way. Similarly, the received power results from method 2 are calculated as $\mathbf{P}_{r2} = \mathbf{P}_2 - L_t + G_a$ in dBm.

Now, when we take the power differences between theory and measurement into account, we use the $\mathbf{P}_{\text{diff,mod}}$ and $\mathbf{P}_{\text{diff,con}}$ as correction factors to calibrate the calculated results. The corrected power from the AR-assisted link from method 1 is obtained by

$$P_{1,\text{mod}} = P_{r1} - P_{\text{diff,mod}} \quad (5.7)$$

and

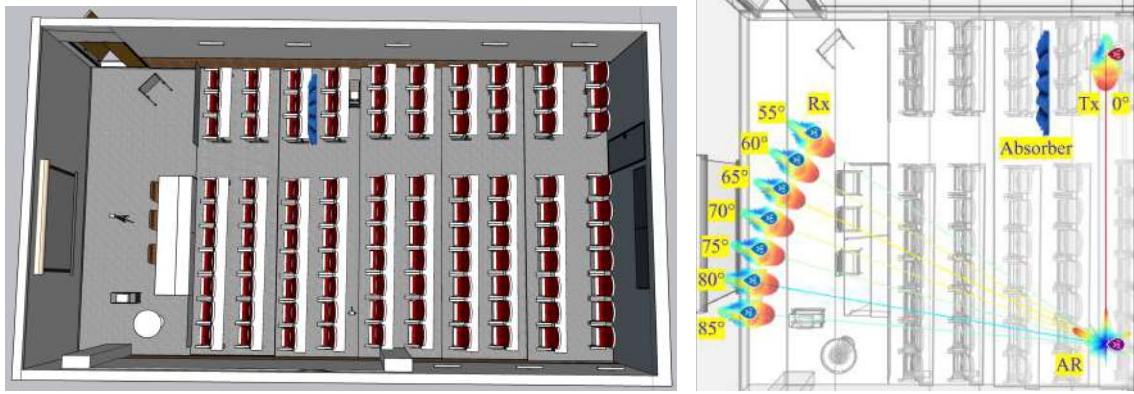
$$P_{1,\text{con}} = P_{r1} - P_{\text{diff,con}} \quad (5.8)$$

corresponding to the modulated and continuous waves. Note that here we only pick the value at 65° and 26 GHz from $\mathbf{P}_{\text{diff,mod}}$ and $\mathbf{P}_{\text{diff,con}}$. Similarly, the corrected power from method 2 is calculated by

$$\mathbf{P}_{r2,\text{mod}} = \mathbf{P}_{r2} - \mathbf{P}_{\text{diff,mod}} \quad (5.9)$$

and

$$\mathbf{P}_{r2,\text{con}} = \mathbf{P}_{r2} - \mathbf{P}_{\text{diff,con}}. \quad (5.10)$$



(a) A top view of the 3D auditorium model, which is replicated with a 1:1 ratio from the actual sizes.

(b) The Tx, Rx, and AR positions and radiation patterns in the MATLAB ray tracer, as well as the LOS paths between them.

Figure 5.6: The 3D auditorium model and LOS paths in the ray tracer.

5.3.3 Ray tracing model

To reproduce the measurement scenario for ray tracing simulations, we first create a 3D model of the auditorium and objects inside with their actual dimensions in the software SketchUp, then import the 3D model to the MATLAB ray tracer for simulations. The top view of the 3D model is shown in Fig. 5.6(a). We model a horn antenna with a maximum gain of 18 dBi as Tx and Rx antennas and import the radiation patterns of the AR from CST simulations to the ray tracer. We place the Rx antenna at different positions from 55° to 85° and orient the main beam of the Rx antenna pattern to always face the AR. In Fig. 5.6(b), we plot the LOS paths between the Tx and the AR, and between the AR and the Rx in the MATLAB ray tracer. The locations and heights of the Tx, Rx, and AR are the same as in the measurement.

For ray tracing simulations with the two ARs, we set the material type of the auditorium as “concrete” and set the reflection paths as zero or three for comparison. When there is no reflection path, it will only simulate the LOS paths as shown in Fig. 5.6(b), and the path loss calculation is based on the free space path loss model, which is the same as from method 2. The zero-reflection case is used to compare the simulation results with the theoretical model, and to allow for a more practical propagation environment, we set three reflection paths to compare the results with measurement results. We denote the simulated powers at 7 or 8 locations for the small AR or big AR as $\mathbf{P}_{r,\text{orig}}$. Then, considering the cable losses and the LNA gain, we obtain $\mathbf{P}_{\text{RT,orig}} = \mathbf{P}_{r,\text{orig}} - L_t + G_a$.

Next, we use the power difference matrix to calibrate our ray tracing simulation results. The corrected simulation results from ray tracing are obtained by

$$\mathbf{P}_{\text{RT,mod}} = \mathbf{P}_{\text{RT,orig}} - \mathbf{P}_{\text{diff,mod}} \quad (5.11)$$

and

$$\mathbf{P}_{\text{RT,con}} = \mathbf{P}_{\text{RT,orig}} - \mathbf{P}_{\text{diff,con}}. \quad (5.12)$$

5.3.4 Results comparison

In this section, we compare the measurement results from Sec. 5.3.1 ($\mathbf{P}_{\text{s,mod}}$, $\mathbf{P}_{\text{s,con}}$, $\mathbf{P}_{\text{b,mod}}$ and $\mathbf{P}_{\text{b,con}}$), the corrected received power results through the AR-assisted communication links between the theoretical models explained in Sec. 5.3.2 (Eq. (5.7), (5.8), (5.9), (5.10)), and the corrected ray tracing simulation results from Sec. 5.3.3 (Eq. (5.11), (5.12)). We analyze the AR's angular response across various Rx locations, evaluate frequency selectivity by varying frequencies, and assess spatial scalability performance through AR prototypes.

Results of the 48×48 -sized AR

The comparison results of received power and EVM for the 48×48 -sized AR are displayed in Fig. 5.7(a) and Fig. 5.7(b), respectively. Fig. 5.7(b) only shows the EVM values that passed the frame-averaged EVM test with the 5G NR signal (EVM less than 12.5% for 16QAM). We observe that from 25, 26, to 27 GHz, the maximum received power increases while the minimum EVM decreases. The maximum received power and minimum EVM for 25, 26, and 27 GHz occur at 70° , 65° , and 60° , respectively. The angles of the received power peaks at the three frequencies are consistent with the scattering pattern shown in Fig. 5.3.

The comparison of the corrected simulation and theoretical results, as well as the measurement results, are plotted in Fig. 5.8. From these three figures, we observe that the results from method 2 and from ray tracing with zero reflection are consistent, which validates our AR implementation method in the ray tracer. Ray tracing with zero reflection and three reflections also does not make much difference in the

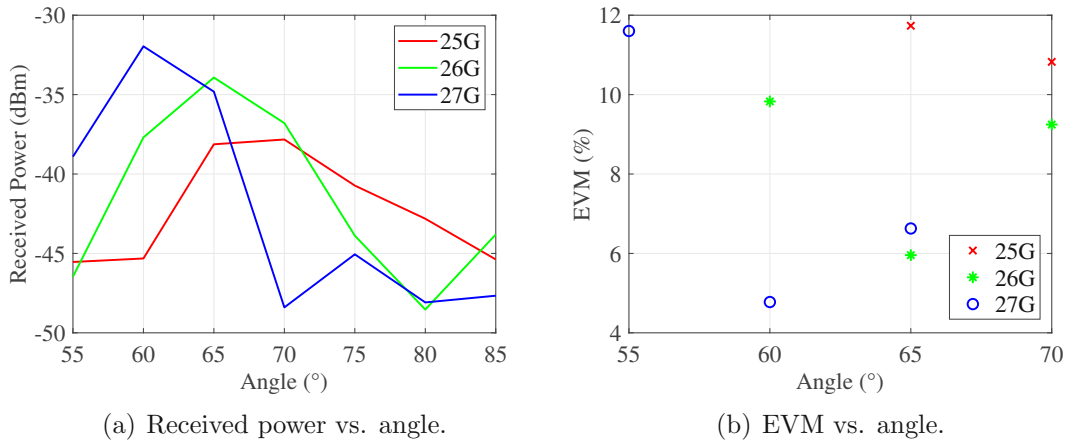


Figure 5.7: Measured results of the 48×48 -sized AR with 16 QAM modulated waves.

5.3. Communication measurement of the manufactured AR

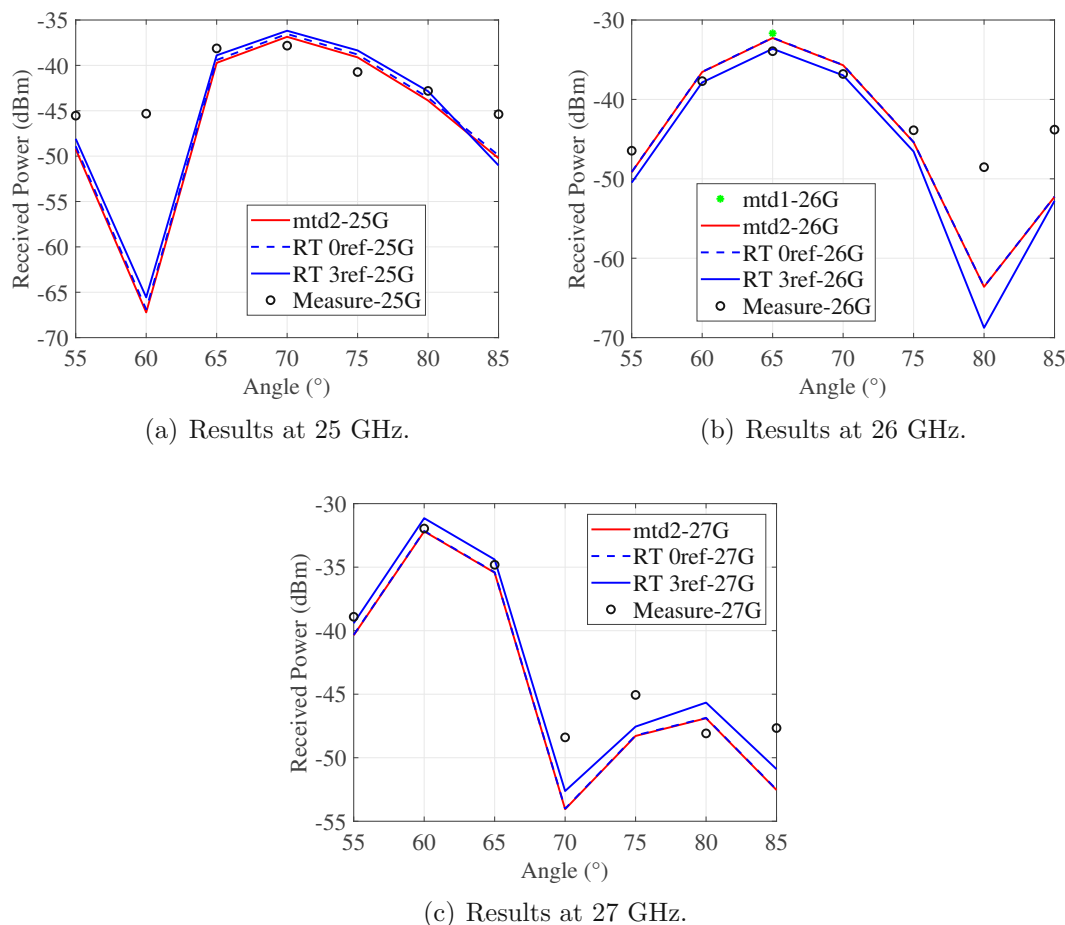


Figure 5.8: Results with the 48×48 -sized AR from corrected calculation and simulation, and from measurements using the modulated waves.

received power. At 25 GHz, the measurement and simulation results have very little difference at most angles, except at 60° . This is highly related to the simulated and measured scattering pattern of the AR, as we see similar circumstances in Fig. 5.3. At 26 GHz, the measurement results at 60° , 65° , and 70° are almost the same as the ray tracing simulation results with three reflections. In addition, the theoretical results from method 1 at 65° are very close to method 2 and ray tracing with zero reflection, which indicates that the 3-bit quantized lossy AR does not have much power loss at the designed reflection angle compared to a perfectly working lossless AR. At 27 GHz, the simulation results and measurement results are almost the same at 55° , 60° , and 65° .

Since the nominal main beam direction of the AR is between 60° and 70° due to the frequency steering phenomenon, we observe the received power results at all 13 frequencies and at 60° , 65° , and 70° which are shown in Fig. 5.9(a)-5.9(c). Generally, we achieve good agreement between the simulations and measurement results, they have big differences only at a few frequency points, which is related to the AR

5.3. Communication measurement of the manufactured AR

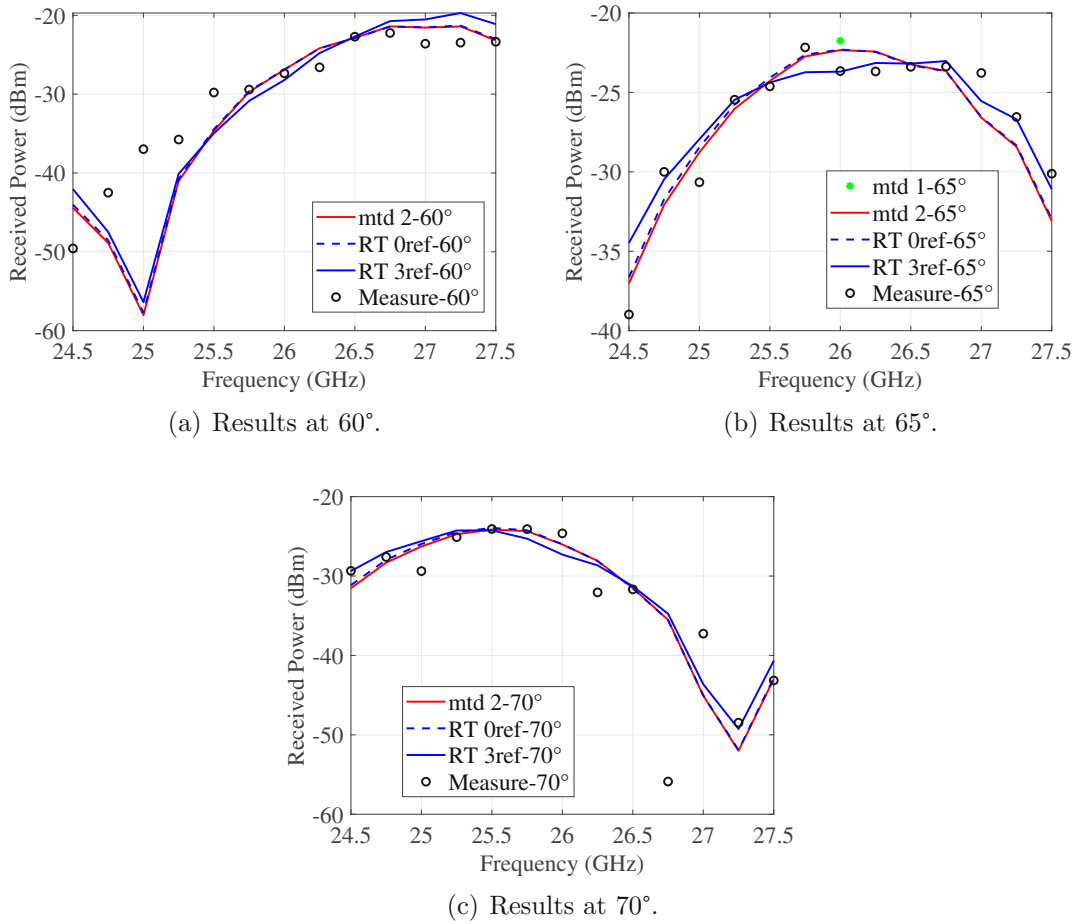


Figure 5.9: Results with the 48×48 -sized AR from corrected calculation and simulation, and from measurements using the continuous waves

scattering pattern difference between simulation and measurements. Since 65° is the designed reflection angle, we see the agreement at this angle is better than in 60° and 70° . In addition, we find that the “frequency steering” phenomenon limits the use of this AR for signal bandwidths greater than 1 GHz approximately. But for any individual center frequencies within the given almost 3 GHz range, we can operate.

These observations confirm that our ray tracing model with the realistic AR gives comparative results as measurement results in such an indoor scenario, even though the 3D model in the ray tracer does not fully replicate the auditorium since we can only set one material type for all objects in the MATLAB version up to 2024a, whereas the materials of different objects in the rooms are different in reality. It is also proved that our theoretical analysis for an AR-assisted link is correct, the 3D auditorium model is accurate, the AR implementation in the MATLAB ray tracer is correct, and the theoretical models and ray tracing methods work not only for a perfect RIS but also for a realistic lossy AR. Next, we can use this method to predict the communication performance of other ARs, especially those that have difficulties

measuring. For example, a 96×96 -sized AR that we could not measure the far-field scattering pattern due to the limitation of measurement condition, but we can use our models to predict the far-field performance.

Results of the 96×96 -sized AR

In this section, we analyze the results for the 96×96 -sized AR which is a tiled combination of the four pieces of 48×48 -sized AR. The received power and EVM results from the big AR are shown in Fig. 5.10(a) and Fig. 5.10(b), respectively. Here we also only plot the EVM results that passed the EVM tests (EVM less than 12.5% for 16QAM and 8% for 64QAM). These results indicate that the maximum power for 25, 26, and 27 GHz appear at 65° , 62.5° , and 60° , respectively. The EVM results are consistent, i.e., the minimum EVM results for the big AR also appear at the same angles for the three frequencies. The main beam direction moves to a smaller angle when increasing the frequency, which is the same as for the small AR. The only difference is that the peak power from the small AR appears at 70° , 65° , and 60° for 25, 26, and 27 GHz, respectively. It also shows that the big AR works well with both 16 QAM and 64 QAM modulation schemes. When changing from 16 QAM to 64 QAM, it can achieve higher data rates and throughput. From the comparison of the results between the two modulation schemes, the 64 QAM modulation results in lower EVM and received power than using 16 QAM, but the differences are not so much. Therefore, we only compare the simulation and calculation results with 16 QAM measurements in the following process.

The received power results from the corrected calculation and simulations, as well as from measurements using modulated waves, are shown in Fig. 5.11. Fig. 5.11(a)-5.11(c) display the results at 25, 26, and 27 GHz, respectively. These three figures show different beam shapes compared to the 48×48 -sized AR, the measured power peak appears in 62.5° while the simulated peak is still in 65° at 26 GHz. However, an

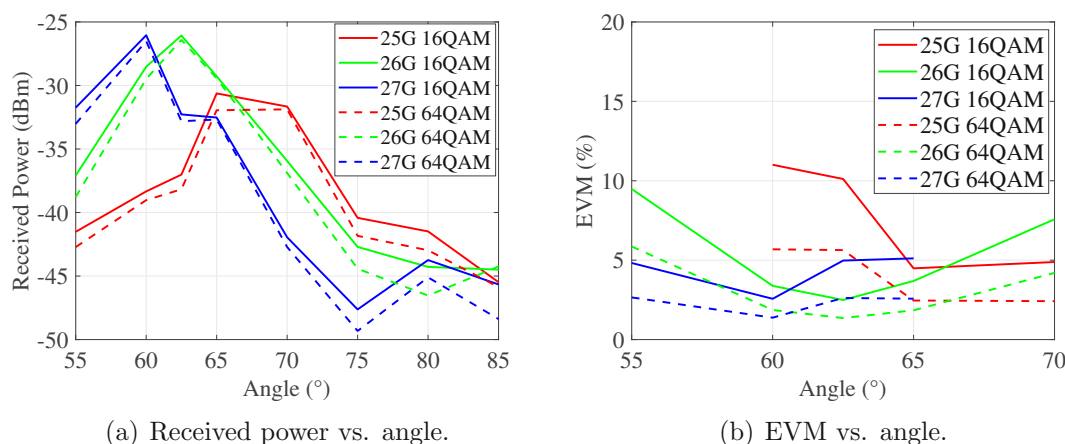


Figure 5.10: Measured results of the 96×96 -sized AR with 16 QAM and 64 QAM modulated waves.

5.3. Communication measurement of the manufactured AR

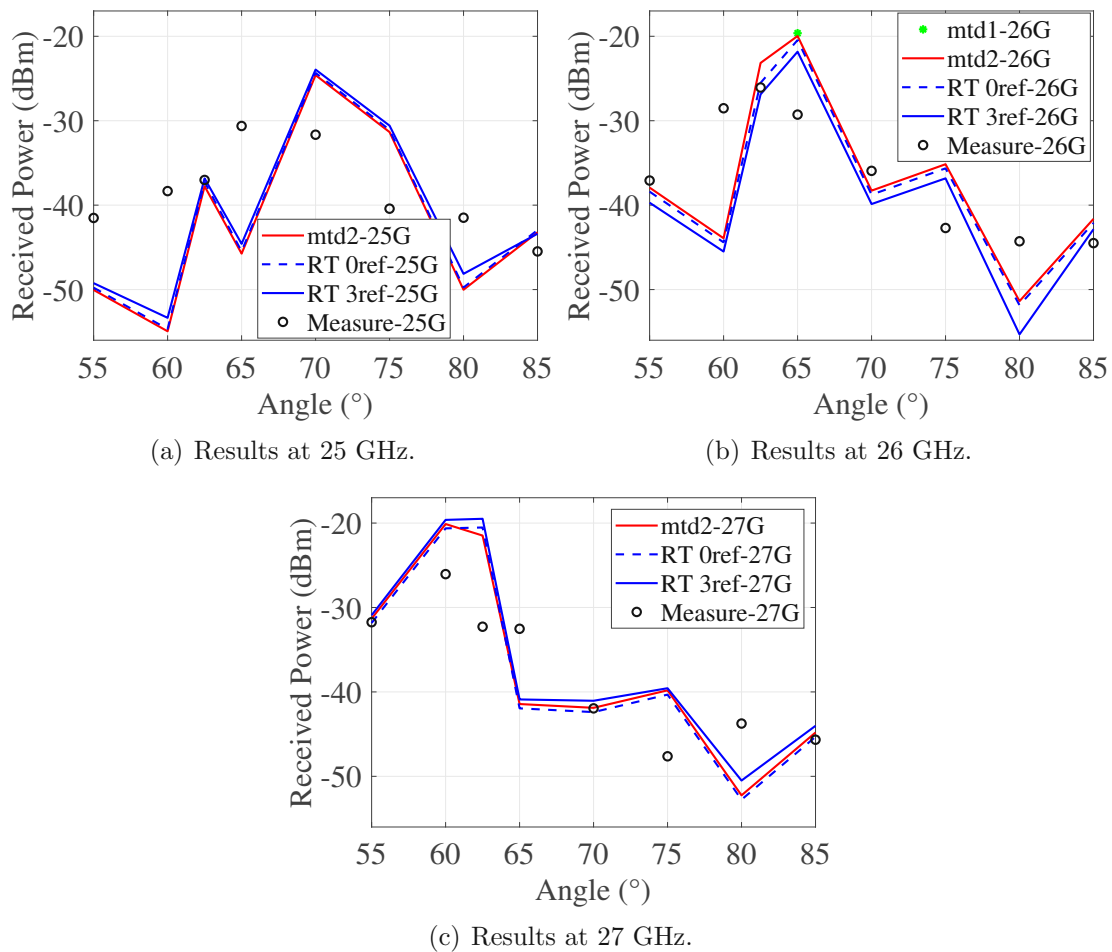


Figure 5.11: Results with the 96×96 -sized AR from corrected calculation and simulation, and from measurements using the modulated waves.

interesting finding is that at some angles, the simulation and measurement results match very well, such as the power in 62.5° at 25 GHz and 26 GHz. Since the beam width of the large AR is much narrower than the small AR, the simulation and measurement results have larger differences in different angles generally. These big differences may be due to the following reasons:

- The accuracy of measurement is reduced due to the more sensitive angular response of the large AR, and the angle samples for measurement are too sparse for this AR;
- The simulated AR gain used in method 2 and the radiation pattern used in ray tracing simulations are from a 96×96 complete panel without discontinuity, while the measured AR is a manually combined one, any misalignment of the elements from the four small ARs will reduce the total scattering property of the big AR. The copper glue at the back of the ARs may also influence the reflection property and the frequency selectivity of the AR;

5.3. Communication measurement of the manufactured AR

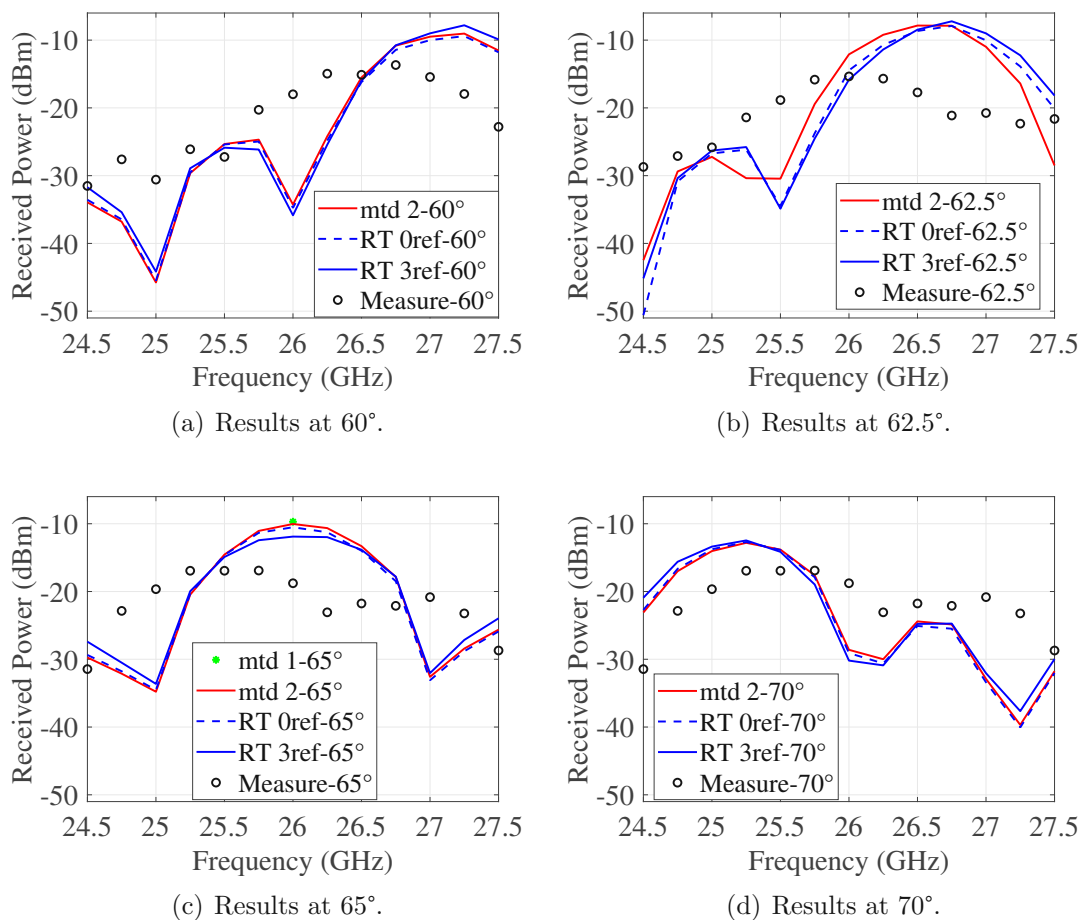


Figure 5.12: Results with the 96×96 -sized AR from corrected calculation and simulation, and from measurements using the continuous waves.

- Method 2 and the ray tracing simulations give far-field results for the big AR while the measured AR is in the near-field, thus the comparison between them does not match very well.

Similar to the 48×48 -sized AR, we compare the results corrected by continuous wave measurement. The results at the 13 frequencies are shown in Fig. 5.12, which show very big differences between the simulation and measurements again. These results reveal that the big AR still works at 26 GHz, but the main beam has a slight shift; the working bandwidth for this AR is approximately 1 GHz. It would be interesting to also compare the performance of this combined AR with a manufactured 96×96 -sized complete AR, and measure the scattering pattern of the big AR when the condition allows. This will help us find out whether the differences come from the manual scale of the four ARs or from the radiation pattern differences between simulation and measurement. This work is postponed to the future as a next step.

5.4 Final remarks

In this chapter, we introduce a manufactured AR that can reflect normal incident plane waves toward 65° at 26 GHz. The scattering pattern of this AR from CST simulation and measurement is consistent in the main reflection directions. We then conduct over-the-air measurements in an auditorium with the 48×48 -sized AR, to measure the received power at a Rx antenna through the Tx-AR-Rx link. In addition, we calculate the received power of the AR-assisted link theoretically with two different models. These results are compared with ray tracing simulations, where we implement the AR into the MATLAB ray tracer and simulate the exact scenario as measurement. The calculated and simulated results show good agreement with the measurement results over different frequencies and different angles.

In addition, we glue four pieces of the 48×48 -sized AR to form a 96×96 -sized AR and measure the received power at the Rx through this combined AR. When we manually combine four small AR pieces together, there could be some uncertainty in distances at the edge elements. Therefore, we expect reduced performance compared to a whole piece of manufactured 96×96 -sized AR since the manufactured AR would ensure perfect distances between all elements. This uncertainty may lead to a shift of the main reflection beam direction of the AR, as our measurement results show that the peak received power at observed angles shifts to 62.5° at 26 GHz with the combined AR. The frequency response of this AR is not as good as the small AR, but the simulation and measurement results have some good agreements at several angles and frequencies. It is proved that our method of implementing an AR in the MATLAB ray tracer is correct, which can be extended to any kind of AR and also other ray tracing tools, as long as the radiation pattern of the AR is available. Our designed AR has a wideband property and can work well within a 2.75 GHz bandwidth. The designed AR also has good spatial scalability, when combining multiple smaller pieces of ARs to form a bigger AR, the big AR can achieve good performance with little deviation, which can be used as a convenient alternative to completely redesigning a new AR with a bigger size.

6

Conclusion and outlook

Serving as a cost-effective and sustainable solution for the next generation of wireless communication, RIS technology becomes attractive due to its advantages of improving coverage, signal strength and energy efficiency with a nearly passive structure. In this dissertation, we have investigated various aspects of RIS technology classified as three big parts. We thus summarize the contributions of the dissertation as follows corresponding to the three parts.

6.1 Summary of contributions

In the first part of the dissertation, we focus on the RIS modeling and applications in the communication part. The contributions in this part are summarized below:

- We extend the open-access Vienna SLS with an RIS module and an interface with the MATLAB ray tracer. We explained the RIS implementation methodology in the SLS that includes several main challenges in the RIS-assisted wireless communication networks, especially the path loss model and channel model for RIS-assisted links. In addition to a free space path loss model, we modify the ray tracing model for RIS-assisted links so that the modified ray tracing model can calculate path loss for RISs correctly and also includes the influences of the propagation environment. The RIS implementation in the SLS and the ray tracer has been verified with known theory so that the SLS with the ray tracer can give reliable and accurate predictions for RIS-assisted links in complex realistic scenarios.
- We develop several approaches to optimize the beamformers at the BS and the phase shifts at RIS for a RIS-assisted MU-MIMO system and, therefore, to improve the system performance, such as signal power, SINR, and rate. An MRT-based heuristic with or without alternating optimization algorithm is proposed to maximize the minimum signal power received by the users and thus achieve good signal quality for all users. To cancel the inter-user interference, we propose a ZF-based optimization approach to maximize the minimum

signal power and increase the minimum SINRs at users. In addition to these power-based optimization approaches, we propose a max-min SINR-based optimization to maximize the minimum SINR for all users. Simulation results show that the MRT-based optimizations can achieve the highest minimum signal power whereas the max-min SINR approach can achieve the highest minimum SINR and minimum rate. In addition, we find that when the RIS phase quantization resolution gets higher, the minimum signal power will be closer to the continuous solution.

The second part of the dissertation discusses the electromagnetic model of an RIS and its applications. This part includes the following contributions:

- We find a low-cost and more convenient alternative than existing passive structure solutions that can enhance radio signal propagation in intricate environments by randomly deploying static scatterers such as purely passive resonant dipoles in the environment. The advantage of this approach is that it does not need human control on the scattering directions and can reach users in any direction since the radiation pattern of dipoles is omnidirectional in the azimuth plane. We develop a modified ray tracing-based model according to the bistatic scattering cross-section of dipolar scatterers to analyze the received power at the Rx antenna through those dipoles. Then we run ray tracing simulations in indoor and outdoor scenarios with the direct link between the Tx and the Rx antennas totally blocked or not blocked. We investigate the influences of different reflection materials, different numbers of reflection paths, different frequencies, and different numbers of dipolar scatterers. The simulation results reveal that the contributions due to the scatterers are not significant when the direct link is not blocked. However, in a scenario in which the direct link is totally blocked, these scatterers can improve the received power at the Rx antenna significantly. By increasing the number of dipolar scatterers, it can achieve similar benefits as using an unturned RIS. The improvement due to the increase of the dipole numbers is higher in a rich scattering environment than in a sparse scattering environment. These scatterers also contribute more when the material loss is higher (such as “Ceiling board”) and at lower frequencies.
- We discuss two path loss models for an optimized RIS that are derived from communication theory and electromagnetic theory, namely the RIS CM model and the RIS EM model. The RIS CM model uses the simplified RIS model that assumes the electric field from the RIS panel is a collection of multiple independent RIS elements, and the wave interactions between each element are ignored, which is not correct in the electromagnetic theory. On the contrary, the RIS EM model captures the total electric field from the whole RIS panel, which involves the geometrical area, incident, and reflection angles of the RIS. The RIS EM model gives the same results as the RIS CM model only when the total effective area of the RIS is assumed to be the same for the two models, and only for perfectly functioning RISs. Since the RIS EM

6.1. Summary of contributions

model is more accurate and reasonable, it has been implemented in the Vienna SLS for the RIS module. However, the RIS CM model can still be used in large-scale system-level simulations to get an upper-bound estimation of the system performance. For example, in a scenario where hundreds of RISs are deployed, the RIS CM model can quickly give an estimation of the system performance without manually placing and orienting each RIS. However, for obtaining accurate and correct results, the RIS EM model should be used.

The third part of the dissertation focuses on RIS modeling and implementation verification through a perfectly designed RIS and a manufactured realistic AR. The contributions in this part are summarized as follows:

- We design a periodical AR according to the Floquet theory that can reflect normal incident waves in different anomalous directions. We optimize the load impedance of each unit cell to achieve maximized power reflection efficiencies for each of the four propagation modes, which correspond to the reflection angles of 13° , 27° , 43° , and 65° . We analyze the reflection efficiency and RIS phase quantization losses with one to four-bit quantization resolutions, respectively, and conclude that a three-bit resolution can already achieve very good results. Next, we pass the EM properties of the designed RIS to two different path loss models to evaluate the large-scale fading through this RIS. One model is the theoretical model for perfectly functioning RIS implemented in the Vienna SLS, and the other one is related to the EM simulation results of the RIS in the CST software. Finally, we implement this designed RIS as antennas into the MATLAB ray tracer to compare the received power through the RIS in different scenarios and verify the simulation results with theoretical results.
- Continuing with the perfectly designed RIS, we tweak the design a bit and manufacture a static passive AR prototype that can reflect normal incident waves in 65° at 26 GHz. Afterward, we measure the scattering pattern of the 48×48 -sized AR prototype in an anechoic chamber. The measurement results are very close to the CST simulated results in the main reflection direction of the AR. In addition to the 48×48 -sized AR, we obtain a 96×96 -sized AR by manually gluing four pieces of the small ARs together. Next, we perform over-the-air measurements in an auditorium with the two different-sized ARs and use the same two path loss models as in Chapter 4 to analyze the large-scale fading through the two ARs. Furthermore, we use the same strategy as Chapter 4 to implement the two ARs into MATLAB ray tracer to simulate the same scenario as in measurements. We evaluate the angular response and frequency response of the two ARs through theoretical models, ray tracing simulations, and measurements, and finally we achieve good agreement between them.
- Together with the designed perfect RIS in Chapter 4 and the lossy realistic AR in Chapter 5, we demonstrate that our RIS analysis methods from the EM design, RIS implementation method in the ray tracer, and the system-level and ray tracing simulations with both a perfect and realistic AR, are all

correct and have been verified with measurement results. The RIS models are consistent with electromagnetic theory and communication theory, the SLS and ray tracer work not only for a perfect RIS but also for a realistic static AR. The RIS implementation methods can also be applied to other ray tracing tools. The analysis methods can be extended to other types of RISs or ARs. The validated connections between the EM and communication analysis for an RIS can accelerate the RIS technology realization. For example, by passing a limited set of macroscopic RIS parameters from the EM design to the RIS-tailored Vienna SLS, the simulator can deal with realistic RISs in large-scale scenarios. In addition, by importing the radiation pattern of an RIS into ray tracers, one can simulate the RISs in different scenarios, taking the propagation environment's effects into consideration. By using our approaches with the software, we can obtain a good estimation of the system performance with realistic RISs in realistic scenarios without the need to conduct measurements.

6.2 Possible future work directions

Despite the broad range of research work that has been done for RIS, there are still some open challenges, and possible improvements can be made in the future. In the following, we list some potential works for the future:

- **RIS-related models:** Throughout this work, all the models we use for RIS are based on far-field assumptions. However, this condition cannot always be met in reality. It is also important to investigate RIS models and path loss models that work in the radiation near field, from both the communication and electromagnetic aspects.
- **The RIS-tailored Vienna SLS:** Since the current version of the Vienna SLS only provides RIS phase shift optimization for SISO scenarios. In the future, when the complexity and simulation time issue can be solved, possible RIS phase shift optimization algorithms for RIS-assisted MU-MIMO systems could also be implemented in the simulator.
- **Static scatterers approaches:** In Chapter 3, we analyzed the potential benefit of deploying static scatterers such as resonate dipoles through theoretical analysis and simulations. In the future, it would be beneficial to perform measurements to investigate how much gain we can obtain through the proposed approaches in real environments.
- **RIS design method:** Our designed RIS is intended for reflection in discrete anomalous directions. In the future, the unit cell loads of the array could be made reconfigurable so that a non-perfect anomalous reflection in the gap angles would be allowed by the design and thus improve the coverage between the discrete modal anomalous angles. Another possibility is to construct a

multimode static anomalous reflector from multiple single-reflection angle sub-panels, i.e., not having an RIS as a reconfigurable surface, but multiple static anomalous reflectors side-by-side to implement the same functionality as the multimode RIS would do.

- **RIS measurements:** In our work, we performed indoor measurements with the manufactured static AR prototypes. However, measurements in outdoor scenarios with RISs would be very necessary since a sparse or rich scattering environment will influence the results very much. In the future, when the condition allows, we could also measure the scattering pattern of a very big AR and conduct communication link measurements in its far-field region. It would also be interesting to compare the performance between a manually combined big AR and a manufactured complete AR panel of the same size.
- **RIS shape effects:** In our work, we only analyzed RISs with squared shapes. However, it would be interesting to also investigate the RIS performance with rectangular or round shapes.

List of Abbreviations

1G	1st generation
2G	2nd generation
3G	3rd generation
4G	4th generation
5G	5th generation
6G	sixth-generation
AR	anomalous reflector
B5G	beyond fifth-generation
BS	base station
CDF	cumulative distribution function
CPW	coplanar waveguide
DAC	digital-to-analog converter
ECDF	empirical cumulative distribution function
EM	electromagnetic
EVM	error vector magnitude
HPBW	half power beam width
IRS	intelligent reflecting surface
LNA	low-noise-amplifier
LOS	line-of-sight
MF	macroscopic fading
MIMO	multiple-input multiple-output
MRT	maximum ratio transmission
MU-MIMO	multi-user MIMO
NLOS	non-line-of-sight
OFDM	orthogonal frequency-division multiplexing
PCB	printed circuit board
PEC	perfect electric conductor
QAM	quadrature amplitude modulation
RIS	reconfigurable intelligent surface
RT	ray tracing

List of Abbreviations

Rx	receiving
SINR	signal-to-interference-plus-noise ratio
SISO	single-input single-output
SLS	system-level simulator
Tx	transmitting
UE	user equipment
VSG	vector signal generator
VSA	vector signal analyzer
ZF	zero-forcing

Notation

In the following table, we describe the notation used throughout this work.

x, X	Non-boldface letters denote scalars
\mathbf{x}	Lowercase boldface letters denote vectors
\mathbf{X}	Uppercase boldface letters denote matrices
\mathbf{I}	Identity matrix
$ \cdot $	Absolute values
$\ \mathbf{x}\ $	Euclidean norm of a vector
$(\cdot)^T$	Transpose operation
$(\cdot)^{-1}$	Inverse operation
$(\cdot)^\dagger$	Pseudo-inverse operation
$(\cdot)^*$	Conjugate operation
$(\cdot)^H$	Conjugate transpose operation
$\text{tr}(\cdot)$	Trace of a matrix
$\det(\cdot)$	Determinant of a matrix
$\text{rank}(\cdot)$	Rank of a matrix
$\arg(\cdot)$	Phase
$\text{diag}(\mathbf{x})$	Diagonal matrix with the elements of \mathbf{x} on its diagonal
\odot	Element-wise (Hadamard) product
\sim	Distributed as
$\mathbf{S} \succeq 0$	\mathbf{S} is a positive semi-definite matrix
$\mathbb{E}\{\cdot\}$	Expected value of a random variable
$\mathbb{C}^{a \times b}$	Space of $a \times b$ complex-valued matrices
$\mathcal{CN}(\mu, \sigma^2)$	Complex Gaussian distribution with mean μ and variance σ^2
$\Re(\cdot)$	Real part of a complex variable
$\Im(\cdot)$	Imaginary part of a complex variable

References

- [1] M. A. U. Gawas, “An Overview on Evolution of Mobile Wireless Communication Networks: 1G-6G,” *International Journal on Recent and Innovation Trends in Computing and Communication*, vol. 3, no. 5, p. 3130–3133, May 2015.
- [2] M. Servetnyk and R. Servetnyk, “Emerging applications, technologies, and services in wireless communications: 5G to 6G evolution,” *Social Development and Security*, vol. 11, no. 2, pp. 3–10, Apr. 2021.
- [3] A. A. A. Solyman and K. Yahya, “Evolution of wireless communication networks: from 1G to 6G and future perspective,” *International Journal of Electrical and Computer Engineering (IJECE)*, vol. 12, no. 4, p. 3943–3950, August 2022.
- [4] Ericsson, “6G – Connecting a cyber-physical world,” Feb. 2022. [Online]. Available: <https://www.ericsson.com/4927de/assets/local/reports-papers/white-papers/6g--connecting-a-cyber-physical-world.pdf>
- [5] S. Abeywickrama, R. Zhang, and C. Yuen, “Intelligent reflecting surface: Practical phase shift model and beamforming optimization,” in *2020 IEEE International Conference on Communications (ICC)*, 2020, pp. 1–6.
- [6] M. A. ElMossallamy, H. Zhang, L. Song, K. G. Seddik, Z. Han, and G. Y. Li, “Reconfigurable intelligent surfaces for wireless communications: Principles, challenges, and opportunities,” *IEEE Transactions on Cognitive Communications and Networking*, vol. 6, no. 3, pp. 990–1002, Sep. 2020.
- [7] Ö. Özgecan, E. Björnson, and E. G. Larsson, “Intelligent reflecting surfaces: Physics, propagation, and pathloss modeling,” *IEEE Wireless Communications Letters*, vol. 9, no. 5, pp. 581–585, May 2020.
- [8] M. Di Renzo, A. Zappone, M. Debbah, M.-S. Alouini, C. Yuen, J. de Rosny, and S. Tretyakov, “Smart radio environments empowered by reconfigurable intelligent surfaces: How it works, state of research, and the road ahead,” *IEEE Journal on Selected Areas in Communications*, vol. 38, no. 11, pp. 2450–2525, Nov. 2020.

References

- [9] E. Björnson, Ö. Özgecan, and E. G. Larsson, “Intelligent reflecting surface versus decode-and-forward: How large surfaces are needed to beat relaying?” *IEEE Wireless Communications Letters*, vol. 9, no. 2, p. 244–248, Feb. 2020. [Online]. Available: <http://dx.doi.org/10.1109/LWC.2019.2950624>
- [10] T. Zhou, K. Xu, X. Xia, W. Xie, and J. Xu, “Achievable Rate Optimization for Aerial Intelligent Reflecting Surface-Aided Cell-Free Massive MIMO System,” *IEEE Access*, vol. 9, pp. 3828–3837, 2021.
- [11] Q. Wu, S. Zhang, B. Zheng, C. You, and R. Zhang, “Intelligent reflecting surface-aided wireless communications: A tutorial,” *IEEE Transactions on Communications*, vol. 69, pp. 3313–3351, 2021.
- [12] J. Chen, Y.-C. Liang, H. V. Cheng, and W. Yu, “Channel Estimation for Reconfigurable Intelligent Surface Aided Multi-User mmWave MIMO Systems,” *IEEE Transactions on Wireless Communications*, vol. 22, no. 10, pp. 6853–6869, 2023.
- [13] Q. Wu and R. Zhang, “Towards smart and reconfigurable environment: Intelligent reflecting surface aided wireless network,” *IEEE Communications Magazine*, vol. 58, no. 1, pp. 106–112, Jan. 2020.
- [14] C. Huang, G. C. Alexandropoulos, A. Zappone, M. Debbah, and C. Yuen, “Energy efficient multi-user MISO communication using low resolution large intelligent surfaces,” in *2018 IEEE Globecom Workshops (GC Wkshps)*, 2018, pp. 1–6.
- [15] M. Najafi, V. Jamali, R. Schober, and H. V. Poor, “Physics-based modeling and scalable optimization of large intelligent reflecting surfaces,” *IEEE Transactions on Communications*, vol. 69, no. 4, pp. 2673–2691, 2021.
- [16] M. Di Renzo, F. Habibi Danufane, X. Xi, J. de Rosny, and S. Tretyakov, “Analytical modeling of the path-loss for reconfigurable intelligent surfaces – anomalous mirror or scatterer ?” in *2020 IEEE 21st International Workshop on Signal Processing Advances in Wireless Communications (SPAWC)*, 2020, pp. 1–5.
- [17] L. Hao, A. Fastenbauer, S. Schwarz, and M. Rupp, “Towards system level simulation of reconfigurable intelligent surfaces,” in *2022 International Symposium ELMAR*, Sep. 2022, pp. 81–84.
- [18] L. Hao, S. Schwarz, and M. Rupp, “The extended Vienna system-level simulator for reconfigurable intelligent surfaces,” in *2023 Joint European Conference on Networks and Communications & 6G Summit (EuCNC/6G Summit)*, Jul. 2023, pp. 1–6.

References

- [19] L. Hao, S. Schwarz, and M. Rupp, “Analysis and Optimization of Reconfigurable Intelligent Surfaces Assisted MIMO Systems,” in *2021 Joint European Conference on Networks and Communications & 6G Summit (EuCNC/6G Summit)*, 2021, pp. 13–18.
- [20] L. Hao, F. S. Cuesta, S. A. Tretyakov, and M. Rupp, “Improving propagation channels with static scatterers,” *IEEE Antennas and Wireless Propagation Letters*, vol. 23, no. 6, pp. 1924 – 1928, 2024.
- [21] L. Hao, F. S. Cuesta, S. A. Tretyakov, and M. Rupp, “Optimizing propagation channels using static scatterers: Modeling and ray-tracing simulations,” in *2024 IEEE International Symposium on Antennas and Propagation and ITNC-USNC-URSI Radio Science Meeting*, 2024.
- [22] L. Hao, F. S. Cuesta, and S. A. Tretyakov, “Comparison of simplistic system-level ris models and diffraction-theory solutions,” in *2024 18th European Conference on Antennas and Propagation (EuCAP)*, 2024, pp. 1–5.
- [23] S. K. R. Vuyyuru, L. Hao, M. Rupp, S. A. Tretyakov, and R. Valkonen, “Modeling RIS from Electromagnetic Principles to Communication Systems—Part I: Synthesis and Characterization of a Scalable Anomalous Reflector,” *submitted to IEEE Transactions on Antennas and Propagation*, 2024. [Online]. Available: <https://doi.org/10.48550/arXiv.2403.12790>
- [24] L. Hao, S. K. R. Vuyyuru, S. A. Tretyakov, A. Salihu, M. Rupp, and R. Valkonen, “Modeling RIS from Electromagnetic Principles to Communication Systems—Part II: System-Level Simulation, Ray Tracing, and Measurement,” *submitted to IEEE Transactions on Antennas and Propagation*, 2024. [Online]. Available: <https://doi.org/10.48550/arXiv.2403.13210>
- [25] L. Hao, S. K. R. Vuyyuru, S. A. Tretyakov, M. Rupp, and R. Valkonen, “Analysis of Scalable Anomalous Reflectors through Ray Tracing and Measurements,” *submitted to IEEE Transactions on Antennas and Propagation*, 2024.
- [26] M. Di Renzo, F. H. Danufane, and S. Tretyakov, “Communication models for reconfigurable intelligent surfaces: From surface electromagnetics to wireless networks optimization,” *Proceedings of the IEEE*, vol. 110, no. 9, pp. 1164–1209, 2022.
- [27] M. A. Kishk and M.-S. Alouini, “Exploiting randomly located blockages for large-scale deployment of intelligent surfaces,” *IEEE Journal on Selected Areas in Communications*, vol. 39, no. 4, pp. 1043–1056, 2021.
- [28] B. Sihlbom, M. I. Poulakis, and M. D. Renzo, “Reconfigurable intelligent surfaces: Performance assessment through a system-level simulator,” *IEEE Wireless Communications*, pp. 1–10, 2022.

References

- [29] M. K. Müller, F. Ademaj, T. Dittrich, A. Fastenbauer, B. R. Elbal, A. Nabavi, L. Nagel, S. Schwarz, and M. Rupp, “Flexible multi-node simulation of cellular mobile communications: the Vienna 5G System Level Simulator,” *EURASIP Journal on Wireless Communications and Networking*, vol. 2018, no. 1, p. 17, Sep. 2018.
- [30] Q. Wu and R. Zhang, “Intelligent reflecting surface enhanced wireless network via joint active and passive beamforming,” *IEEE Transactions on Wireless Communications*, vol. 18, no. 11, pp. 5394–5409, 2019.
- [31] C. Huang, A. Zappone, G. C. Alexandropoulos, M. Debbah, and C. Yuen, “Reconfigurable intelligent surfaces for energy efficiency in wireless communication,” *IEEE Transactions on Wireless Communications*, vol. 18, no. 8, pp. 4157–4170, 2019.
- [32] N. S. Perović, L.-N. Tran, M. Di Renzo, and M. F. Flanagan, “Achievable Rate Optimization for MIMO Systems With Reconfigurable Intelligent Surfaces,” *IEEE Transactions on Wireless Communications*, vol. 20, no. 6, pp. 3865–3882, 2021.
- [33] X. Qian, M. D. Renzo, J. Liu, A. Kammoun, and M.-S. Alouini, “Beamforming through reconfigurable intelligent surfaces in single-user MIMO systems: SNR distribution and scaling laws in the presence of channel fading and phase noise,” *IEEE Wireless Communications Letters*, vol. 10, pp. 77–81, 2021.
- [34] X. Yu, D. Xu, and R. Schober, “MISO wireless communication systems via intelligent reflecting surfaces : (invited paper),” 2019.
- [35] Q. Nadeem, A. Kammoun, A. Chaaban, M. Debbah, and M. Alouini, “Asymptotic max-min SINR analysis of reconfigurable intelligent surface assisted MISO systems,” *IEEE Transactions on Wireless Communications*, 2020.
- [36] B. Tahir, S. Schwarz, and M. Rupp, “Analysis of Uplink IRS-Assisted NOMA Under Nakagami-m Fading via Moments Matching,” *IEEE Wireless Communications Letters*, vol. 10, no. 3, pp. 624–628, 2021.
- [37] G. Piro, L. A. Grieco, G. Boggia, F. Capozzi, and P. Camarda, “Simulating lte cellular systems: An open-source framework,” *IEEE Transactions on Vehicular Technology*, vol. 60, no. 2, pp. 498–513, 2011.
- [38] “[https://simulte.omnetpp.org/.](https://simulte.omnetpp.org/)”
- [39] C. A. Balanis, *Antenna Theory: Analysis and Design*. John wiley & sons, 2015.
- [40] W. Tang, M. Z. Chen, X. Chen, J. Y. Dai, Y. Han, M. Di Renzo, Y. Zeng, S. Jin, Q. Cheng, and T. J. Cui, “Wireless communications with reconfigurable

- intelligent surface: Path loss modeling and experimental measurement,” *IEEE Transactions on Wireless Communications*, vol. 20, no. 1, pp. 421–439, Jan. 2021.
- [41] S. R. Saunders and A. Aragón-Zavala, *Antennas and propagation for wireless communication systems*, 2nd ed. Chichester, England: J. Wiley & Sons, 2007.
- [42] M. Grant and S. Boyd, “CVX: Matlab software for disciplined convex programming, version 2.1,” <http://cvxr.com/cvx>, Mar. 2014.
- [43] M. S. John G. Proakis, *Digital Communications*, 5th, Ed. McGraw-Hill, Inc., 2007.
- [44] R. Zhang and Y. Liang, “Exploiting multi-antennas for opportunistic spectrum sharing in cognitive radio networks,” *IEEE Journal of Selected Topics in Signal Processing*, vol. 2, no. 1, pp. 88–102, 2008.
- [45] W. Tang, J. Y. Dai, M. Z. Chen, K. Wong, X. Li, X. Zhao, S. Jin, Q. Cheng, and T. J. Cui, “Design and implementation of MIMO transmission through reconfigurable intelligent surface,” in *21st IEEE International Workshop on Signal Processing Advances in Wireless Communications, SPAWC 2020, Atlanta, GA, USA, May 26-29, 2020*. IEEE, 2020, pp. 1–5.
- [46] Z. Yu, C. Feng, Y. Zeng, T. Li, and S. Jin, “Wireless communication using metal reflectors: Reflection modelling and experimental verification,” in *ICC 2023 - IEEE International Conference on Communications*, 2023, pp. 4701–4706.
- [47] W. Tang, X. Chen, M. Z. Chen, J. Y. Dai, Y. Han, M. D. Renzo, S. Jin, Q. Cheng, and T. J. Cui, “Path loss modeling and measurements for reconfigurable intelligent surfaces in the millimeter-wave frequency band,” *IEEE Transactions on Communications*, vol. 70, no. 9, pp. 6259–6276, 2022.
- [48] F. H. Danufane, M. D. Renzo, J. de Rosny, and S. Tretyakov, “On the path-loss of reconfigurable intelligent surfaces: An approach based on Green’s theorem applied to vector fields,” *IEEE Transactions on Communications*, vol. 69, no. 8, pp. 5573–5592, Aug. 2021.
- [49] S. Kosulnikov, F. S. Cuesta, X. Wang, and S. A. Tretyakov, “Simple link-budget estimation formulas for channels including anomalous reflectors,” *IEEE Transactions on Antennas and Propagation*, vol. 71, no. 6, pp. 5276–5288, Jun. 2023.
- [50] S. Tretyakov, “Maximizing absorption and scattering by dipole particles,” *Plasmonics*, vol. 9, p. 935–944, 2014.

References

- [51] F. Xia, S. Quan, and G. He, “RCS calculations of resonant dipole antennas with arbitrary loads based on the equivalent circuit method,” in *2008 8th International Symposium on Antennas, Propagation and EM Theory*, 2008, pp. 867–870.
- [52] F. T. Ulaby, *Fundamentals of Applied Electromagnetics*, 5th ed. Upper Saddle River, N.J.: Prentice Hall, 2007.
- [53] A. Díaz-Rubio, V. S. Asadchy, A. Elsakka, and S. A. Tretyakov, “From the generalized reflection law to the realization of perfect anomalous reflectors,” *Sci. Adv.*, vol. 3, no. 8, p. e1602714, Aug. 2017.
- [54] A. M. H. Wong and G. V. Eleftheriades, “Perfect anomalous reflection with a bipartite Huygens’ metasurface,” *Phys. Rev. X*, vol. 8, p. 011036, Feb 2018. [Online]. Available: <https://link.aps.org/doi/10.1103/PhysRevX.8.011036>
- [55] D.-H. Kwon, “Lossless scalar metasurfaces for anomalous reflection based on efficient surface field optimization,” *IEEE Antennas Wireless Propag. Lett.*, vol. 17, no. 7, pp. 1149–1152, Jul. 2018.
- [56] V. S. Asadchy, A. Díaz-Rubio, S. N. Tsvetkova, D.-H. Kwon, A. Elsakka, M. Albooyeh, and S. A. Tretyakov, “Flat engineered multichannel reflectors,” *Phys. Rev. X*, vol. 7, p. 031046, Sep 2017. [Online]. Available: <https://link.aps.org/doi/10.1103/PhysRevX.7.031046>
- [57] V. S. Asadchy, M. Albooyeh, S. N. Tsvetkova, A. Díaz-Rubio, Y. Ra’di, and S. A. Tretyakov, “Perfect control of reflection and refraction using spatially dispersive metasurfaces,” *Phys. Rev. B*, vol. 94, p. 075142, Aug 2016. [Online]. Available: <https://link.aps.org/doi/10.1103/PhysRevB.94.075142>
- [58] Y. Ra’di and A. Alù, “Metagratings for efficient wavefront manipulation,” *IEEE Photon. J.*, vol. 14, no. 1, pp. 1–13, Feb. 2022.
- [59] A. Casolaro, A. Toscano, A. Alu, and F. Bilotti, “Dynamic beam steering with reconfigurable metagratings,” *IEEE Trans. Antennas Propag.*, vol. 68, no. 3, pp. 1542–1552, Mar. 2020.
- [60] O. Rabinovich and A. Epstein, “Dual-polarized all-metallic metagratings for perfect anomalous reflection,” *Phys. Rev. Appl.*, vol. 14, p. 064028, Dec 2020. [Online]. Available: <https://link.aps.org/doi/10.1103/PhysRevApplied.14.064028>
- [61] V. Popov, F. Boust, and S. N. Burokur, “Constructing the near field and far field with reactive metagratings: Study on the degrees of freedom,” *Phys. Rev. Appl.*, vol. 11, p. 024074, Feb 2019. [Online]. Available: <https://link.aps.org/doi/10.1103/PhysRevApplied.11.024074>

References

- [62] N. Yu, P. Genevet, M. A. Kats, F. Aieta, J.-P. Tetienne, F. Capasso, and Z. Gaburro, “Light propagation with phase discontinuities: generalized laws of reflection and refraction,” *Science*, vol. 334, pp. 333–337, Oct. 2011.
- [63] J. Huang and J. A. Encinar, *Reflectarray Antennas*. Hoboken, NJ, USA: Wiley, 2008.
- [64] S. K. R. Vuyyuru, R. Valkonen, D.-H. Kwon, and S. A. Tretyakov, “Efficient anomalous reflector design using array antenna scattering synthesis,” *IEEE Antennas Wireless Propag. Lett.*, vol. 22, no. 7, pp. 1711–1715, 2023.
- [65] V. Degli-Esposti, E. M. Vitucci, M. D. Renzo, and S. A. Tretyakov, “Reradiation and scattering from a reconfigurable intelligent surface: A general macroscopic model,” *IEEE Transactions on Antennas and Propagation*, vol. 70, no. 10, pp. 8691–8706, 2022.
- [66] E. M. Vitucci, M. Fabiani, and V. Degli-Esposti, “Use of a realistic ray-based model for the evaluation of indoor rf coverage solutions using reconfigurable intelligent surfaces,” *Electronics*, vol. 12, no. 5, 2023. [Online]. Available: <https://www.mdpi.com/2079-9292/12/5/1173>
- [67] J. Huang, C.-X. Wang, Y. Sun, R. Feng, J. Huang, B. Guo, Z. Zhong, and T. J. Cui, “Reconfigurable intelligent surfaces: Channel characterization and modeling,” *Proceedings of the IEEE*, vol. 110, no. 9, pp. 1290–1311, 2022.
- [68] P. Gómez García and J.-P. Fernández-Álvarez, “Floquet-bloch theory and its application to the dispersion curves of nonperiodic layered systems,” *Mathematical Problems in Engineering*, p. 12, 2015.
- [69] A. Díaz-Rubio and S. A. Tretyakov, “Macroscopic modeling of anomalously reflecting metasurfaces: Angular response and far-field scattering,” *IEEE Transactions on Antennas and Propagation*, vol. 69, no. 10, pp. 6560–6571, 2021.
- [70] W. L. Stutzman and G. A. Thiele, *Antenna Theory and Design*. John Wiley Sons, 1998.
- [71] S. W. Ellingson, “Path loss in reconfigurable intelligent surface-enabled channels,” in *2021 IEEE 32nd Annual International Symposium on Personal, Indoor and Mobile Radio Communications (PIMRC)*, 2021, pp. 829–835.
- [72] L. Gotszald, “Novel Tracing Algorithm vs Remcom Wireless InSite,” *International Journal of Electronics and Telecommunications*, vol. vol. 61, no. No 3, 2015. [Online]. Available: <http://journals.pan.pl/Content/87871/PDF/36.pdf>
- [73] K. Guan, D. He, and Z. Zhong, “CloudRT: A Chinese example of open science infrastructure and services,” *Cultures of Science*, vol. 4, no. 4, pp. 217–226, 2021. [Online]. Available: <https://doi.org/10.1177/20966083221084142>